# DESIGN AND CHARACTERIZATION OF ROBUST HOT FILM SENSORS FOR TACTICAL AIRCRAFT INLETS

by

STEVEN R. BRADDOM

Bachelor of Science in Mechanical Engineering
United States Military Academy, 1993

Submitted to the Department of Aeronautics and Astronautics
in Partial Fulfillment of the Requirements for the Degree of

MASTER OF SCIENCE

in

AERONAUTICS AND ASTRONAUTICS

at the

MASSACHUSETTS INSTITUTE OF TECHNOLOGY

February 2002



Author:_____
Department of Aeronautics and Astronautics
February 1, 2002

Certified by:_____
Dr. Gerald R. Guenette
Principal Research Engineer
Thesis Supervisor

Accepted by:_____
Wallace E. Vander Velde
Professor Aeronautics and Astronautics
Chair, Committee on Graduate Students

# DESIGN AND CHARACTERIZATION OF ROBUST HOT FILM SENSORS FOR TACTICAL AIRCRAFT INLETS

by

Steven R. Braddom

Submitted to the Department of Aeronautics and Astronautics on February 1, 2002, in partial fulfillment of the requirements for the degree of Master of Science in Aeronautics and Astronautics

## ABSTRACT

Robust hot film sensors capable of withstanding the environmental hazards common to tactical aircraft while meeting the performance requirements for use in an active control system were developed and tested. The usefulness of the robust sensors was demonstrated by employing hot film sensors in the separated flow region of a small-scale Uninhabited Combat Air Vehicle (UCAV) inlet to provide real time information about the separation induced distortion at the aerodynamic interface plane (AIP).

Robust hot film sensors with 0.2 micrometer thick evaporated Nickel sensor elements on 635 micrometer thick quartz substrates with 2 micrometer thick Aluminum Oxide protective coatings, gold leads, and aspect ratios ranging from 12.5 to 20 were developed. These sensors were tested for Temperature Coefficient of Resistivity (TCR) time stability, steady-state sensitivity, dynamic response, and sand abrasion resistance. The robust sensors exhibited a maximum TCR variation of 0.32 percent over a simulated period of 500 hours of aircraft operation and 82 percent of the laminar flow steady-state sensitivity value of comparable unprotected sensors. The protective coating did not affect the sensor amplitude and phase response at frequencies less than 1000 Hertz and 600 Hertz respectively. The robust sensors on average lasted more than 21 minutes (the equivalent of over 500 hours of aircraft operation) in sand abrasion tests at the maximum sand particle velocities and concentration possible in the actual full-scale UCAV inlet without a significant change in resistance.

Experiments were conducted on a one-sixth scale model of a UCAV inlet with a hot film sensor array lining the separated flow region and unsteady total pressure probes located at the AIP. A characteristic frequency consistent with vortex shedding from the separated flow region was present in the inlet for massflows from 2.9 to 3.4 pounds per second. In the characteristic frequency band, the hot film sensors along the stagnation line at the leading edge of the separated flow region were highly correlated to the unsteady total pressure probes at the AIP. The maximum cross-correlation and coherence values between the hot film sensors and the AIP probes were 0.68 and 0.95 respectively.

Thesis Supervisor: Dr. Gerald R. Guenette
Title: Principal Research Engineer
Department of Aeronautics and Astronautics
Gas Turbine Laboratory

## Acknowledgements

First and foremost I would like to thank my wife Jennifer and my daughters Ashley and Katherine for their understanding and their support, without which this research would not have been possible.

I would also like to express my sincere gratitude to Dr. Gerald Guenette and to Dr. James Paduano for their constant mentorship, their technical expertise, and their decision to allow me to participate in the Micro-Adaptive Flow Control project.

Thanks to the staff of the Gas Turbine Laboratory, specifically James Letendre, Jack Costa, and Victor Dubrowski as well as to the staff of the Microsystems Technology Laboratory, specifically Vicky Diadiuk, Kurt Broderick, Dan Adams, and Paul Tierney for their frequent help and advice in the fabrication and assembly of the various experimental test rigs and the robust sensors themselves.

Finally, I would like to thank the other members of the Micro-Adaptive Flow Control project and the members of the Blow-Down Turbine project at MIT, specifically Dr. Michael Brear, Zachary Warfield, Ashish Verma, Brian McElwain, Andrew Luers, Jameel Janjua, and William Fournier for their willingness to frequently put aside their own pressing tasks to lend me their assistance.

# Table of Contents

# List of Figures

# List of Tables

# Nomenclature

## *Roman*

| | |
|---|---|
| $A_{inlet}$ | Cross-sectional area of the full-scale UCAV inlet at the point of separation |
| $A_s$ | Cross-sectional area of the core of the free jet flow (sand abrasion test) |
| B | Sensor sensitivity |
| Bi | Biot number |
| $C_n$ | Equivalent thermal capacitance of node *n* |
| $C_p$ | Specific heat |
| D | Diameter |
| $E_o$ | CTA output voltage with no flow over the sensor |
| $E_{out}$ | CTA output voltage |
| F | Dimensionless frequency |
| $\bar{f}$ | Pipe friction factor |
| g | Gravitational acceleration |
| $Gr_L$ | Grashof number |
| h | Convection heat transfer coefficient at the sensor surface |
| K | Ratio of the substrate thermal conductivity to the fluid thermal conductivity |
| k | Thermal conductivity |
| $K_c$ | Ratio of the coating thermal conductivity to the substrate thermal conductivity |
| l | Length (stream-wise) |
| $L^*$ | Effective sensor element stream-wise length |
| $L'$ | Sonic length (stream-wise distance to the point at which the flow was Mach 1) |
| M | Mach number |
| $\dot{m}$ | Actual small-scale inlet massflow rate (adjusted for ambient conditions) |
| $\dot{m}^*$ | Reference small-scale inlet massflow rate (massflow rate at 295.9 K and 14.7 psi) |
| $\dot{m}_{a_{inlet}}$ | Massflow rate for the full-scale inlet at cruise power |
| $\dot{m}''_{s_{ref}}$ | Reference massflow rate of sand per unit area for the full-scale inlet |
| $\dot{m}''_{s_{test}}$ | Massflow rate of sand per unit area for the sand abrasion test |
| Nu | Sensor Nusselt number |
| $Nu_o$ | Sensor Nusselt number with no flow over the sensor |
| P | Sensor power dissipation |
| p | Ambient atmospheric pressure during small-scale inlet test |
| $p^*$ | Reference atmospheric pressure (14.7 psi) |
| Pe | Peclet number |
| $P_{ff}$ | Power spectral density of discrete signal f |
| $P_{fg}$ | Cross spectral density of discrete signals f and g |
| $p_g$ | Gauge pressure |

| | |
|---|---|
| $\dot{Q}$ | Rate of heat generation |
| $\dot{q}'$ | Rate of heat generation per unit length |
| R | Sensor element resistance at room temperature |
| $R_a$ | Fixed CTA bridge arm resistance (see Figure 5-4) |
| $R_b$ | Fixed CTA bridge arm resistance (see Figure 5-4) |
| $R_c$ | Variable CTA bridge arm resistance (see Figure 5-4) |
| $R_h$ | Sensor heated resistance (resistance at overheat temperature including leads and cables) |
| $R_l$ | Sensor lead and cable resistance |
| $R_{mn}$ | Equivalent thermal resistance between nodes *m* and *n* |
| $R_{20}$ | Sensor element resistance at 20°C |
| $R_{50}$ | Sensor element resistance at 50°C |
| s | Fluid shear |
| $S_{out}$ | Scanivalve output value |
| T | Temperature |
| t | Thickness |
| $T^*$ | Reference Temperature (295.9 K) |
| $t^*$ | Sensor element length to thickness ratio |
| $t_f$ | Sensor failure time (sand abrasion test) |
| $t'_f$ | Sensor failure time adjusted to reference sand concentration (sand abrasion test) |
| u | Local stream-wise velocity |
| $U_o$ | Mean free stream velocity |
| V | Volume |
| $V_s$ | Volume of sand injected into the air jet during the sand abrasion test |
| w | Width (span-wise) |
| x | Stream-wise coordinate |

## *Greek*

| | |
|---|---|
| $\alpha$ | Thermal diffusivity |
| $\alpha^*$ | Ratio of thermal diffusivity to the fluid thermal diffusivity |
| $\gamma$ | Ratio of specific heats |
| $\Delta T$ | Sensor overheat temperature above ambient |
| $\varepsilon$ | Free stream oscillation amplitude |
| $\xi$ | Maximum ambient concentration of sand in air (kg sand / cubic meter air) |
| $\eta$ | Fraction of total sand mass injected inside the core of the free jet (sand abrasion test) |
| $\Theta$ | Sensor element Temperature Coefficient of Resistivity based on room temperature resistance (R) |
| $\kappa$ | Constant gain of CTA feedback amplifier |
| $\mu$ | Viscosity |
| $\nu$ | Kinematic viscosity |
| $\rho$ | Electrical resistivity |
| $\rho_{a_{ref}}$ | Reference ambient air density for full-scale inlet |

| | |
|---|---|
| $\rho_e$ | Sensor element density |
| $\rho_s$ | Sand density |
| $\tau_w$ | Wall shear stress |
| $\chi$ | Mass flow plug position |
| $\Phi_{fg}$ | Coherence between discrete signals f and g |
| $\phi_{fg}$ | Cross-correlation between discrete signals f and g |
| $\Omega$ | Ohms |
| $\omega$ | Free stream oscillation frequency |

### *Subscripts*

| | |
|---|---|
| c | Coating |
| e | Sensor element |
| f | Fluid |
| s | Substrate |

### *Acronyms*

| | |
|---|---|
| AIP | Aerodynamic Interface Plane |
| AR | Aspect Ratio |
| CTA | Constant Temperature Anemometer |
| DAQ | Data Acquisition System |
| FIR | Finite Impulse Response |
| HMDS | Hexamethyldisilazane |
| HVAC | Heating, Ventilation and Air Conditioning |
| ID | Inner Diameter |
| MIT | Massachusetts Institute of Technology |
| OD | Outer Diameter |
| PR | Pressure Recovery |
| RMS | Root Mean Square |
| TCR | Temperature Coefficient of Resistivity based on Resistance at 20°C |
| TCR50 | Temperature Coefficient of Resistivity based on Resistance at 50°C |
| TRL | Technology Research Laboratory |
| UCAV | Uninhabited Combat Air Vehicle |

# 1 Introduction

## *1.1 Motivation*

Uninhabited combat air vehicles (UCAVs) are beginning to take a significant role in the missions of all of the branches of the United States Armed Forces. UCAV length, and therefore overall size and weight are currently predicated on the length of the propulsion system. Low observable requirements for the vehicles mean that the engine inlet must involve large turns and/or changes in geometry in order to prevent radar viewing of the compressor face. Such changes in the geometry cause flow separation that translates into distortion at the compressor face. Current research indicates the possibility of using various methods of active control to reduce the flow distortion at the compressor face, allowing shorter inlets or smaller propulsion system stall margins and therefore reducing overall vehicle size, weight and cost. Figure 1-1 below shows a rendering of a Northrup-Grumman UCAV (top), and a photo of the current U.S. Air Force UCAV produced by Boeing (bottom).

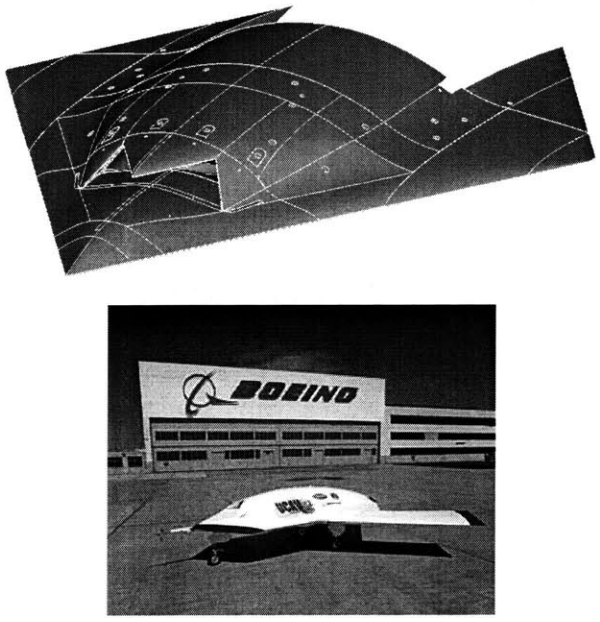


Figure 1-1. Uninhabited Combat Air Vehicles (UCAVs).

Active control systems designed to reduce inlet flow distortion require real time information about the characteristics of the flow separation and the distortion at the aerodynamic interface plane (AIP). The AIP is the interface plane between the inlet and

the compressor. Hot film sensors flush mounted to the inlet surface are ideal sensors for providing this information as they have a high frequency response, are very sensitive to flow changes, and are completely non-intrusive and therefore can be mounted in and around the separated flow region without interfering with the flow. Current research also suggests that hot film sensors near the separation point can provide meaningful real-time information about the characteristics of the flow separation and also about the subsequent distortion at the AIP. However, currently available commercial hot film sensors lack the robustness to operate consistently in a UCAV inlet under the full range of environmental conditions associated with the vehicle's mission profile.

### *1.2 Previous Work*

Previous research by many different individuals has shown both the usefulness of traditional hot film sensors for determining the characteristics of both internal and external flows and the possibility of their use in active control systems to improve aircraft and/or engine performance. Although the possibility of protecting hot film sensors through the use of quartz or other ceramic coatings is alluded to by Popescu [18], there is no available research on the performance of protected sensors or on creating hot film sensors capable of withstanding the extreme environmental conditions common to military and commercial aircraft.

The fact that hot film sensors near the separation point in the UCAV inlet can provide meaningful information about both the characteristics of the separation and the distortion downstream at the AIP was demonstrated by Zachary Warfield in experiments conducted at the Massachusetts Institute of Technology (MIT) on a one-sixth scale model of the inlet for the Northrup-Grumman UCAV shown in Figure 1-1 [22]. These small-scale experiments used planar acoustic waves from actuators downstream of the AIP to attempt to reduce the level of distortion seen at the AIP. The instrumentation for the small-scale MIT experiments included hot film sensors near the separation point and unsteady total pressure probes at the AIP. For a complete description of the configuration for the small-scale experiments, please refer to Warfield's work, *Active Control of Separation Induced Distortion in a Scaled Tactical Aircraft Inlet* [22].

Figure 1-2 shows the coherence and cross-correlation plot for data from a hot film sensor in the separated region versus data taken from a total pressure probe at the AIP in

the MIT small-scale experiments at a model massflow of 3.1 lb/s. Figure 1-2 shows a coherence of greater than 0.5 at frequencies from 500-600 Hz, which Warfield concludes corresponds to the characteristic vortex shedding frequency of the flow separation. A coherence of 0.5 is significant given the amount of noise present in the inlet. Also, the time delay shown in the cross-correlation plot corresponds to the flow convection time from the hot films at the separation point to the AIP, further indicating that the distortion created by the separation and seen by the hot film travels downstream to the AIP. Thus, the small-scale experiments demonstrated that the hot film sensors near the separation point may be able to provide some useful information about both the characteristics of the separation and the characteristics of the distortion at the AIP.

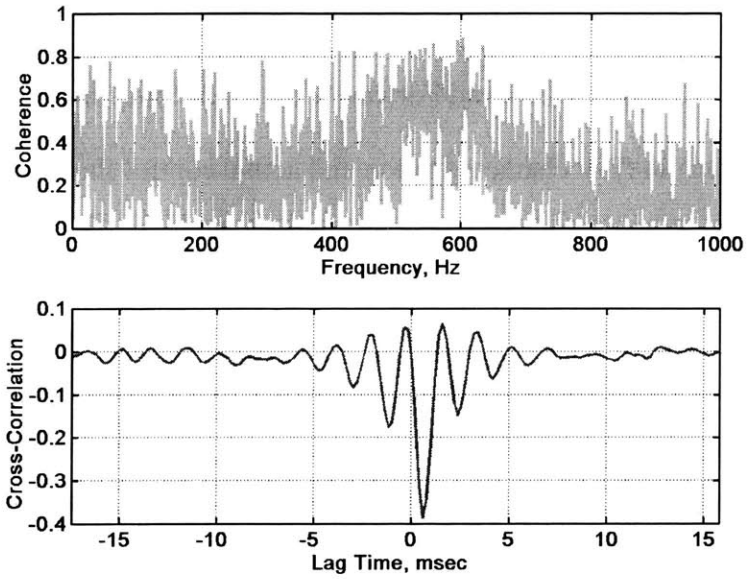


Figure 1-2. Comparison of Hot Film Data to Total Pressure at AIP.

The coherence between the hot film sensors and the downstream actuators in the small-scale experiments was sufficient to generate a transfer function between the two, which was used successfully with single frequency feedback control to reduce local unsteadiness at the hot film sensor location. Furthermore, Warfield raises the possibility of the using the hot film sensors as the inputs for a "feed forward" control system to reduce distortion at the AIP. Figure 1-3 shows Warfield's diagram of the "feed forward" control system setup.

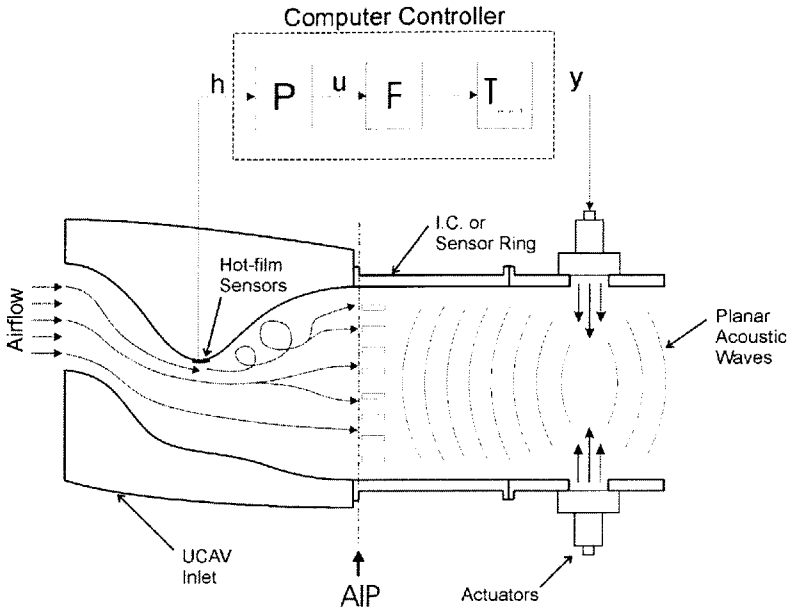


Figure 1-3. Feed Forward Control Architecture.

Other research in flow characterization and active control shows that robust hot film sensors have many other applications aside from their possible role in the active control of the UCAV inlet. Arrays of hot film sensors connected to constant temperature or constant voltage anemometers have been used in flight tests on a variety of aircraft from sailplanes to the F-15B to simultaneously determine external flow characteristics such as the location of stagnation, separation, and reattachment points; turbulence levels; shock locations; and transition characteristics [13]. The work of Moes, Sarma, and Mangalam further indicates the possibility of controlling a variable geometry inlet for a supersonic cruise vehicle using arrays of hot film sensors to detect in real time the location of steady or rapidly moving shocks in the inlet [14]. Hot film sensors in these and other external and internal aerodynamic applications for production aircraft clearly must be robust enough to provide consistent results despite environmental hazards such as extreme temperatures, thermal shock, and abrasion from sand, dust and precipitation.

### *1.3 Hot Film Anemometry*

Hot film anemometry is based on two simple facts. First, "...a fluid flowing over a heated surface transfers heat away from that surface in an amount related to the shear stress exerted by the fluid on that surface" [12]. Second, the electrical resistivity of metal is related to its temperature. Therefore, if a thin metal film is connected to a feedback

circuit (as shown in Figure 1-4) which supplies an electrical current to the film such that the film is maintained at a constant resistance, and thus a constant temperature (above the fluid temperature), then fluctuations in the instantaneous shear stress on the film will appear as fluctuations in the electrical current required to maintain the film at the desired temperature. This type of anemometry is referred to as Constant Temperature Anemometry (CTA). Constant current and constant voltage methods also exist, but only the CTA method was used for this research. Current CTA systems have a maximum frequency response on the order of 100 kHz. Figure 1-4 shows a typical hot film constant temperature anemometer system.

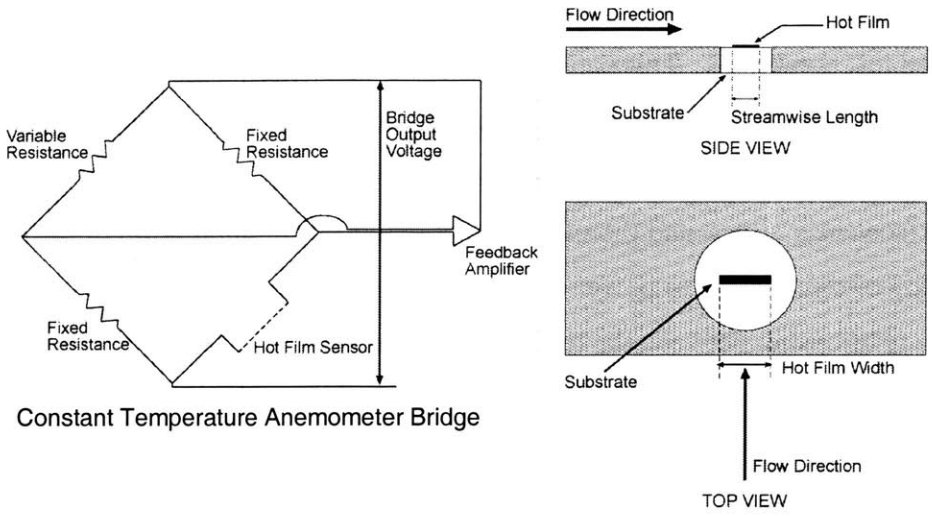


Figure 1-4. Typical Hot Film Sensor Constant Temperature Anemometer (CTA) Setup.

The relationship between shear stress and heat transfer, or more appropriately, the relationship between shear stress and the total power dissipated in the sensor is often referred to as the sensitivity of the sensor, and has been the subject of much research, such as the work of Cole and Beck [3] and the work of Menendez and Ramaprian [16]. Note that the relationship is typically expressed in dimensionless terms using the Peclet number as the dimensionless shear stress and the Nusselt number as the dimensionless power dissipated. The Peclet number is defined as $Pe \equiv \frac{sl_e^2}{\alpha_f}$ where s is the fluid shear at

the wall ( $s \equiv \frac{\partial u}{\partial y}|_{y=0}$ ), $l_e$ is the probe streamwise length, and $\alpha_f$ is the fluid thermal diffusivity. The Nusselt number is defined as: $Nu \equiv \frac{P}{w_e k_f \Delta T}$ where P is the probe power dissipation, $w_e$ is the probe spanwise width, $k_f$ is the fluid thermal conductivity, and $\Delta T$ is the probe overheat temperature. Due to the complexities of the sensor interaction with the substrate and the fluid thermal and velocity boundary layers, the exact relationship between the surface shear stress and the power dissipated in the sensor can only be determined analytically for the simplest of flow conditions, and is most often determined through calibration in known flow conditions which are extremely similar to the desired test conditions. This calibration requirement is the largest drawback to the use of hot film sensors to measure surface shear stress. However, the applications of interest here for the sensors (as discussed above) do not require an absolute measurement of the surface shear stress, and therefore do not require the computation of the exact relationship of shear stress to power dissipated.

The relationship between the temperature of a substance and its electrical resistivity is quantified by the Temperature Coefficient of Resistivity (TCR), which is defined as: $TCR \equiv \frac{1}{\rho}\frac{d\rho}{dT} \approx \frac{1}{R_{20}}\frac{\Delta R}{\Delta T}$ where $\rho$ is the material resistivity and $R_{20}$ is the material resistance at 20°C. For typical metals, the relationship between temperature and resistivity is approximately linear above the Debye Temperature (~300 K) and of the form $\rho \sim T^5$ below the Debye Temperature.

### *1.4 Objectives*

The objective of this research was to demonstrate the feasibility of using hot film sensors as inputs for active control systems in production aircraft. This objective had two parts. The first was to further demonstrate that hot film sensors located in the separated flow region of an inlet can provide valuable data about the separation itself as well as about the conditions at the AIP by conducting additional small-scale experiments on the Northrup-Grumman UCAV inlet with additional instrumentation. The second part was the design and testing of a robust hot film sensor capable of providing consistent, meaningful data about the characteristics of the inlet flow over long periods of time

throughout the range of environmental conditions experienced by actual production aircraft.

### *1.5 Thesis Overview*

The remainder of this thesis focuses on the two objectives outlined above. Chapters 2 and 3 describe the experimental setup for the small-scale inlet tests as well as the experimental results. Chapter 4 gives a description of the development of the performance and environmental requirements for the robust sensors. Chapter 5 covers the design of the robust sensors to include the selection of the materials and the physical dimensions. Chapter 6 describes the fabrication process used to construct the sensors. Chapter 7 describes the experimental facilities and results from the environmental and performance tests performed on the robust sensors. A summary of the experimental results and recommendations for future work are given in Chapter 8.

# 2 Small-Scale Inlet Experimental Facility

## *2.1 Overview*

The small-scale inlet experiments were conducted with three primary objectives: first, to demonstrate that hot film sensors in the separated flow region can predict unsteady flow conditions at the AIP; second, to show that the hot film sensors can determine the steady intensity of the separation and thus provide information on the inlet pressure recovery; and third, to provide insight into the most effective sensor locations for predicting the unsteady AIP conditions.

The experimental facility consisted of a one-sixth scale model of the Northrup-Grumman UCAV shown in Figure 1-1 with an attached bellmouth to simulate cruise airflow conditions. The separated flow region of the top surface of the inlet was instrumented with an array of hot film sensors. Immediately downstream of the inlet was a sensor ring containing three total pressure probes to measure unsteady AIP conditions. Downstream of the sensor ring was an instrument can containing a steady total pressure measurement rake consisting of 40 sensors, which was not used during these experiments. A calibrated, variable mass flow plug connected the instrument can to the inlet of a De-Laval compressor which provided the suction required to pull air through the inlet at massflow rates from 2.0 – 3.7 lb/s. Figure 2-1 shows a diagram and a photograph of the overall experimental setup. The details of the operational procedure and characteristics of the De-Laval compressor and its associated turbomachinery as well as the design of the sensor ring and the total pressure probes are contained in Warfield's Thesis [22].

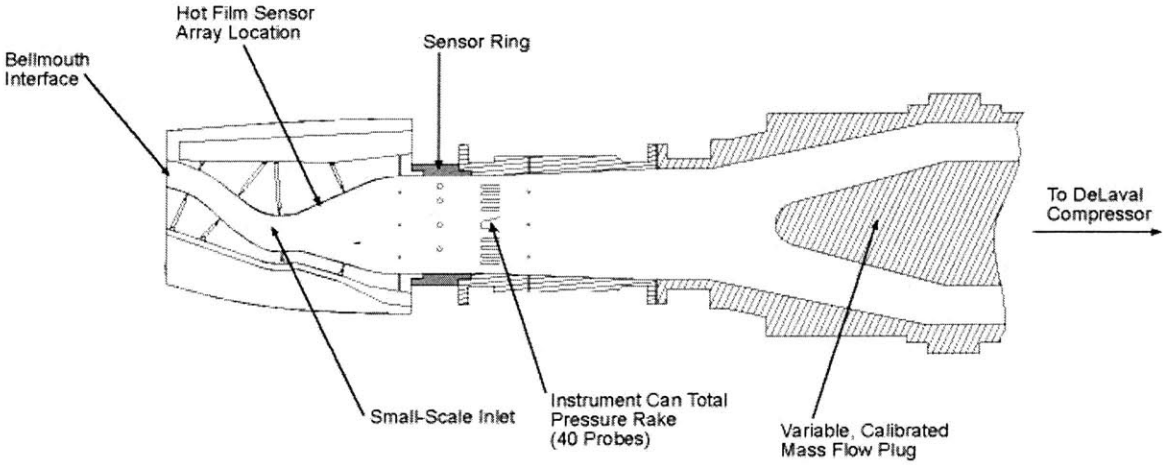

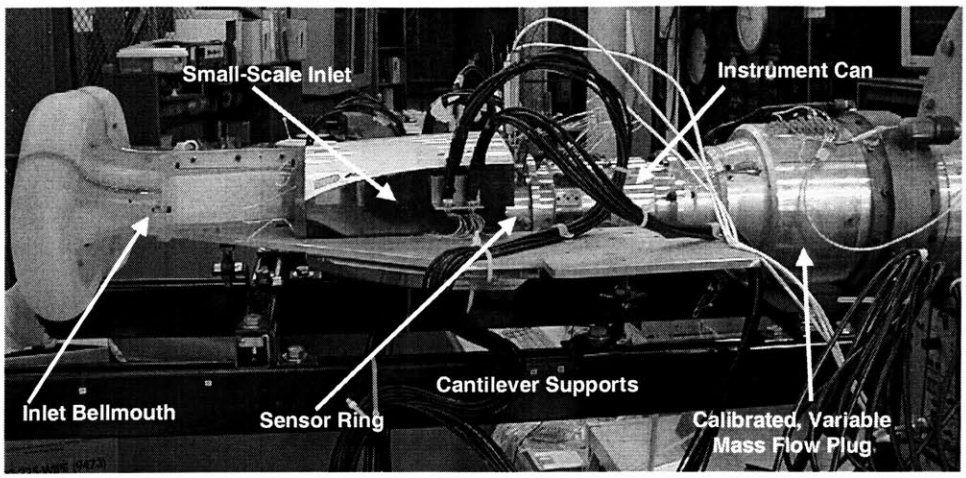


Figure 2-1. Small-Scale Inlet Experimental Setup.

## *2.2 Hot Film Sensor Array*

### *2.2.1 Design & Characteristics*

The hot film sensor array was designed to span the entire separated flow region for the complete range of inlet mass flows. In order to achieve complete coverage of the separated region, the design of the array was conducted using the results of the flow visualization experiments conducted by Warfield on the small-scale inlet. Figure 2-2 shows the final 30 sensor locations superimposed against the flow visualization results. The final sensor array design provided complete coverage of the separated flow area for

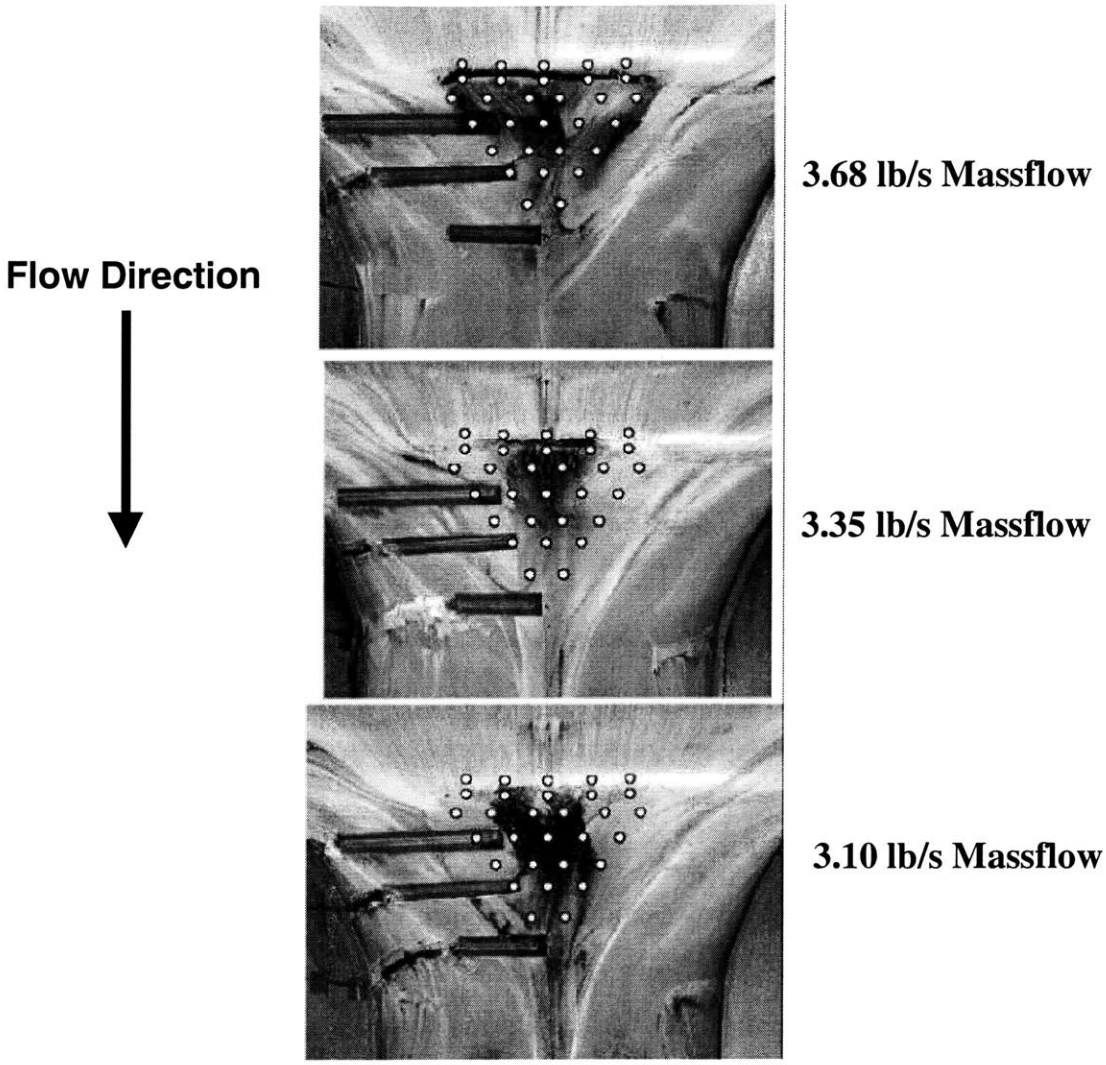


Figure 2-2. Hot Film Sensor Locations.

the entire range of massflows with a higher sensor density at the leading edge of the separation in order to provide greater resolution of the flow activity in the vicinity of the leading edge stagnation line. The number of sensor elements was constrained to a maximum of 30 by the overall cost of the array, the minimum possible lead width (0.010"), and the number of CTAs available to operate the sensors. The sensors were placed in a span-wise symmetric arrangement in order to allow for correlations between symmetric sensor pairs. Such symmetric correlations were used to investigate the possibility of span-wise (left-right) periodicity in the vortex shedding from the separated region.

Figure 2-3 below shows the final design of the sensor array. The array used in the tests was fabricated by Tao of Systems Integrations, Inc. under the brand name SENFLEX® and designated with the array number SF0108. The sensor elements were electron beam deposited Nickel with Copper leads on an Upilex S polyimide film substrate. The characteristics of both the SENFLEX® sensors and the adhesive used to bond the array to the inlet are shown below in Table 2-1. Table 2-2 lists the electrical resistance and coordinates of each sensor on the substrate sheet (as measured in centimeters from the coordinate origin shown in Figure 2-3). The sensor leads were combined into five thin fingers on each side of the array in order to allow them to be smoothly mounted to the compound curved surface of the inlet near the walls.

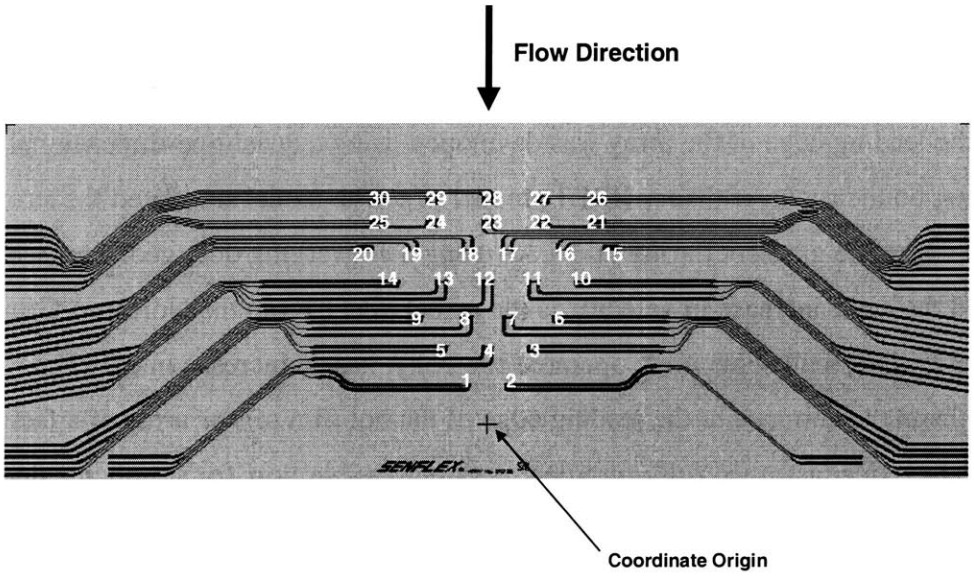


Figure 2-3. Hot Film Sensor Array Design.

| SENFLEX® Hot Film Sensor Characteristics | | | | |
|---|---|---|---|---|
| | Material | Thickness (in) | Length (in) (Stream-wise) | Width (in) (Span-wise) |
| Element | Nickel | $7.9 \times 10^{-6}$ (0.20μm) | 0.004 | 0.057 |
| Leads | Copper | 0.0005 | 0.010 – 0.030 | |
| Substrate | Upilex S Polyimide | 0.002 | | |
| Adhesive | MACtac® IF-2012 | 0.002 | | |

Table 2-1. SENFLEX® Hot Film Sensor Characteristics.

The final consideration in the use of the hot film sensor array was to ensure the array would not significantly alter the original flow of the inlet. For the array not to interfere with the flow, its thickness had to be much less than the thickness of the boundary layer at the point where the flow crosses the leading edge of the array. The maximum thickness of the array including the adhesive layer is 0.0045 inches (114 μm). An order of magnitude estimate of the thickness of the boundary layer of the small-scale inlet at the leading edge of the array was developed using a quasi-one-dimensional interacting boundary layer theory (IBLT) model [8]. The model simulated the strong favorable pressure gradient through the inlet using a converging duct geometry which produced the same increase in velocity as the actual inlet. From the Northrup-Grumman CFD results, the small-scale inlet, operated statically, has an increase in core flow velocity from the entrance to the leading edge of the hot film sensor array of a factor of 50 [4]. The model assumed fully turbulent, incompressible flow for simplicity since the addition of a region of laminar flow and compressibility effects would only have increased the boundary layer thickness. The model used the CFD computed, small-scale inlet AIP Reynold's number at cruise massflow for the Reynold's number at the leading edge of the sensor array ($1 \times 10^6$). Although this Reynold's number value was clearly an overestimate because the distance to the separation point was much less than the distance to the AIP, it makes the model more conservative by underestimating the actual boundary layer thickness. The displacement thickness ($\delta^*$) and the momentum thickness ($\theta$) predicted by the model are 377μm and 195μm respectively. Using the approximate relation between the momentum thickness and the boundary layer thickness ($\delta$) derived for a flat plate turbulent boundary layer, $\theta/\delta \cong 0.0972$ [25], the boundary layer thickness

at the leading edge of the sensor array is of the order of 2 millimeters, more than 17 times larger than the thickness of the sensor array.

### *2.2.2 Installation*

The first step in the installation of the hot film array was to cut away the excess substrate, yielding the shape shown in Figure 2-4, a triangular region with the sensors themselves and five thin fingers of leads running from each side. Next, the surface was roughed using fine sandpaper (400 grit) and cleaned thoroughly with isopropyl alcohol in order to maximize the effectiveness of the adhesive. The adhesive used was Morgan Adhesives Company's MACtac® IF-2012. IF-2012 is a 0.002 inch thick acrylic, pressure sensitive adhesive film. This adhesive can be removed from the inlet without damaging the inlet surface by using a small amount of acetone to dissolve it. The adhesive sheet was cut to the same shape but slightly larger than the array itself. Alignment of the array was performed using a reference mark on the array at the coordinate origin shown in Figure 2-3. The coordinate origin reference mark was aligned with static pressure port 225 on the inlet surface. The right angle corners between the interior inlet wall and the upper surface of the inlet piece were rounded to allow the lead fingers to turn the corner smoothly. The fingers were laid into 0.025 inch deep grooves milled into the upper surface of the inlet piece. Once the wires were connected to the array, the grooves milled in the surface of the inlet piece were filled in with RTV sealant to prevent airflow through them during operation of the inlet. Finally, the excess adhesive was rubbed with a soft cloth to remove it from the around the edges of the array.

Lead wires, 0.018 inch OD, were soldered to the ends of the sensor array leads and carried through the grooves in the top surface to 5 "D" connectors attached to brackets on either side of the inlet for strain relief. The wiring scheme for the sensor array is detailed in Appendix A. From the "D" connectors, 5 meter long RG-58A/U coaxial wires were run to 18 DANTEC 56C17 CTA anemometers. The 5 meter cable length is required to provide the correct impedance to ensure proper dynamic operation of the CTA bridge. Table 2-3 below gives the internal CTA settings used.

| Hot Film Sensor Coordinates | | | |
|---|---|---|---|
| Sensor Number | Sensor Resistance (Ω)* | X-Coordinate (cm) | Y-Coordinate (cm) |
| 1 | 7.1 | 0.59 | 1.00 |
| 2 | 7.2 | -0.59 | 1.00 |
| 3 | 7.3 | 1.16 | 1.96 |
| 4 | 7.3 | 0 | 1.96 |
| 5 | 7.5 | -1.16 | 1.96 |
| 6 | 7.3 | 1.79 | 2.73 |
| 7 | 7.2 | 0.53 | 2.73 |
| 8 | 7.2 | -0.53 | 2.73 |
| 9 | 7.3 | -1.79 | 2.73 |
| 10 | 7.4 | 2.37 | 3.64 |
| 11 | 7.2 | 1.17 | 3.64 |
| 12 | 7.1 | 0 | 3.64 |
| 13 | 7.2 | -1.17 | 3.64 |
| 14 | 7.9 | -2.37 | 3.64 |
| 15 | 7.6 | 3.04 | 4.46 |
| 16 | 7.2 | 1.90 | 4.46 |
| 17 | 7.2 | 0.50 | 4.46 |
| 18 | 7.3 | -0.50 | 4.46 |
| 19 | 7.3 | -1.90 | 4.46 |
| 20 | 7.7 | -3.04 | 4.46 |
| 21 | 7.8 | 2.73 | 5.19 |
| 22 | 7.2 | 1.41 | 5.19 |
| 23 | 7.2 | 0 | 5.19 |
| 24 | 7.4 | -1.41 | 5.19 |
| 25 | 7.7 | -2.73 | 5.19 |
| 26 | 7.4 | 2.73 | 5.64 |
| 27 | 7.2 | 1.41 | 5.64 |
| 28 | 7.2 | 0 | 5.64 |
| 29 | 7.2 | -1.41 | 5.64 |
| 30 | 7.6 | -2.73 | 5.64 |

*Measured by manufacturer at room temperature

Table 2-2. Hot Film Sensor Coordinates
(Measured from the Coordinate Origin in Figure 2-3).

| DANTEC 56C17 CTA Internal Settings | |
|---|---|
| Servo-Amplifier Gain | 166 (AC), 3470 (DC) |
| Servo-Amplifier Filter | 25 kHz |
| Amplifier Frequency Response Shape | Film (3dB/octave) |
| Cable Length Impedance Compensation | 5 Meters |

Table 2-3. CTA Internal Settings.

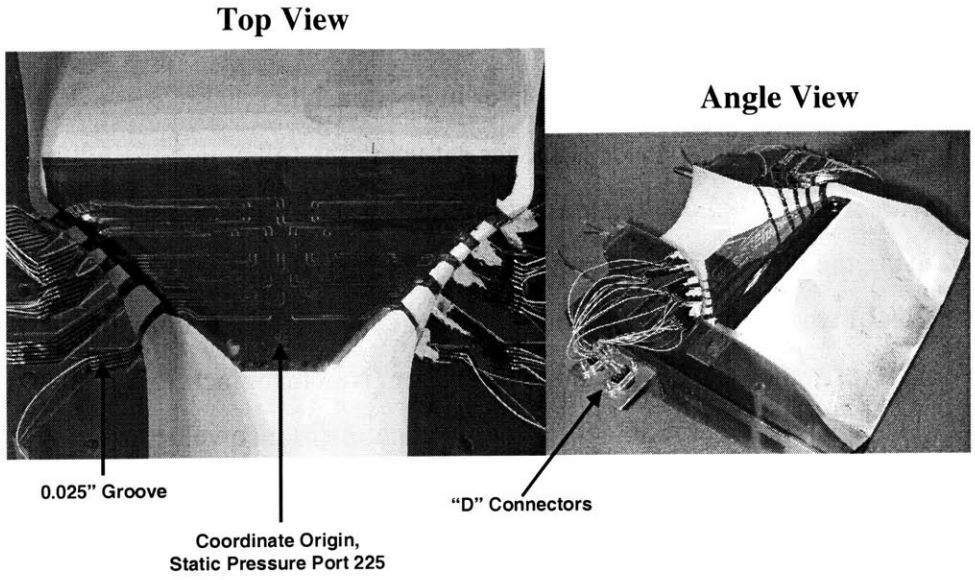


Figure 2-4. Installed Hot Film Sensor Array.

The CTAs were connected to signal conditioners in order to AC couple and amplify the CTA output voltages. Because enough signal conditioners of a single type were not available, the CTAs were connected to two different types of signal conditioners, 9 DANTEC 56N20 Signal Conditioners and 9 Measurements Group, Inc. Model 2300 Strain Gauge Conditioning Amplifiers. Appendix A shows which CTAs were connected to which type of signal conditioners. For a common input signal from a hot film CTA, the output signals of the two different types of signal conditioners were compared and found to be identical (except for the negligible effect of slightly different highpass filter settings). For the hot film sensor signals, both types of signal conditioners were operated in AC coupled mode with a lowpass frequency cutoff of 10 kHz and a gain of 10. For the DANTEC 56N20s, the highpass frequency cutoff was set to 1 Hz. No variable highpass setting was possible for the Model 2300s.

### *2.2.3 Operation*

Operation of the hot film sensors was conducted at the highest overheat ratio (sensor temperature) which would not cause significant degradation of the sensor element resistance, in order to achieve the maximum possible sensitivity to changes in the surface shear stress as well as to reduce the effects of temperature fluctuations in the freestream.

An overheat ratio of 1.5 was selected, corresponding to an approximate sensor temperature of 150°C. The effect of higher overheat temperatures on the resistance of the SENFLEX® sensor elements is discussed later in Section 7.1.

The CTA overheat resistance ($R_h$) was set using the following procedure. First, the sensor with all leads and cabling was attached to the CTA and its resistance was calculated using the internal resistance measurement capability of the CTA. Once this resistance ($R+R_l$) was known, the lead and cable resistance ($R_l$) was computed using the sensor element resistance (R) provided by the sensor array manufacturer and listed in Table 2-2. Using an overheat ratio of 1.5, the overheat resistance value set into the CTA bridge is given by:

$$R_h=1.5R+R_l. \qquad \text{(Equation 2.1)}$$

No calibration was performed on the hot film sensor array. Since the intent of the experiment was not the accurate measurement of flow velocity or surface shear stress, but only the relative response of the sensor elements, a calibration was not required. All that was required was that the sensors respond in a similar manner to similar changes in the flow. It is assumed that using an array of identical sensor elements (all fabricated from the same electron-beam deposited sheet of Nickel film) with similar resistances and the same overheat ratios ensured that the individual sensors behaved in approximately the same manner. It is also important to note that due to the complexity of the flow inside the inlet, an accurate calibration was not practical.

### *2.3 AIP Total Pressure Probes*

Three total pressure probes were placed in the sensor ring downstream of the inlet to measure the unsteadiness of the flow at the AIP. The design and operating characteristics of the AIP total pressure probes are detailed in Warfield's thesis [22]. It is important to note that the total pressure probes provided useful information only up to 1000 Hz due to the presence of an acoustic half-wave mode at 1500 Hz. Figure 2-5 is a photograph of the sensor ring with the three sensor probes installed.

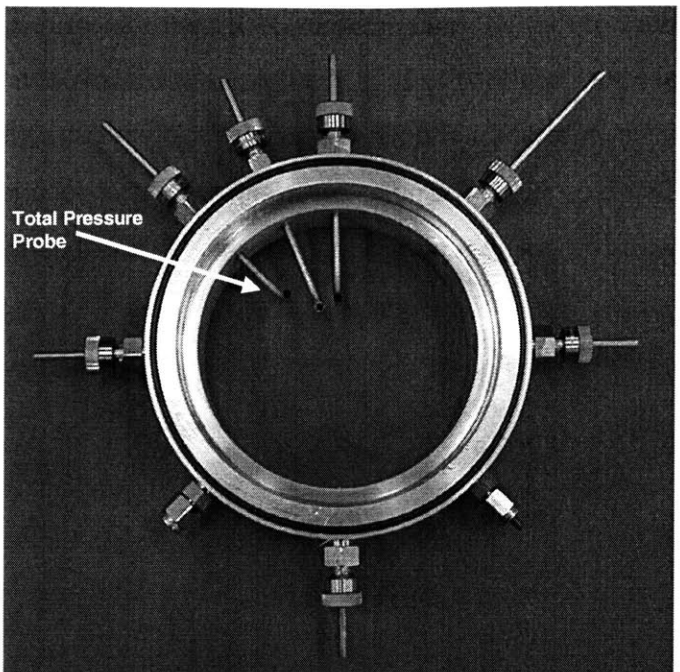

Figure 2-5. AIP Total Pressure Probe Sensor Ring.

To measure the unsteady total pressure, Kulite pressure transducers (±5 psi range) were attached to the three total pressure probes and operated using Measurements Group, Inc. Model 2300 Strain Gauge Conditioning Amplifiers. The conditioning amplifiers were operated using an excitation of 5 volts, a low pass filter setting of 10 kHz, and gains of 100 for the first test and 200 for the second and third tests. Since the objective of the experiments was the correlation of the hot film signals to the AIP signals, the Kulite signals were AC coupled and no attempt was made to measure the actual total pressure at the AIP measurement locations. Therefore, no calibration was performed on the total pressure transducers.

Since the intent of the experiment was to find correlations in the unsteady hot film signals with unsteady signals at the AIP, the AIP total pressure probes were located at positions on the AIP showing the maximum level of unsteadiness. Previous small-scale inlet experiments conducted by Warfield [22] showed that the highest levels of unsteadiness at the AIP were located on the edge of the AIP total pressure deficit. Figure 2-6 below shows the steady total pressure profile of the AIP at various massflows measured using the Northrup-Grumman instrument can shown in Figure 2-1. The numbers of the total pressure probes in the instrument can are overlaid on the plots in Figure 2-6 for reference. From Figure 2-6, locations 1, 7, and 37 were the best locations

for seeing the boundary of the AIP total pressure deficit for the entire range of massflows. For the experimental tests, locations 1, 2, 7, 37, the mid-point between locations 2 and 37, and a point between locations 1 and 37 were used variously as the locations for the sensor ring total pressure probes. The polar coordinates of these locations relative to the center of the duct (with zero angle representing the vertical) are shown in Table 2-4 below.

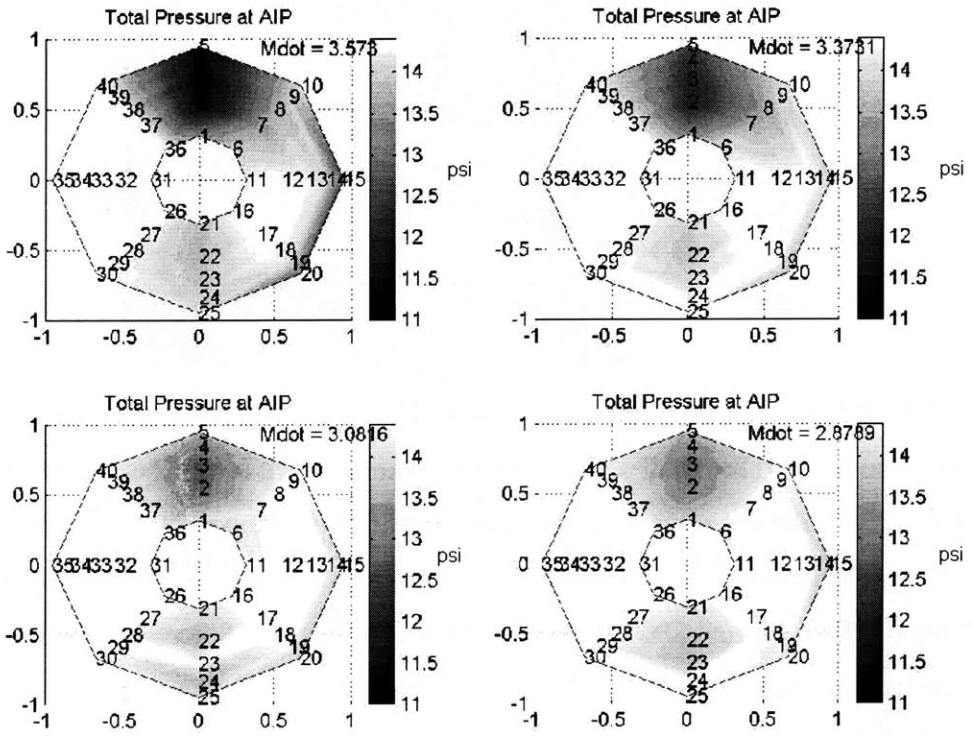


Figure 2-6. AIP Total Pressure Profile.

| Total Pressure Probe Polar Coordinates | | |
|---|---|---|
| Probe Location (*Fig 2-6*) | Angle | Radius (inches) |
| 1 | 0° | 0.628 |
| 2 | 0° | 1.096 |
| 7 | 45° | 1.096 |
| 37 | -45° | 1.096 |
| Between 1-37 | -22.5° | 0.770 |
| Midpoint 2-37 | -22.5° | 1.013 |

Table 2-4. Total Pressure Probe Polar Coordinates

### *2.4 Mass Flow Determination*

The mass flow through the inlet was determined using a calibration curve for the mass flow plug provided by Northrup-Grumman and updated by Warfield. The mass flow plug's position in inches ($\chi$) is indicated by a voltage output signal (V) from the plug. Warfield's calibration equations relate the reference mass flow ($\dot{m}^*$) to the plug position and are:

$$\chi = 0.50398V - 0.29231 \text{ (in)}, \qquad \text{(Equation 2.2)}$$

$$\dot{m}^* = -0.0068\chi^4 + 0.049\chi^3 - 0.0201\chi^2 + 1.355\chi - 0.016 \text{ (lb/s)}. \qquad \text{(Equation 2.3)}$$

The reference mass flow ($\dot{m}^*$) is the mass flow at a reference temperature (T*) of 295.9 Kelvin and a reference pressure (p*) of 14.7 psi. The reference mass flow was then adjusted due to the actual test conditions to get the actual mass flow ($\dot{m}$) using the relation:

$$\dot{m} = \dot{m}^* \left( \frac{p}{p^*} \right) \sqrt{\frac{T^*}{T}} \qquad \text{(Equation 2.4)}$$

where p and T are the actual test condition ambient pressure and temperature.

In order for this calibration to be accurate, two conditions must be met. First, the instrument can shown in Figure 2-1 must be attached to the mass flow plug. Second, the flow through the plug must be choked. To ensure the plug is choked during the tests, the pressure ratio of the ambient static pressure to the static pressure in the reservoir downstream of the mass flow plug is maintained at a value of at least 2. The ambient pressure is measured using a SETRA absolute pressure transducer. The downstream reservoir pressure is measured using a static pressure tap drilled in the air ducting downstream of the inlet leading to the De-Laval compressor with a Scanivalve 48CMK3 pressure transducer. The calibration relating the Scanivalve output ($S_{out}$) to the actual gauge pressure ($P_g$) in psi was determined experimentally and is shown below:

$$P_g = 0.14565V_s + 0.009344. \qquad \text{(Equation 2.5)}$$

### *2.5 Data Acquisition*

Data acquisition of the voltage signals from the signal conditioners for the hot film sensors and the total pressure sensors was performed using an ADTEK AD-380 12-bit analog to digital high speed data acquisition system controlled by a DOS based software

interface. The ADTEK system had 4 data acquisition boards, each with 8 channels. For each measurement, 32 channels of data were taken at an acquisition rate of 20 kHz. The buffer size was 32768 bytes with a buffer count of 200 per measurement, corresponding to 102,400 data points or 5.12 seconds per channel. The maximum signal input range was ±5 Volts. In order to ensure that the data acquisition system and the associated computer codes for reduction of the raw data were operating correctly, a 500 Hz sine wave with a 3.0 Volt amplitude was input into board 3, channel 8 and board 4, channel 1.

# 3 Small-Scale Inlet Experimental Results

Small-scale inlet experiments were conducted with three different hot film and AIP total pressure sensor configurations at several different mass flows ranging from 2.1 lb/s to 3.7 lb/s. In order to assess repeatability, several sensors and mass flows were common to all three configurations. The details of the sensor configuration for each experiment are contained in Appendix B. The small-scale experimental results are divided into three sections: a general discussion of the sensor RMS results, the determination of the separation intensity, and the correlation of the hot film and the AIP total pressure data.

## *3.1 Sensor RMS Results*

The RMS for each sensor at each massflow was computed by taking the RMS of the entire 5.12 second time trace of the AC coupled sensor output voltage from the signal conditioner. Examination of the sensor RMS results along with the flow visualization results shown in Figure 2-2 lends some insight into the overall behavior of the separated flow region. Figure 3-1 below shows an interpolated surface plot of the sensor RMS for the array at various mass flow values. Since data could only be taken on 18 sensors during an experimental run due to the number of available CTAs, in order to show the entire array the plot combines data from the second and the third experimental runs (detailed in Appendix B). Note that the dots indicate the locations of the sensors used to create the plot.

In general, the RMS of all of the hot film sensors increased as the massflow was increased from 2.1 lb/s to 2.9 lb/s. However, as the massflow was increased above 2.9 lb/s, the RMS of the sensors generally decreased. This RMS trend indicates that the separation, although becoming stronger, also became steadier as the massflow increased above 2.9 lb/s. It should also be noted that for the entire range of massflows, the center of the stagnation line at the leading edge of the separated region (sensors 28 and 23, see Figure 2-3) was consistently an area of very high RMS, and therefore very high unsteadiness, relative to the rest of the separated region.

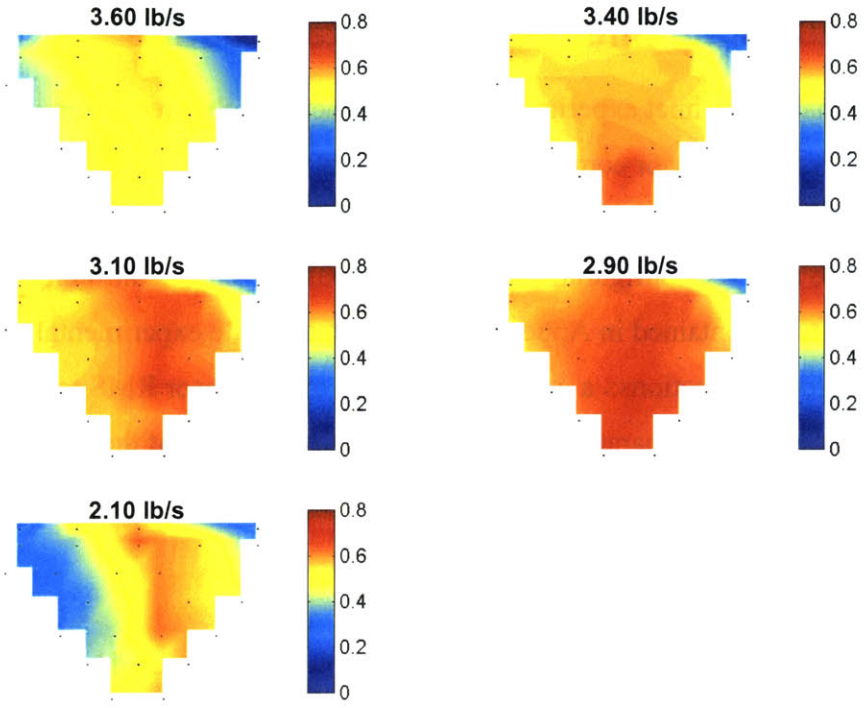


Figure 3-1. Hot Film Sensor RMS.

Figure 3-1 shows a slight span-wise asymmetry. This asymmetry occurs also in the flow visualization results shown in Figure 2-2. Of particular interest is sensor 26 on the far left side of stagnation line (see Figure 3-2 below). Notice that the flow visualization results, particularly the 3.68 lb/s massflow case, indicate that as the massflow increased, the stagnation line increased in span-wise extent asymmetrically with a slight angle on one side. As shown below in Figure 3-2, this slight angle in the stagnation line placed sensor 26 further upstream of the stagnation line than any of the other sensors, resulting in it seeing a much steadier flow. Therefore, the fact that sensor 26 had the lowest RMS of any sensor in the array throughout the entire range of massflows was most likely due to the span-wise asymmetry in the separation.

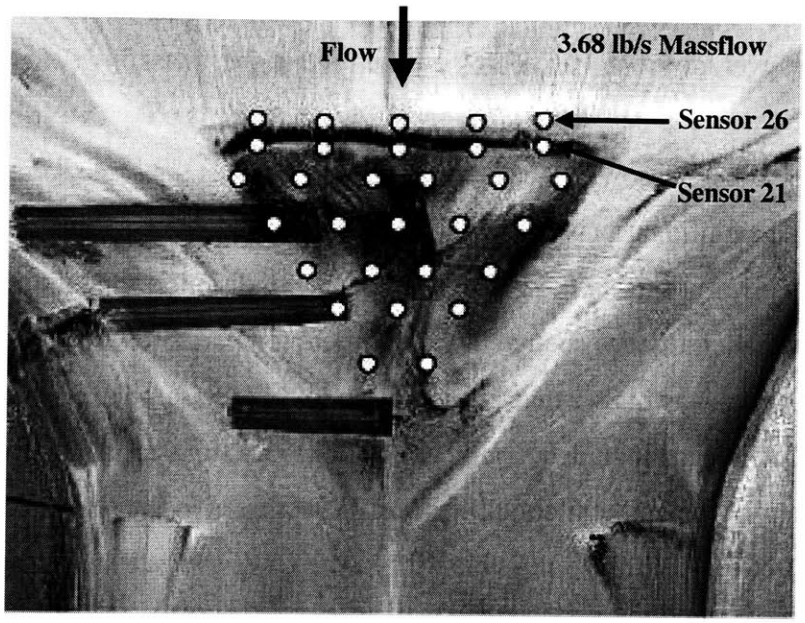


Figure 3-2. Hot Film 26 Location.

In order to assess the errors associated with the hot film sensor measurements, several sensors were common to all of the experimental runs as a basis for comparison. Also, in order to assess the variations within each experimental run, after all of the data had been taken for each massflow value of interest, several of the massflow values were repeated. For the case of repeated massflows within a single experimental run, the mass flow plug was set in exactly the same position (the voltage reading from the plug was identical in both cases to within 10 millivolts, corresponding to a maximum error of 0.25% in the massflow) and the ambient pressure and temperature were identical. For these cases, the percent differences in the RMS results for all of the sensors on the array were very low. For example, comparing the repeated 3.1 lb/s and 3.4 lb/s massflow cases for both the second and third experimental runs yielded a maximum difference of 2.6% and a mean difference of 1.0% for all of the sensors used. This variation was most likely the result of both minor differences in the inlet massflow and random noise in the separated flow region. However, comparison of the common sensors from different experimental runs at the same massflow yielded larger variations.

Figure 3-3 below shows the RMS versus massflow data points for each of the common sensors between the second and third experimental runs. Figure 3-3 shows that the variation in the sensor results between runs is low for massflows lower than 3.4 lb/s.

The average sensor RMS variation for massflows less than 3.4 lb/s, neglecting sensor 2, was 2.6%. The average RMS variation including the higher massflows, neglecting sensor 2, was 5.3%. Sensor 2 is neglected since from Figure 3-3 it is clear that it is an outlier compared to the other sensors. The data trend for sensor 2 is the same for both runs, but the data shows a significant bias error between the runs. This bias error was most likely due to a human error in setting the gain of the signal conditioner or an internal failure in the CTA causing a significant change in the overheat temperature. The variation for each sensor between runs was higher than the variation within the same run because comparing different runs included a number of additional small errors such as errors in the measurement of the ambient conditions, small decreases in the sensor resistances due to aging (see Section 4.3.3), and possible drift in the CTA overheat resistances or signal conditioner gains. Note that no changes were made to the CTAs, signal conditioners, wiring, or the inlet itself between runs 2 and 3. The results shown in Figure 3-3 indicate that the sensor data was reasonably repeatable, particularly for massflows less than 3.4 lb/s.

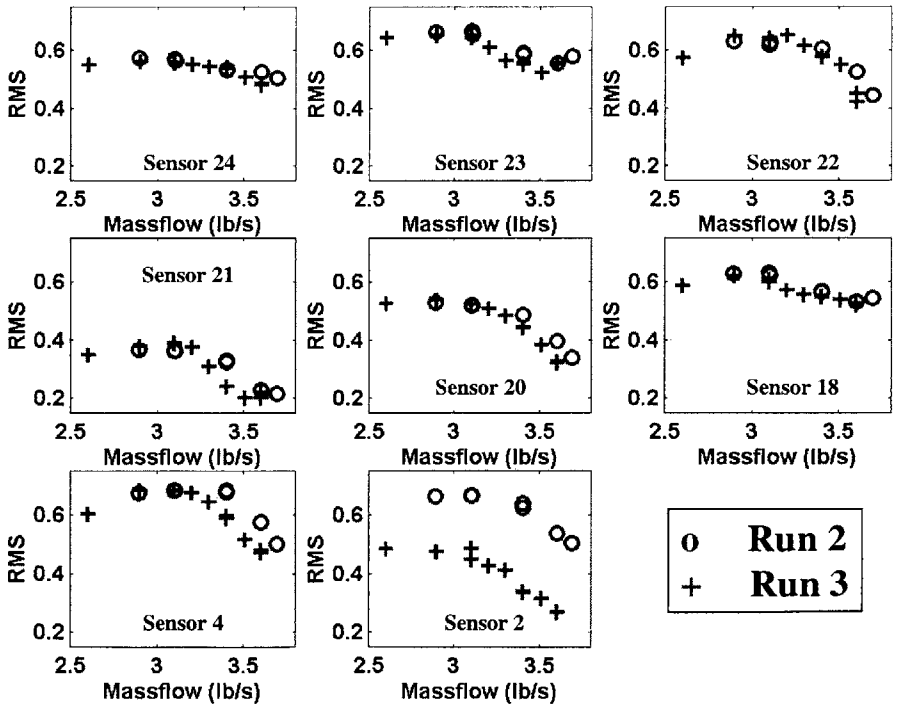


Figure 3-3. Hot Film Sensor RMS Variation.

### *3.2 Determination of the Separation Intensity*

The RMS results indicated that the hot film sensors can provide information about the steady characteristics of the separation such as the resulting pressure recovery at the AIP. Since the UCAV cruise condition corresponds to a small-scale mass flow of 3.12 lb/s, the massflow range from 2.9 lb/s to 3.6 lb/s was considered sufficient to cover the majority of the UCAV operating conditions. In this massflow range, there are several hot film sensors that exhibited a monotonically decreasing RMS value with increasing massflow. This relationship between sensor RMS and massflow, and also therefore between RMS and pressure recovery at the AIP, was examined for each of these sensors individually and in combination. Although there are several sensors which could have been used, the results shown below in Figure 3-4 are for an average of the RMS of sensors 22 and 24, located just behind the stagnation line at the leading edge of the separation (see Figure 2-3), because their average had the least variation between experimental runs. Figure 3-4 shows the average RMS of sensors 22 and 24 plotted against the inlet pressure recovery for the second and third experimental runs.

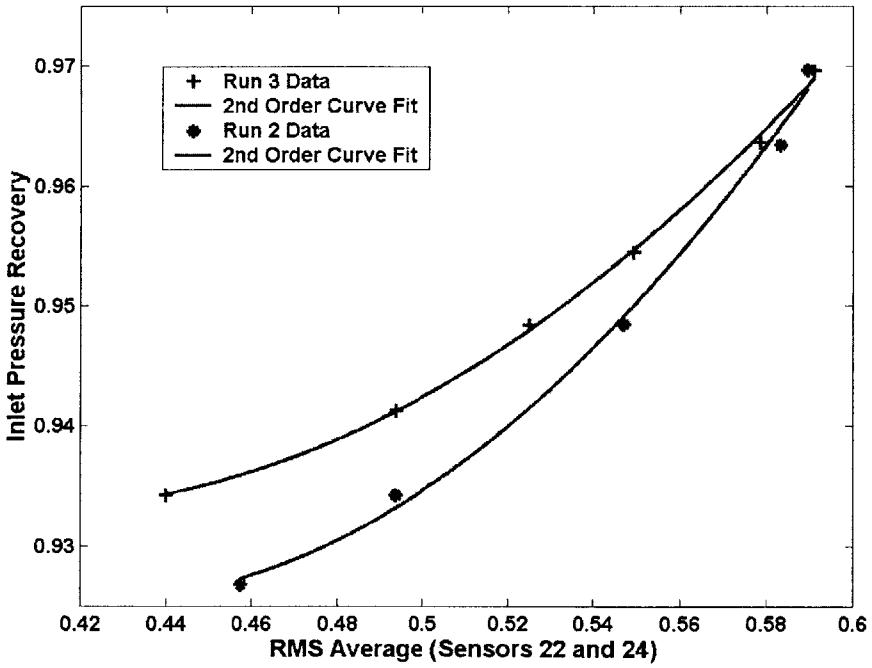


Figure 3-4. Inlet Pressure Recovery.

The pressure recovery at the AIP was computed using an empirical relationship provided by Northrup-Grumman:

$$PR = -0.041\dot{m}^2 + 0.0216\dot{m} + 0.688 \qquad \text{(Equation 3.1)}$$

where PR is the inlet pressure recovery and $\dot{m}$ is the inlet massflow in lb/s.

Although more data is required to rigorously quantify the accuracy of the relationship shown in Figure 3-4, it is clear that a quantifiable relationship exists which could provide an indication of the inlet pressure recovery to within better than 1% of the actual value.

### *3.3 Unsteady Hot Film Sensor to AIP Correlation*

As expected from the earlier small-scale experiments described in Section 1.2, the hot film sensor and the AIP total pressure sensor data indicated the presence of a characteristic frequency. The exact value of the characteristic frequency was difficult to determine accurately due to the noise in the sensor signals and the fact that the characteristic was not always a clear spike but an elevated range. The frequency does however increase with increasing massflow. Figure 3-5 below shows the frequency spectrum for hot film sensor 21 (located on the far side of the leading edge stagnation line, see Figure 2-3) and AIP total pressure probes at locations 7 and 37 (on opposite sides of the AIP) in the third experimental run. Figure 3-5 clearly shows the presence of the characteristic frequency at the hot film sensor at and the AIP as well as its movement with massflow. A characteristic frequency was not discovered in any of the data at or above a massflow of 3.6 lb/s.

For a wide massflow range around the UCAV cruise massflow, 2.9 lb/s to 3.4 lb/s, the hot film sensors were significantly correlated to the AIP total pressure sensors. This correlation existed only the same narrow frequency band as the characteristic frequency. Therefore, in order to determine the correlations between the hot film sensors and the AIP total pressure sensors, both signals were filtered to reduce the noise outside of the characteristic frequency range.

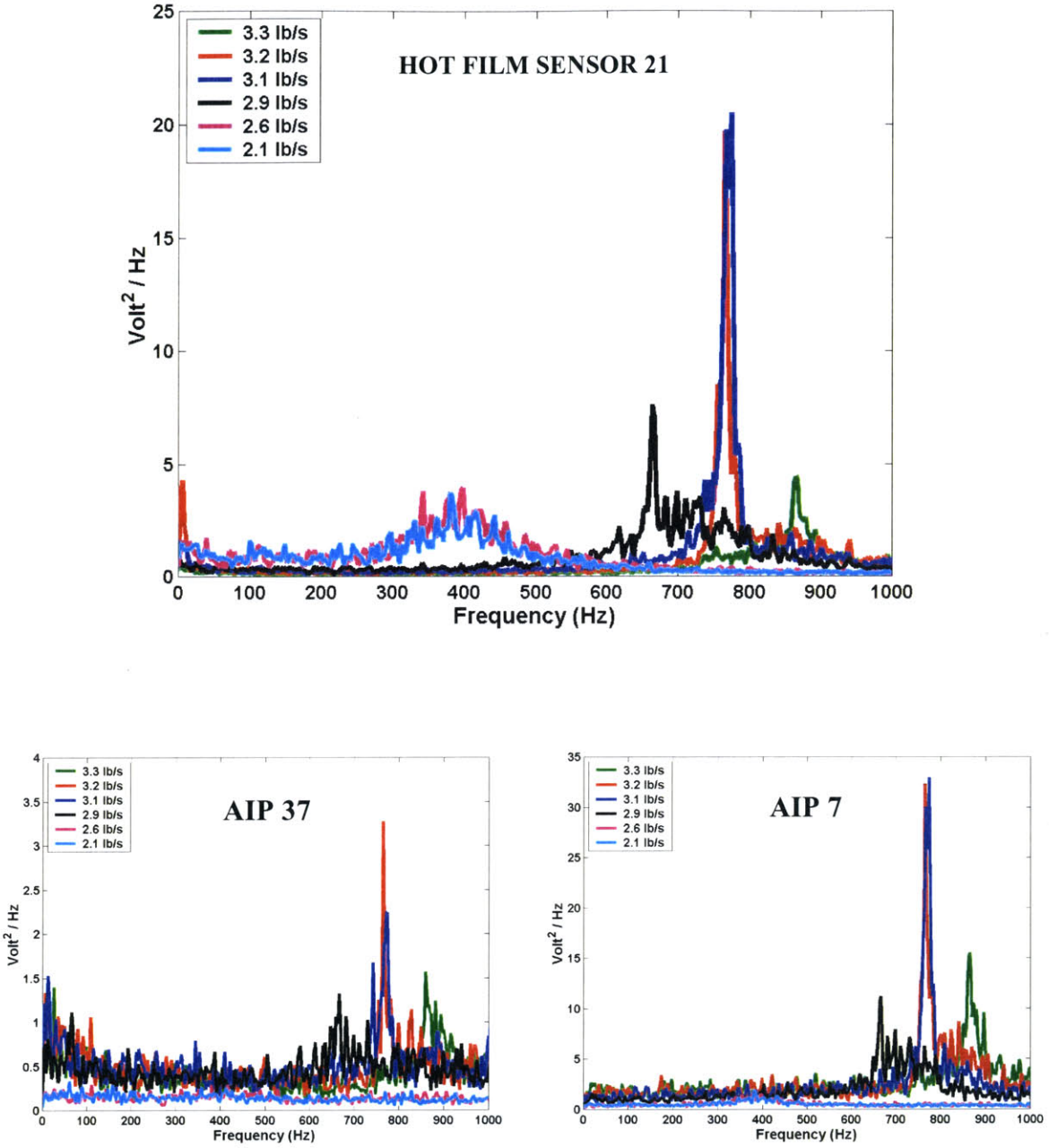


Figure 3-5. Characteristic Inlet Frequency.

The filter used was a fortieth order finite impulse response (FIR) bandpass filter [20]. The width of the bandpass filter was 100 Hz, centered on the peak value of the characteristic frequency for each massflow, which was estimated using the frequency spectra for all of the hot film and AIP sensors. The filter had an attenuation of –0.53 dB at the ends of the bandpass region with a 1440 Hz bandwidth for a –20 dB attenuation. The fortieth order filter was used because it represents the largest filter which could be reasonably applied to the hot film sensor data in real time. The fortieth order filter applied in real time would add a one millisecond lag to any active control system using the filtered data as an input. This filter was tested using two normally distributed random signals to ensure that the artificial increase in the cross-correlation values due to the reduction in the signal bandwidth was not significant.

The signals from the hot film sensors and the AIP total pressure probes were compared by computing the cross-correlation and coherence of each hot film sensor against each AIP probe. The cross-correlation between two different signals is a measure of their statistical correlation (on a scale of –1 to 1) as a function of the time difference between them. From Stearns [20], the cross-correlation between discrete signals *f* and *g* ($\phi_{fg}$) is defined as:

$$\phi_{fg}(n) \equiv \lim_{N\to\infty} \frac{1}{2N+1} \sum_{m=-N}^{N} f_m g_{m+n}. \qquad \text{(Equation 3.2)}$$

To preserve to the scaling of the cross-correlation values between –1 and 1, each signal was normalized by its AC coupled RMS value.

The coherence between two signals is a measure of their correlation (on a scale of 0 to 1) as a function of frequency. Thus, while cross-correlation can show at what relative time delay the signals are highly correlated, coherence can show at what frequencies they are highly correlated. The coherence between two discrete signals f and g ($\Phi_{fg}$) is defined as:

$$\Phi_{fg} = \frac{\left|P_{fg}\right|^2}{P_{ff} P_{gg}} \qquad \text{(Equation 3.3)}$$

where $P_{ff}$ and $P_{gg}$ are the power spectral densities of signals f and g respectively and $P_{fg}$ is the cross spectral density of the two signals. $P_{ff}$, $P_{gg}$, and $P_{fg}$ were computed using Welch's averaged periodogram method using 8 windows [20].

The maximum absolute value of the cross-correlation and the coherence for all of the hot film sensors with the AIP sensors are shown using interpolated surface plots in Figures 3-6 and 3-7. Note that for both figures the filter described above was applied to the hot film and the AIP sensor signals. For Figure 3-6, the cross-correlations and coherence were taken with respect to the AIP total pressure sensor on the same side of the inlet as the sensor (either AIP position 7 or 37). In Figure 3-7, the cross-correlations and coherence of the sensors were all taken with respect to the center AIP total pressure sensor (AIP location 1). Since only 18 sensors could be used during each run due to a limitation in the number of available CTAs, the plots were constructed by combining data from the second and the third experimental runs. The dots on the figures show the locations of the sensors used to the build the plots.

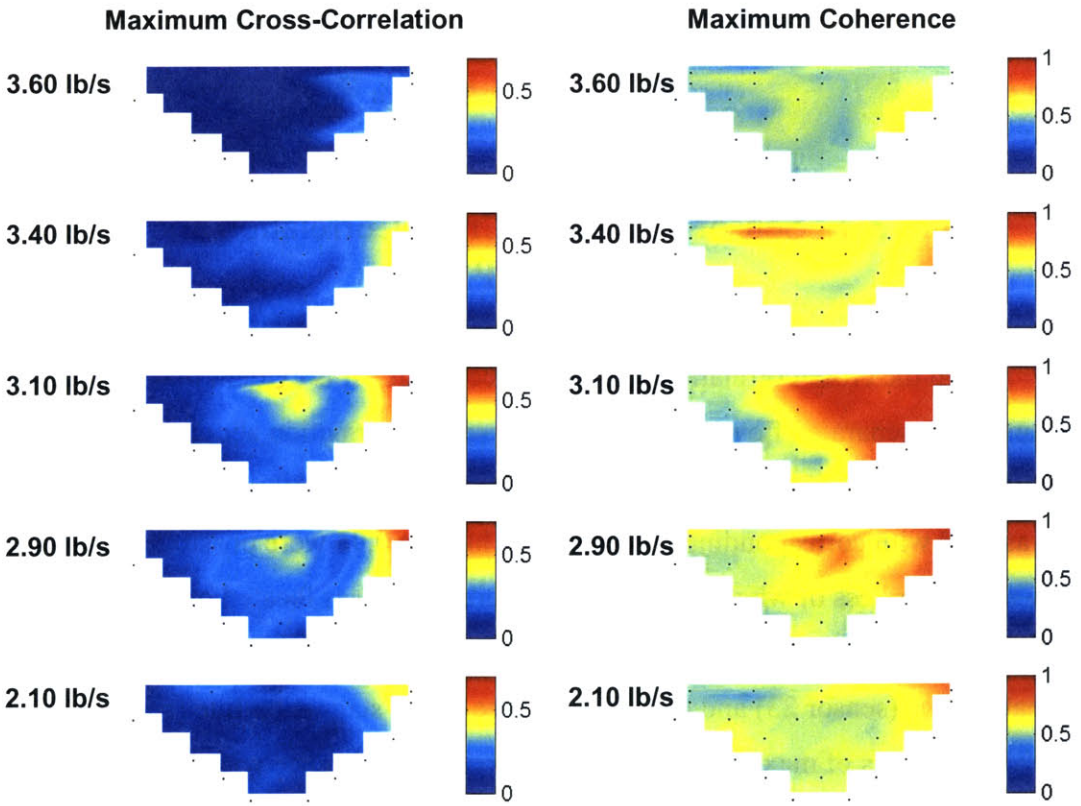


Figure 3-6. Sensor Maximum Cross-Correlation and Coherence (AIP 37& 7).

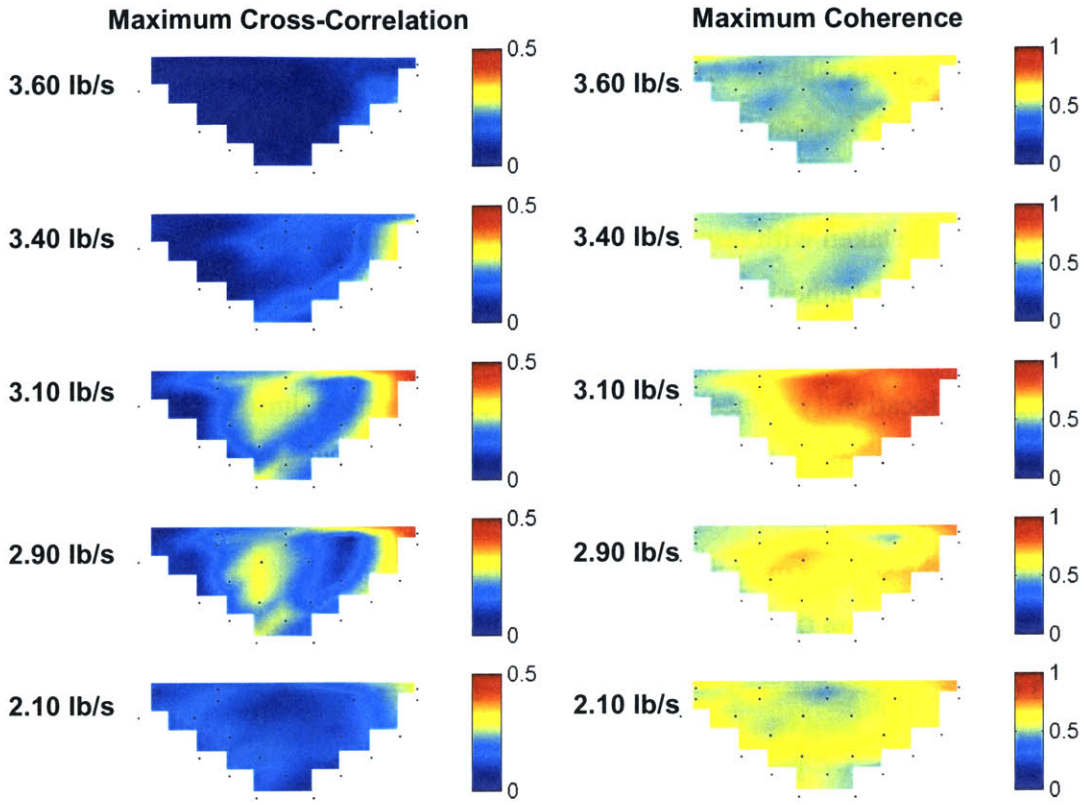


Figure 3-7. Sensor Maximum Cross-Correlation and Coherence (AIP 1).

From the cross-correlation and coherence results, it is evident that the hot film sensors in the separated flow region provided useful information about the unsteady flow conditions at the AIP in the characteristic frequency range as cross-correlation values as high as 0.68 with corresponding coherences as high as 0.95 were possible. The results show that regardless of whether the total pressure probe was located on the side or at the bottom center of the AIP total pressure deficit, the region just behind the center of the stagnation line (sensor 23) and the leftmost edge of the stagnation line (sensors 21 and 26) were the areas of maximum cross-correlation and coherence with the AIP. It is important to note that the cross-correlation and coherence (as well as the strength of the characteristic frequency in the sensor frequency spectra as shown in Figure 3-5) reached a maximum at a massflow of 3.1 lb/s. The correlation and coherence between the hot film sensors and the AIP decreased along with the flow unsteadiness as the massflow increased or decreased away from 3.1 lb/s. Since the cruise massflow of the UCAV corresponds to a small-scale inlet massflow of 3.12 lb/s, the hot film sensors were

significantly correlated to the unsteady regions of the AIP for a wide range of massflows around the cruise massflow (2.9 lb/s to 3.4 lb/s).

The cross-correlation plots of Figures 3-6 and 3-7 also show a span-wise asymmetry similar to the asymmetry in the RMS results discussed previously. As shown above in Figure 3-2, the asymmetry in the separated flow region seen in the shape of the stagnation line is one possible explanation for the span-wise asymmetric cross-correlations in sensors 21 and 26 on the far edge of the stagnation line.

Figures 3-8 through 3-11 below show the cross-correlation and the coherence for two highly correlated sensors (21 and 23) against AIP location 7 with the filter applied to both signals. Sensor 21 has a maximum cross-correlation and coherence of 0.68 and 0.95 respectively. Sensor 23 has a maximum cross-correlation and coherence of 0.49 and 0.96 respectively.

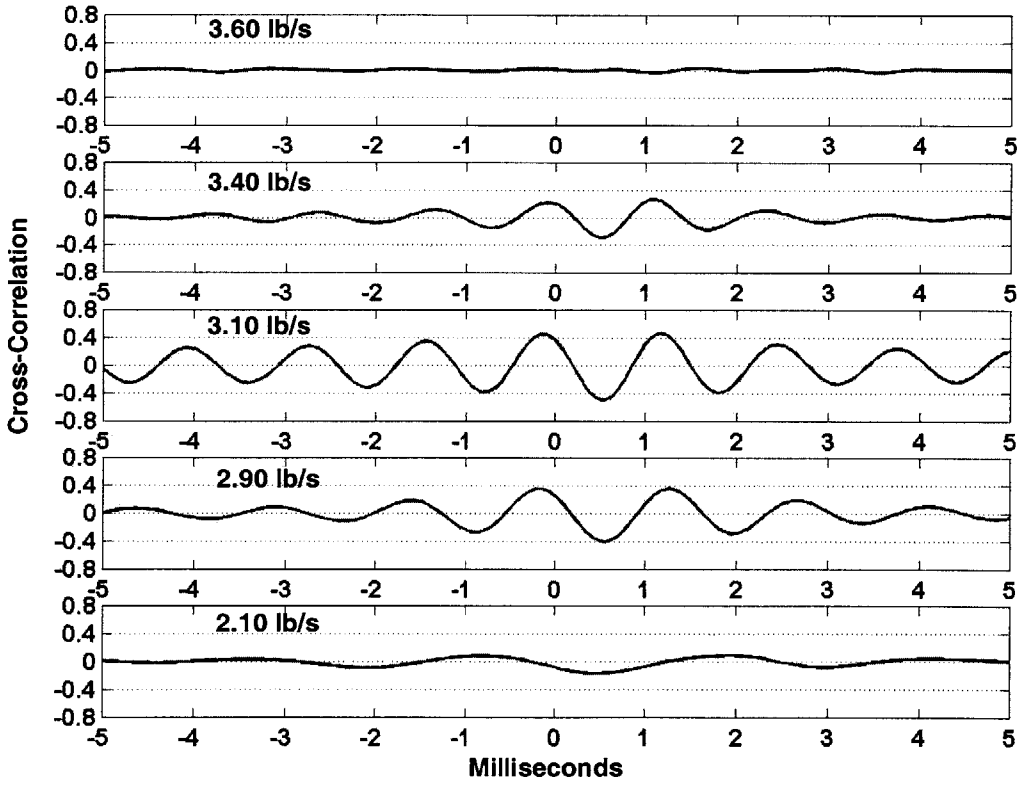


Figure 3-8. Sensor 23 & AIP 7 Cross-Correlation.

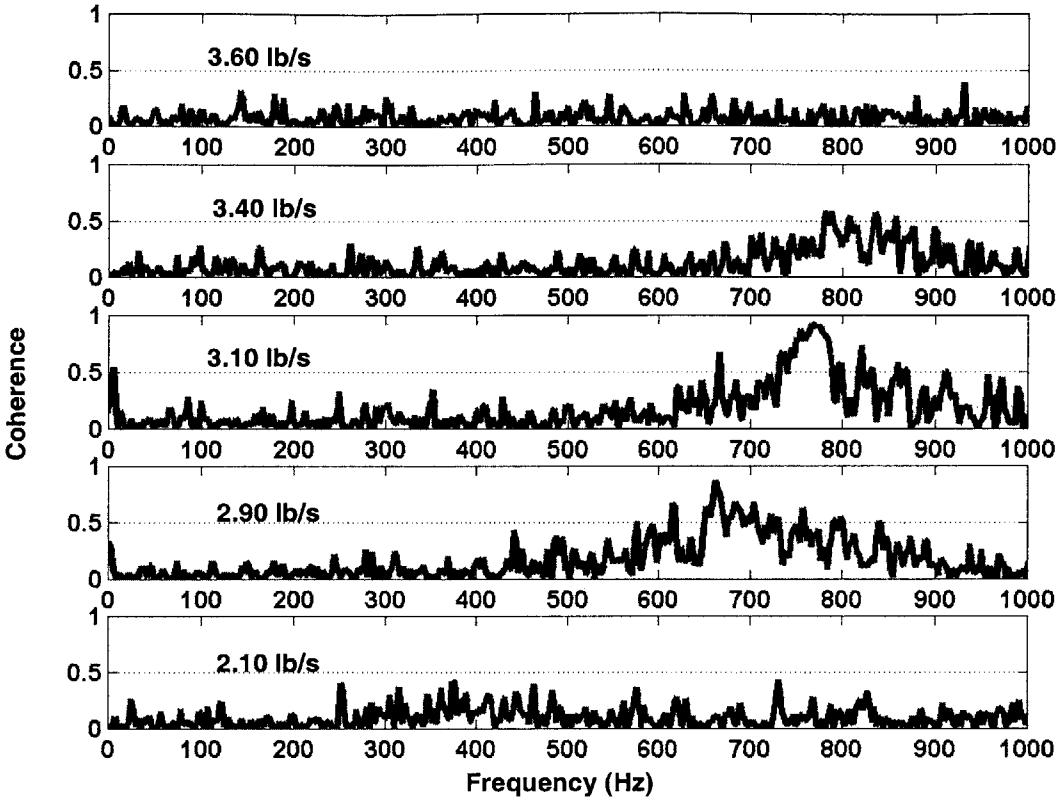


Figure 3-9. Sensor 23 & AIP 7 Coherence.

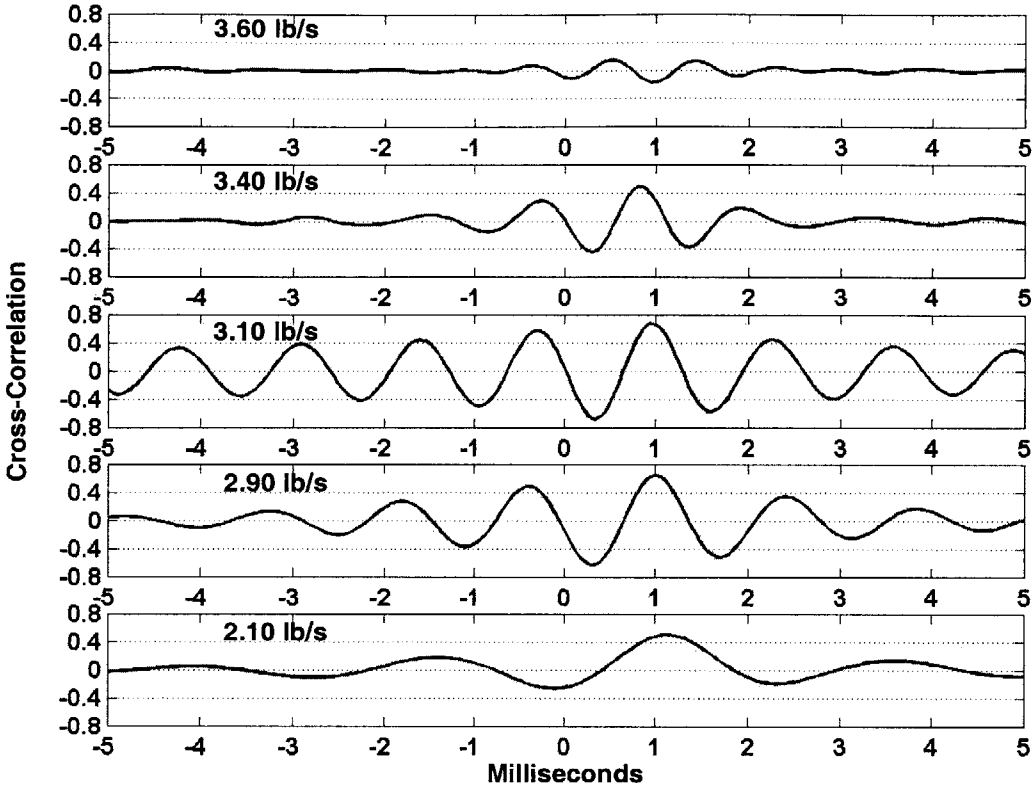


Figure 3-10. Sensor 21 & AIP 7 Cross-Correlation.

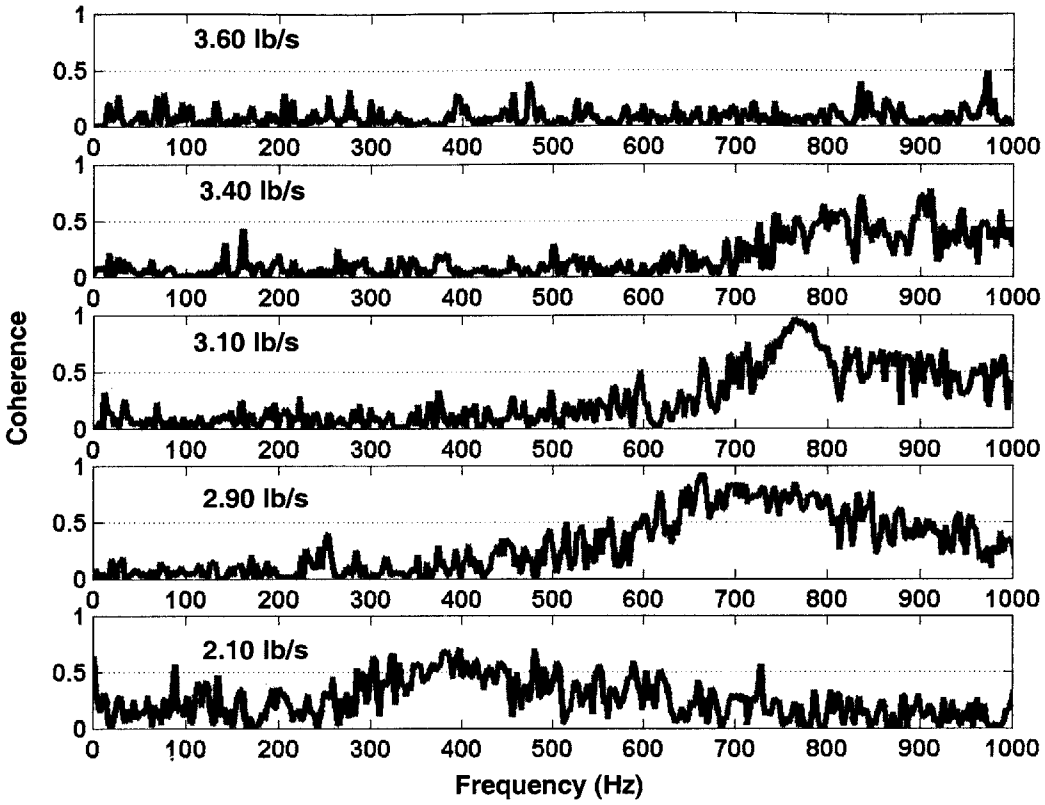


Figure 3-11. Sensor 21 & AIP 7 Coherence.

For the sensors which are significantly correlated to the AIP, the fact that the peak values of the cross-correlations occurred at positive times indicated that the hot film sensors saw the periodic disturbance associated with the characteristic frequency in advance of the AIP. This trend allows the hot film sensors to predict the unsteadiness in the characteristic frequency range at the AIP.

An analysis of the delay between the hot film sensors and the AIP probes shows that the delays were very consistent with a convective phenomenon and inconsistent with an acoustic phenomenon. Therefore, as postulated by Warfield, the characteristic frequency was most likely the result of periodic vortex shedding from the separated flow region. The delay was measured on the cross-correlation plots as the time (x-axis distance) from the origin to the point of maximum cross-correlation. Table 3-1 below shows the delay results for three significantly correlated sensors at 3.1 lb/s massflow. Note that the analysis assumes a 0.272 millisecond delay in the total pressure probe, a

192 m/s average flow velocity, and a 523 m/s downstream acoustic wave velocity as calculated by Warfield for the 3.1 lb/s case [22].

| Hot Film Sensor to AIP Time Delay Analysis | | | | | | |
|---|---|---|---|---|---|---|
| Sensor | Runs | AIP Probe | Distance (cm) | Estimated Delay for Acoustic Signal (ms) | Estimated Delay for Convective Signal (ms) | Average Measured Delay (ms) |
| 23 (center) | 2,3 | 1(center) | 11.9 | 0.50 | 0.89 | 1.00 |
| 21 (left-side) | 3 | 7(left-side) | 12.2 | 0.51 | 0.91 | 0.95 |
| 4 (center) | 2,3 | 1(center) | 8.8 | 0.44 | 0.73 | 0.70 |

Table 3-1. Hot Film Sensor to AIP Time Delay Analysis.

The left-right periodicity in the vortex shedding from the separated flow region was explored by taking the cross-correlation for all of the hot film sensors against AIP location 37. Figure 3-12 shows the cross-correlation for each hot film sensor against AIP location 37 at zero time lag with the filter applied to both signals. The cross-correlation value was taken at zero time lag in order to show the simultaneous relationship of all of the hot film sensors to AIP 37. Note that Figure 3-12 is a composite of data taken in the second and third experimental runs.

Figure 3-12 shows that the separated region had areas of positive and negative correlation with the AIP sensor. At a massflow of 3.60 lb/s, the majority of the left side of the inlet was positively correlated with the AIP sensor while the majority of the right side was negatively correlated with the AIP sensor. At lower massflows, the center of the separated region was negatively correlated with the AIP sensor while the edges were positively correlated with the AIP sensor. But, at all of the massflows examined, the extreme left and right edges of the stagnation line at the leading edge of the separation were oppositely correlated with the AIP sensor. This difference in the cross-correlation suggests that vortices were shedding alternately from the positively and negatively correlated areas.

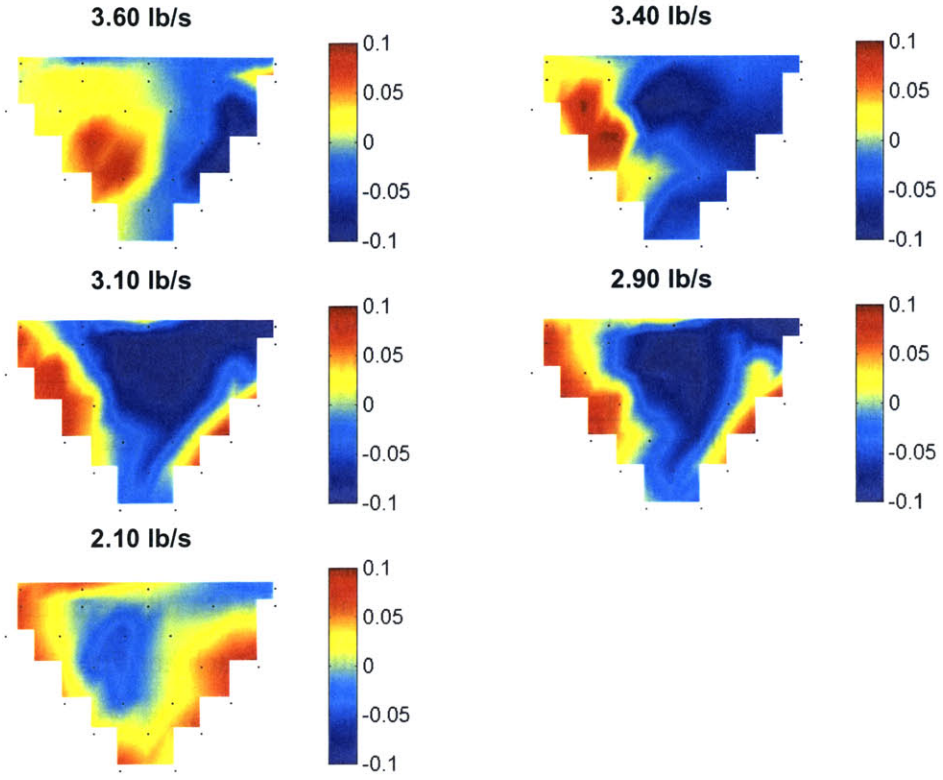


Figure 3-12. Hot Film Sensor Cross-Correlation to AIP 37.

## 3.4 Conclusions

Using both sensor RMS and the strength of the characteristic frequency peak to measure unsteadiness, the unsteadiness in the inlet was found to be a function of the massflow. The maximum unsteadiness occurred in the inlet near the scaled UCAV cruise massflow of 3.12 lb/s. The lag time from the hot film sensors to the AIP probes indicated that the characteristic frequency in the inlet was consistent with a periodic convective disturbance traveling downstream from the hot film sensors to the AIP, such as vortex shedding from the separated flow region.

Hot film sensors positioned along the stagnation line at the leading edge of the separated flow region (locations 21, 23, and 26 – see Figure 2-3) were highly correlated to the unsteadiness at the AIP in the characteristic frequency range for massflows from 2.9 lb/s to 3.4 lb/s. Since the disturbance moved downstream from the hot film sensors to the AIP, the hot film sensors provided advanced information about the conditions at the

AIP. The hot film sensors were not significantly correlated to the unsteadiness at the AIP outside of the 2.9 lb/s to 3.4 lb/s massflow range.

Hot film sensors positioned just behind the stagnation line and to either side of the inlet centerline (locations 22 and 24) provided information about the steady state strength of the separation. The average RMS from sensors 22 and 24 was unambiguously related to the pressure recovery of the inlet from 2.9 lb/s to 3.6 lb/s.

Therefore, for unsteady or steady state information about the AIP, the region just behind the center and possibly the span-wise edges of the stagnation line at the leading edge of the separation appear to be the most advantageous locations for the hot film sensors. Also, the sensors just behind the center of the stagnation line (sensors 22, 23, and 24) showed the highest degree of repeatability between runs for the entire range of massflows.

It is important to realize that the fact that the peak unsteadiness and the maximum correlation between the hot film sensors and the AIP occurred in the small-scale inlet at the UCAV cruise massflow may be a feature which is unique to the particular Northrup-Grumman UCAV inlet geometry tested. Additional tests on full-scale short (separating) inlets are required to determine the range of application of the trends shown here.

Finally, the small-scale inlet tests demonstrated that hot film sensors in the separated region of the inlet could predict separation induced unsteady distortion at the AIP. Also, the hot film sensors provided real time information on the steady-state intensity of the inlet separation and therefore the inlet pressure recovery. Furthermore, the results indicated that the best location for the hot film sensors for both high correlation with the AIP and repeatability was just behind the stagnation line at the leading edge of the separated region.

# 4 Sensor Requirements

The first step in the development of a robust hot film sensor is the definition of the requirements the sensor must meet in order to be effective. These requirements are divided into three areas: sensor design life, which defines the minimum useable life of the sensor; environmental requirements, which ensure the sensor can provide consistent results throughout the range of conditions experienced in the aircraft's mission profile; and performance requirements, which ensure that the sensor can provide meaningful data which can be used by active control systems. A summary of all of the requirements is given in Section 4.4. The performance parameters from the UCAV's mission profile that were used in the development of the requirements are shown below in Table 4-1.

| UCAV Mission Profile | |
|---|---|
| Maximum Range | 1000 NM |
| Minimum Ceiling | 40,000 Ft |
| Cruise Velocity | Mach 0.7 |
| Maximum Velocity | Mach 0.8 |
| Ground Operation Time (Start-up / Taxi) | 20 Minutes |
| UCAV Inlet Data | |
| Cruise Mass Flow | 111.5 lb/s |
| Cross Sectional Area (@ Separation Point) | 0.2266 $m^2$ |

Table 4-1. UCAV Performance Parameters.

### *4.1 Sensor Design Life*

A sensor design life of 500 flight hours was selected as a compromise between robustness and performance. Also, 500 hours is a typical scheduled maintenance interval for aircraft engines, which will facilitate sensor replacement. Assuming the radius for a typical UCAV mission is 80% of its maximum range listed in Table 2-1, 500 flight hours corresponds to roughly 126 sorties.

### *4.2 Environmental Requirements*

Department of Defense Handbook 310 (MIL-HBK-310), Global Climatic Data for Developing Military Products [9], lists the possible environmental hazards that should be considered in the design of any military device as: extreme temperature, blowing sand and dust, precipitation, humidity, ice accretion, thermal shock, and ozone concentration.

Within the UCAV's mission profile, only extreme temperature, thermal shock, and blowing sand are relevant to the performance of the hot film sensors.

### *4.2.1 Temperature Range Requirement*

In order to determine the required operating temperature range for the sensor, the one percent minimum and maximum temperature values for altitudes from sea level to 46,000 feet were considered. The one percent temperature is the value typically used in defining requirements for military hardware, and is defined as the temperature value equaled or exceeded only one percent of the time. From sea level to 46,000 feet, the one percent temperature range is 49°C to –77°C [9]. Note that since the UCAV's maximum speed is subsonic, an analysis of the free stream stagnation temperatures throughout its mission profile determined that aerothermal heating of the inlet is not a significant factor, and will not generate temperatures outside of the range given above.

However, during operation, the temperature of the sensor is increased above the ambient air temperature to achieve the desired overheat ratio. During the small-scale MIT inlet experiments described in Section 1.2, the hot film sensors produced useable results operating at a maximum overheat temperature of approximately 130°C above ambient. Allowing for a maximum overheat of 150°C, the robust hot film sensors must be designed for a worst case temperature range of –77°C to 199°C, which covers all conditions, whether the sensor is on or off. It is important to note that the overheat of the sensor must be at least 100°C to ensure that the sensor is always above the Debye Temperature (discussed previously in Section 1.3). If the temperature is allowed to fluctuate above and below the Debye Temperature, the nature of the relationship between temperature and resistivity for the sensor may change, and the sensor output will not always be consistent.

### *4.2.2 Thermal Shock Requirement*

In order for the sensors to survive startup and shutdown and to provide consistent results over a long period of time, they must be able to withstand a repetitive thermal shock equal to the maximum sensor overheat of 150°C throughout the 49°C to –77°C ambient air temperature range without a structural failure or a significant change in cold

resistance (resistance at 20°C). It is important to note that in order to obtain the most consistent data possible from a hot film sensor, its overheat must be automatically adjusted so that the temperature of the sensor relative to ambient is constant. Thus, the largest thermal shock encountered by the sensor will be the maximum overheat temperature (150°C).

### *4.2.3 Sand Abrasion Requirement*

Exposure to blowing sand is the most significant environmental hazard due to the extreme vulnerability of hot film sensors to abrasion damage. Typical commercial hot film sensors, even those with quartz protective coatings (less than 0.5 micrometer thickness), are extremely fragile due to the small size of the sensor element (typically less than 200 micrometers in the streamwise direction and less than one micrometer in thickness). In the UCAV's mission profile, exposure to blowing sand is limited to ground operation, taxi, takeoff, and landing. However, the sand abrasion is only a significant hazard when the engine is operating at power levels comparable to cruise power, which limits the time to consider to takeoff and landing. To establish that the sensors are indeed robust with respect to sand abrasion, they must not fail or experience a significant change in cold resistance (resistance at 20°C) due to sand abrasion at the maximum sand concentration and the maximum particle impact velocities possible under actual operational conditions.

Sand abrasion resistance is covered by MIL-HBK-310 [9] and by Department of Defense Test Method Standard 810F (MIL-STD-810F) [7], which divide abrasion resistance in three categories. The first class is for items likely to be in close proximity to aircraft operating over unpaved surfaces in multidirectional strong winds. This class is primarily for equipment that will be operated in the vicinity of helicopter downwash. The second class is for items never in close proximity to operating aircraft but near operating surface vehicles on unimproved surfaces. The third class is for equipment that will only see natural conditions. Since the UAV will operate from improved surfaces, it falls into the third classification for a worst case analysis. This classification requires abrasion resistance against a concentration of 0.177-0.0/+0.2 grams of sand per cubic meter of ambient air. Making the conservative assumption of standard sea level air

density (1.225 kg/m$^3$), the mass ratio of sand to air in the ambient air is $1.45 \times 10^{-4}$ to $3.08 \times 10^{-4}$. Making the assumption that the UCAV draws a mass flow equal to its cruise mass flow during its exposure to blowing sand during takeoff and landing, the mass flow rate of sand through the inlet is 0.00731 kg/s to 0.0156 kg/s. Using the cross-sectional area of the inlet near the separation point where the sensors will be located, and assuming a uniform sand distribution normal to the flow, the mass flow rate of sand per unit area in the vicinity of the sensors will be 0.0323 kg/sm$^2$ to 0.0687 kg/sm$^2$.

MIL-HBK-310 and MIL-STD-810F also provide specifications for typical airborne sand particles. Typical sand particles range from 74 to 1000 micrometers in diameter, with the majority of the particles in the 150-850 micrometer range and the mean particle size in the 150-600 micrometer range. Sand particles are composed of 95% quartz by weight with a hardness of 7 on the Moh scale and are angular in shape with sharp edges.

The maximum possible sand particle velocities were determined by approximating the particles as individual quartz spheres of diameters ranging from 74-1000 micrometers and computing the acceleration of those spheres due to drag at discrete points along a straight line path from the inlet entrance to the separation point of the flow (since the sensors will be located in the vicinity of the separation point). Note that this path is free of any collisions with the inlet walls. Standard sea level air density as well as the worst case ambient temperature and wind speed of 49°C and 18 meters per second respectively (from MIL-STD-810F [7]) were used as the initial conditions at the entrance to the inlet. The velocity of the air flow along the particle path inside the inlet was estimated from the interior Mach number profile of the inlet at the static condition at cruise power. This Mach number profile was derived from the CFD results developed by John Magnus of Northrup-Grumman for the inlet [4]. The maximum possible particle velocities are shown in Figure 4-1.

The sand concentration and particle velocity requirements given here are intended as worst case values in order to establish criteria which will ensure sensor robustness independent of the specific inlet geometry and sensor location. The actual particle sizes, velocities, and concentration seen by hot film sensors in a given inlet will clearly vary greatly based on the inlet geometry and the sensor locations.

Of course, exposure duration and contact angle requirements must also be defined. Over the design life of the sensor, the UCAV will conduct approximately 126 sorties. Assuming a combined time of one minute for takeoff and landing where the UCAV will be in close proximity to the ground at high power, and further assuming that only 15% of sorties involve a significant amount of blowing sand, then the sensor must sustain at least 19 minutes of continuous exposure to sand without a change in its cold resistance. In order to determine a requirement for the contact angle (the angle between the sand moving inside the inlet and the sensor face), the location of the sensors must be considered. Regardless of the geometry of the inlet, the sensors will be placed in areas with the potential for severely separated flow, which implies that the sensors will only be placed on surfaces which diverge from the core flow of the inlet. Thus the worst case for the contact angle is zero degrees, i.e. the sand flow is parallel to the surface of the sensor.

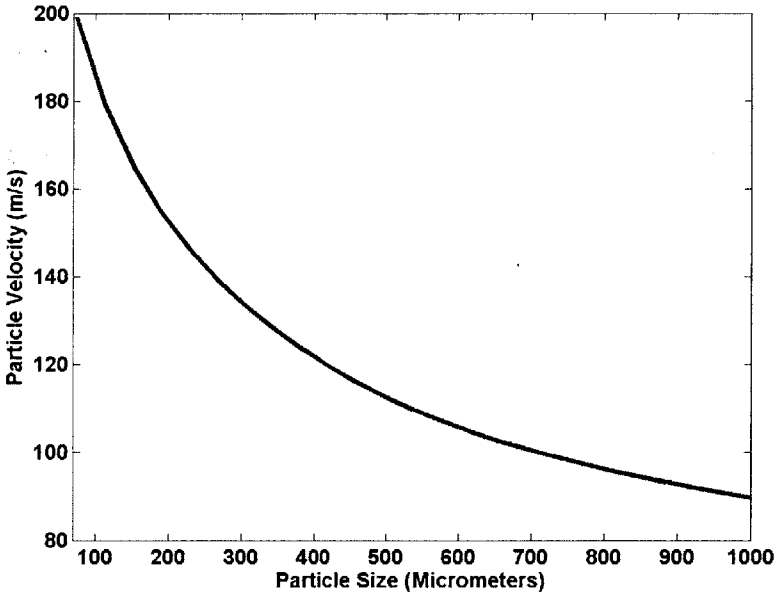


Figure 4-1. Maximum Sand Particle Velocities.

### *4.3 Performance Requirements*

There are three performance parameters of importance for hot film sensors: frequency response, sensitivity, and the stability of the cold resistance and TCR of the sensor element.

### *4.3.1 Frequency Response*

In order for the robust hot film sensors to be effective, they must have sufficient frequency response to see the characteristic frequencies in full-scale inlets. The characteristic frequency in the small-scale inlet is shown for a range of massflows in Figure 3-5.

The physical cause of this characteristic frequency has not been clearly determined, although Warfield's conclusion, which is further supported by the small-scale experimental results in Chapter 3, is that the frequency was caused by periodic vortex shedding from the separated region of the flow. Assuming that the frequency was the result of vortex shedding, the frequency of the separation in the full-scale inlet is expected to be lower than in the small-scale inlet. This prediction is based on the assumption that the flow acts qualitatively similar to two-dimensional flow over a backward facing step. For flow over a backward facing step, the vortex shedding frequency scales directly with the free stream velocity and inversely with the diffusion length (the length of the separation bubble) [19]. In two-dimensional flow, the diffusion length is directly proportional to the step height and inversely proportional to the free stream velocity [19]. Therefore, in a full-scale inlet where the velocities are comparable to the small-scale inlet but all of the physical dimensions, and thus the step height, are a factor of 6.25 larger, the vortex shedding frequency will decrease.

However, the actual frequency in the full-scale inlet can not be accurately predicted beyond the assertion that the frequency will not be larger in the full-scale inlet than in the small-scale inlet. Therefore, the design -3dB cutoff frequency for the robust hot film sensors was selected as 1000 Hz, above the highest frequency observed in the small-scale inlet, which was approximately 875 Hz.

For the sensor phase response, Warfield's work [22] suggests that in order for the sensors to be useful as inputs to an active control system, the maximum sensor phase lag should be limited to 20 degrees.

### *4.3.2 Sensitivity Requirement*

Hot film sensor sensitivity is a measure of the change in power dissipated at the sensor due to a change in the shear stress at the sensor and is typically expressed in terms

of the relevant dimensionless parameters: the Nusselt number and the Peclet number. However, since very little information was known about the shear stress profile and the perturbations in the inlet under the range of operating conditions, it was not feasible to establish a design requirement based upon the minimum shear stress that will be seen by the sensor. Instead, the sensitivity of the robust hot film sensors was evaluated under laminar steady flow conditions against the sensitivity of the commercial hot film sensors used in the small-scale inlet experiments described in Chapters 2 and 3.

### *4.3.3 Stability of the TCR Requirement*

The time stability of the TCR and the resistance of the sensor element are of critical importance to maintaining consistent sensor performance. One drawback to the use of thin metal films is that their resistance is not typically time-stable. The resistance of thin films tend to decrease slowly from the initial value at the time of fabrication to a limiting value as the films age. Since the cold resistance and the TCR must be used to set and maintain the correct overheat temperature to ensure consistent results, any significant change in either parameter over the life of the sensor will result in an incorrect setting of the overheat temperature and a change in the sensitivity of the sensor.

Since testing the sensors in real time over the design life was not feasible, aging the sensors was simulated by thermal cycling. Since the useful life of the sensor corresponds to roughly 126 sorties, in order to ensure the stability of both the TCR and the cold resistance, neither value should experience a significant change over 126 cycles, where each cycle corresponds to electrical heating of the test sensor to the maximum required temperature (200°C).

### *4.4 Summary of Requirements*

Listed below in Table 4-2 is a summary of the sensor requirements developed previously.

| Sensor Design Life | |
|---|---|
| Time | 500 Flight Hours |
| UCAV Sorties | 126 Sorties |
| **Environmental Requirements** | |
| Temperature Range | 199°C to -77°C |
| Thermal Shock | 150°C |
| **Sand Abrasion** | |
| Particle Type | 95% $SiO_2$, Moh Hardness 7, Angular Shape |
| Mean Particle Size | 150μm -600μm |
| Max Particle Velocity | Refer to Figure 4-1 |
| Particle Concentration | 0.0323 - 0.0687 $kg/sm^2$ |
| Exposure Duration | 19 Minutes with flow parallel to sensor |
| **Performance Requirements** | |
| 3dB Cutoff Frequency | 1000 Hz |
| Phase Lag | < 20° |
| Sensitivity | Comparison with commercial sensors from MIT small-scale experiments |
| TCR/Cold Resistance Stability | No significant change over sensor lifespan (126 cycles) |

Table 4-2. Summary of Robust Sensor Requirements

# 5 Robust Sensor Design

The exact performance of a hot film sensor (the power dissipated in the sensor) in turbulent flow, particularly for flows with high frequency oscillations, can not be determined a priori due to the extreme complexity of solving the three dimensional unsteady heat transfer problem involving the sensor element, the substrate, and the three dimensional surface flow with thermal and viscous boundary layers which governs the sensor performance. Although some work has been done to develop procedures to predict probe performance in laminar steady flow conditions (Kalumuck [12]) and in turbulent flows with oscillating components (Cole and Beck [3] and Menendez and Ramaprian [16]), no comprehensive method exists for the prediction of probe performance and therefore the design of sensors intended for use in turbulent flow with high frequency oscillations. The design methodology used here was therefore to examine and optimize the relevant dimensionless parameters that govern sensor performance. The diagram of the basic hot film sensor problem for a sensor element with a protective coating is shown in Figure 5-1 below.

The first step in the dimensional analysis of the sensor performance is to recognize the 19 relevant independent physical scales which describe the steady and unsteady performance of the sensor as shown in Figure 3-1. Neglecting free convection and radiation effects, the physical scales of the problem are: P, $\partial u/\partial y|_{y=0}$, h, $U_o$, $\varepsilon$, $\omega$, $\Delta T$, $\alpha_s$, $\alpha_f$, $\alpha_c$, $\alpha_e$, $k_s$, $k_f$, $k_c$, $l_e$, $w_e$, $t_e$, $t_c$, $t_s$. Note that $t_s$ is not the actual depth of the substrate, but the depth of the substrate which is involved in the transient heat transfer. These scales have 4 independent units (mass, length, time and temperature). Therefore, the dimensionless power dissipated in the sensor (Nu) is a function of 14 independent dimensionless parameters: the Peclet Number (Pe); the substrate/fluid thermal conductivity ratio (K); the coating/substrate thermal conductivity ratio ($K_c$), the sensor aspect ratio (AR); the frequency for the substrate, the element, and the coating ($F_s$, $F_e$, $F_c$); the coating Biot number (Bi); the flow oscillation amplitude ($\varepsilon$); the effective length of the sensor (L*); the ratios of the thermal diffusivities of the substrate, the element, and the coating to the fluid thermal diffusivity ($\alpha_s$*, $\alpha_e$*, $\alpha_c$*), and the sensor element length to thickness ratio (t*). Thus:

$Nu = f(Pe, K, K_c, AR, F_s, F_e, F_c, Bi, \varepsilon, L^*, \alpha_s^*, \alpha_e^*, \alpha_c^*, t^*)$.

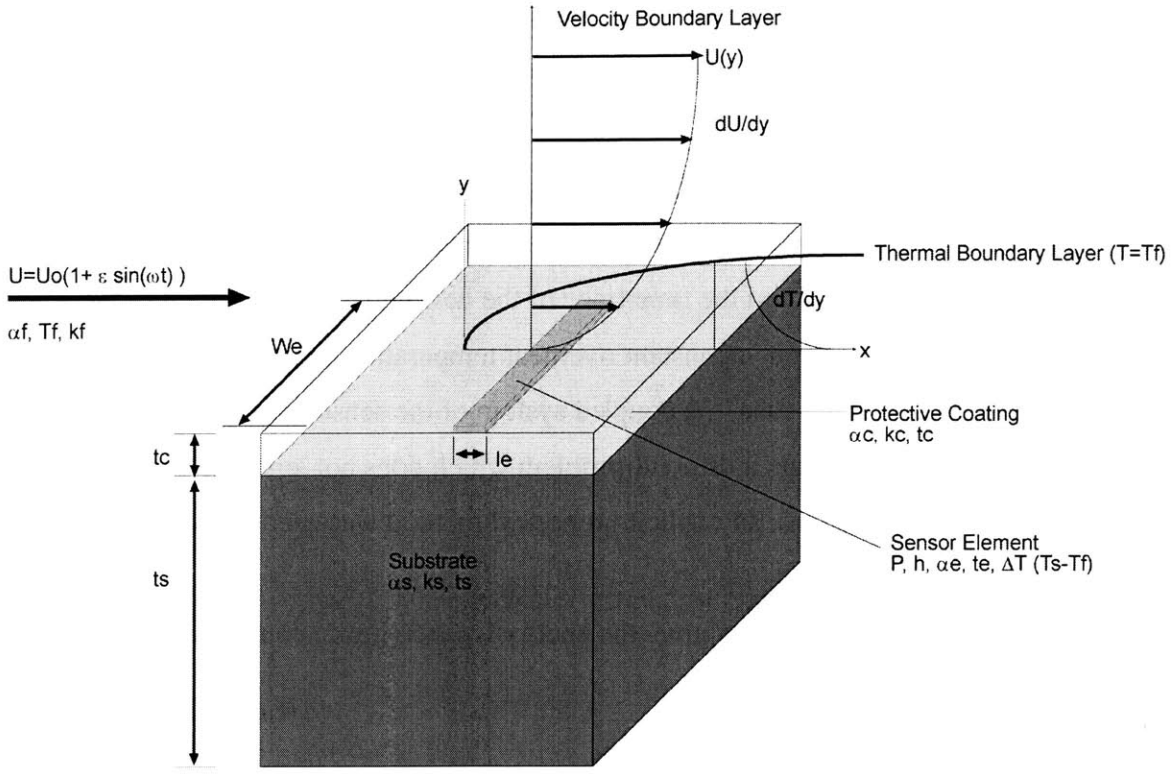


Figure 5-1. Hot Film Sensor Problem Diagram.

Note the Reynolds Number and the Prandtl Number, two parameters typical of this type of problem, are not included since the velocity gradient at the wall ($\partial u/\partial y|_{y=0}$) and the convection heat transfer coefficient at the sensor surface (h) were chosen as the physical scales to describe the velocity and the thermal boundary layer effects in place of the fluid kinematic viscosity.

Examination of the effects of these dimensionless parameters as well as other concerns, to include the ease of fabrication and the commercial availability of materials, led to the final design selected for the robust sensors. The final sensor design was a configuration using a 2000 Angstrom thick, high aspect ratio nickel sensor element with gold leads on a quartz substrate with a 2 micrometer thick protective coating of Aluminum Oxide.

### *5.1 One Dimensional Sensor Model*

In order to determine the effects of the material properties and the dimensions of the sensor element, the substrate, and the protective coating on the overall dynamic response of the sensor, the sensor was simulated using a simplified one-dimensional model. Once the physical dimensions and material properties of the sensor system were set, the model took a time varying convection heat transfer coefficient (h) for the sensor surface as the input and returned the time trace of the heat generation required in the sensor to maintain the sensor at a constant overheat temperature as the output. However, even in the one-dimensional case, the coupled system of the sensor element, substrate, and protective coating presents a difficult problem which does not lend itself to an analytical solution. Therefore, an explicit numerical method was used to model the system.

Considering any control volume, the energy balance inside can be written as:

$$\frac{\partial}{\partial x}(k\frac{\partial T}{\partial x})+\dot{Q}=\rho C_P\frac{\partial T}{\partial t}. \qquad \text{(Equation 5.1)}$$

Due to the changes in material properties in the system, simple finite difference methods were not used to discretize this equation. Instead, a discrete representation using the equivalent thermal capacitance at each node and the equivalent thermal resistance between nodes was used. The discrete energy balance for a given node is as shown below:

$$\sum_{n=2}^{3}\frac{(T_1^i-T_n^i)}{R_{1n}}+\dot{q}'\Delta x=C_1(\frac{T_1^{i+1}-T_1^i}{\Delta t}), \qquad \text{(Equation 5.2)}$$

where $R_{1n}$ is the equivalent thermal resistance between node 1 and node n and $C_1$ is the equivalent thermal capacitance of node 1, defined as $C_1\equiv\rho_1 C_{P1} V_1$ where $V_1$ is the volume of node 1 [17]. Note that the superscripts indicate increments in time. A diagram of this node discretization is shown below in Figure 5-2. For an interior node as shown in Figure 5-2, the explicit expression for $T_1^{i+1}$ is:

$$T_1^{i+1}=T_i(1-\frac{\Delta t}{C_1R_{12}}-\frac{\Delta t}{C_1R_{13}})+T_2^i(\frac{\Delta t}{C_1R_{12}})+T_3^i(\frac{\Delta t}{C_1R_{13}})+\frac{\dot{q}'\Delta x\Delta t}{C_1}. \qquad \text{(Equation 5.3)}$$

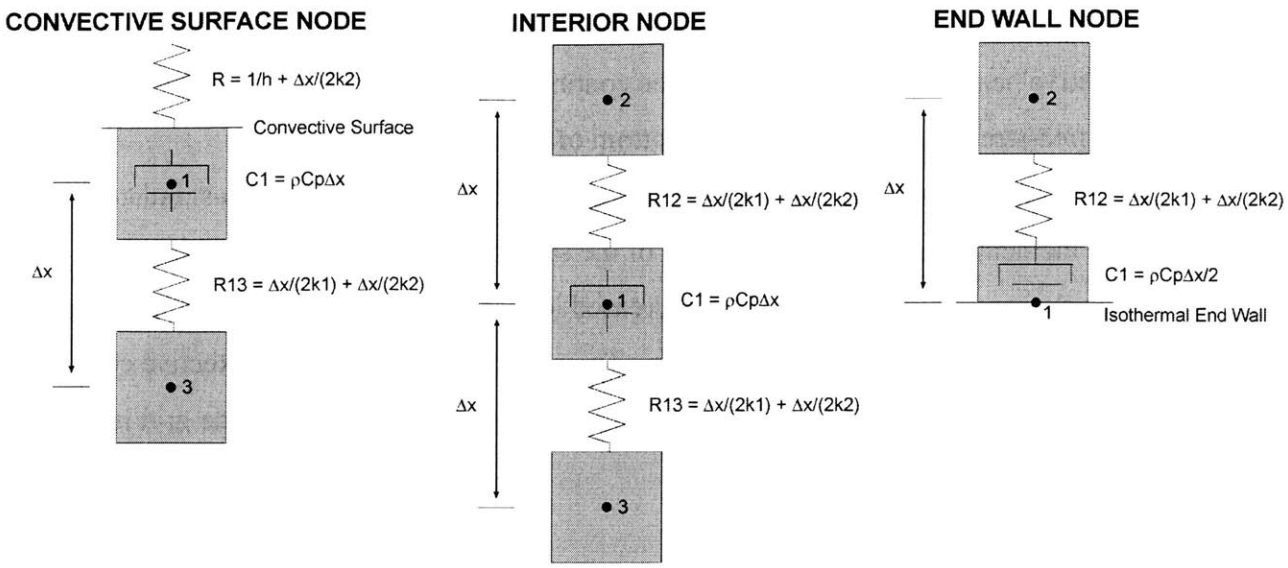


Figure 5-2. Resistance-Capacitance Node Discretization.

For simplicity, the following assumptions were incorporated into the model:

1. Only forced convection effects were considered at the surface. Free convection effects are only significant when $Gr_L / Re_L^2 >> 1$, where $Gr_L$ is the Grashof number. The Grashof number is a ratio of the buoyancy force to the viscous force acting on the fluid, and for a perfect gas is defined as:

   $Gr_L \equiv \frac{g(\Delta T) l_e^3}{T_f \nu^2}$ where ν is the fluid kinematic viscosity. Due to the high velocity of the inlet flow and the extremely small length scale for the heat transfer from the sensor to the fluid, $Gr_L / Re_L^2 << 1$ and the effects of free convection could be neglected.
2. The substrate, coating and sensor element had perfect thermal contact (zero thermal resistance due to the material interface).
3. The substrate, coating and sensor element had perfectly uniform material properties.
4. The sensor responded instantaneously to temperature changes in the substrate and the coating (the time delay due to the constant temperature anemometer circuit was neglected).

For boundary conditions, the model used forced convection with a time variant convective heat transfer coefficient at the coating surface and an isothermal boundary (set to the free-stream temperature) at the bottom of the substrate.

The discrete node grid uses a single node 0.1 micrometers wide to simulate the sensor element. The first five elements of the substrate are of the same width as the sensor element and then the width is increased logarithmically to reduce the number of required elements to model the substrate. The element spacing in the protective coating was set at the same spacing as the sensor element. An example of the node grid is shown in Figure 5-3.

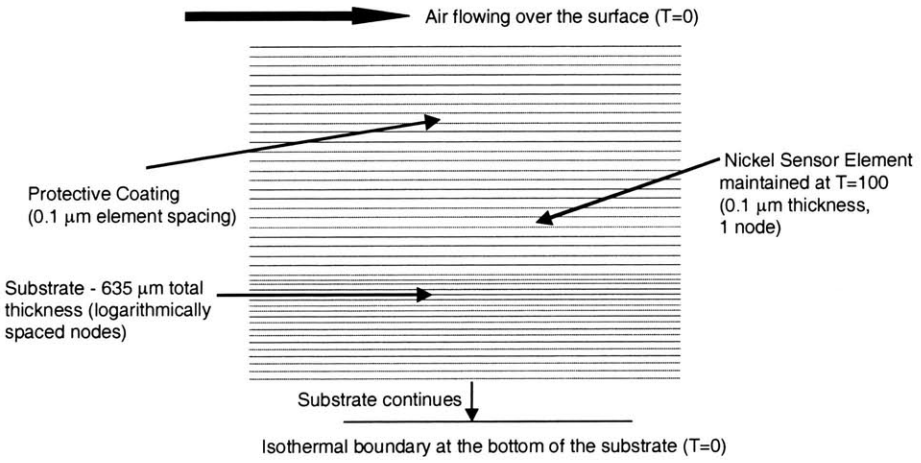


Figure 5-3. One-Dimensional Sensor Model Node Grid.

The model validity was verified by establishing the boundary conditions and allowing the model to converge to a steady state solution. The model value for the steady state heat generated in the sensor converged to within 0.05% of the exact steady state value for the entire range of materials and conditions examined. Note that convergence to less than 0.05% was possible but was not performed due to the computational expense.

### *5.2 Substrate*

The performance of the sensor depends significantly on the substrate material and dimensions. The key parameters which describe the substrate contribution to sensor

performance are the substrate/fluid thermal conductivity ratio (K) and the dimensionless frequency based on the substrate ($F_s$). The value of K affects the steady performance of the sensor while the value of $F_s$ affects its dynamic response. Table 5-1 below lists several of the candidate substrate materials which are commercially available and commonly used in thin film applications.

| Candidate Substrate Material Properties | | | | | |
|---|---|---|---|---|---|
| Substrate | k (W/mK) | $K^{-1}$ ($k_f/k_s$) | Thermal Diffusivity $\alpha x10^6$ ($m^2/s$) | Thermal Shock Resistance (°C) | Max Temp (K) |
| Kapton* | 0.12 | 0.219 | 0.0775 | NA | 673 |
| Acrylic PMMA (Plexiglas©) | 0.26 | 0.101 | 0.127 | Information Not Available | 366 |
| Pyrex** | 1.4 | 0.0188 | 0.7535 | 100 | 763 |
| Quartz | 1.4 | 0.0188 | 0.850 | 1400 | 1883 |
| MACOR | 1.8 | 0.0146 | 0.898 | 25-100 | 1273 |
| Alumina*** | 36 | 0.000731 | 7.94 | 200 | 2323 |

Table 5-1. Properties of Candidate Substrate Materials.

*©Dupont Corporation
**©Corning
*** 99.6% Tape Cast $Al_2O_3$

The conductivity ratio (K) describes the relative contributions of heat conduction into the substrate and forced convection into the fluid to the total power dissipated in the sensor. Natural convection and radiation also contribute to the total power dissipated, but are negligible when compared to conduction and forced convection ($Gr_L / Re_L^2 << 1$ ). Since the substrate material typically has a thermal conductivity much larger than that of the air ($K >> 1$), conduction to the substrate is usually the dominant mode of power dissipation in the sensor. The steady-state effect of conduction to the substrate is to influence the zero-flow power, which is sometimes referred to as the background measurement or the dc bias to the sensor output signal. As noted by Kalumuck [12], the value of K has a minor effect on the sensitivity of the sensor to changes in surface shear stress, but is significant in that it provides a first order approximation of the percentage of the power applied to the sensor that is actually convected to the fluid and therefore is "flow sensitive." Consider the sensor as a one-dimensional heat transfer problem with a substrate of depth $t_s$. With no protective coating, the ratio of the heat convected to the

fluid versus the heat conducted into the substrate in steady-state is simply $(\frac{k_f}{k_s})(t_s)(\frac{\partial T}{\partial y}|_{y=0})^{-1}$ where $t_s(\frac{\partial T}{\partial y}|_{y=0})^{-1}$ is a fixed value for a given flow condition and geometry. The inverse of the conductivity ratio K ($K \equiv \frac{k_s}{k_f}$) therefore provides an estimate of the ratio of flow sensitive power to the power lost to the substrate. Construction of a sensor with a very high K value results in a very large power required to maintain a desired sensor overheat temperature and a very low flow sensitive percentage of the total power. A large K value can also make it impossible to reach a desired overheat temperature without first exceeding the maximum electrical current the sensor element can withstand. Therefore, a low K value and hence a low substrate thermal conductivity is advantageous in terms of the sensor efficiency.

In an unsteady flow, the substrate plays an important role in the dynamic response of the sensor. Cole and Beck note that although the anemometer maintains the average sensor temperature as constant, the actual temperature distribution on the film varies slightly for different flow conditions. Also, as changes in the flow cause changes in the thermal boundary layer, the substrate does not instantaneously adjust to the new equilibrium upstream and downstream of the sensor element. Thus, as the flow over the sensor changes, the probe signal lags the flow because the substrate cannot adjust instantaneously to the new thermal equilibrium [3]. The parameter which describes the effect the substrate has on the sensor's unsteady performance is $F_s$, defined as: $F_s \equiv \frac{\omega t_s^2}{\alpha_s}$. The parameter $F_s$ is a ratio of the characteristic thermal time for the substrate to the period of the flow oscillations. Another way to look at $F_s$ is as the inverse of the Fourier number (dimensionless time) based on the oscillation period. As $F_s$ increases, the phase lag of the sensor should also increase. In determining how to minimize $F_s$, it is important to note that the exact relationship between the thermal penetration depth $t_s$ and $\alpha_s$ has not been determined. The work of Menendez and Ramaprian does not include the dynamic effects of the substrate in the sensor model, while the work of Cole and Beck establishes the value of $t_s$ for the model using empirical correlations. Thus, the exact effect of the value of $\alpha_s$ as a design parameter is not known. But, Kalumuck's work suggests that a

high value of $\alpha_s$ is advantageous for dynamic response. Since $\alpha_s=k_s/(\rho_s C_P)$, increasing $\alpha_s$ typically means increasing $k_s$ and therefore K, resulting in a higher dc bias and a lower percentage of flow sensitive power. Therefore, the choice of the substrate material must balance the need for a low K for high efficiency with the need for a high $\alpha_s$ for good dynamic response.

Despite the performance issues discussed above, there are several other important considerations in the design of the substrate. The substrate must be an electrical insulator. The substrate must have a high thermal shock resistance to withstand the rapid heating and cooling of the sensor element as well as the wide temperature range encountered over the vehicle's flight profile and a high maximum temperature (above 300°C) to withstand the temperatures used in the fabrication process. The substrate material must also not degrade the time stability of the TCR for the sensor element. Finally, the substrate must be commercially available with a high quality surface finish.

Quartz was selected as the substrate material for the robust sensors as a compromise between low K and high $\alpha_s$. Also, quartz has excellent thermal shock and high temperature performance as well as good TCR stability for metal films and is readily available commercially. The substrate thickness was set at 635 micrometers (0.025") for cost and ease of fabrication since thinner substrates must be custom made and are difficult to handle during the sensor fabrication process.

### *5.3 Sensor Element*

The design of the sensor element requires an examination of the dimensionless parameters Pe, AR, L* and $F_e$ as well as the sensor resistance R and the sensor Temperature Coefficient of Resistivity ($\Theta$).

The Peclet Number (Pe) is defined as: $Pe \equiv \frac{sl_e^2}{\alpha_f}$ and is a dimensionless expression of the surface shear stress. As Kalumuck points out, it is advantageous to operate at the highest possible Peclet number in order to maximize the sensor sensitivity to shear stress and to increase the amount of flow-sensitive power dissipated in the sensor.

The dimensionless probe length $L^*$ is defined as $L^* \equiv \frac{\omega l_e}{U_o}$ and provides a ratio of the probe stream-wise length to the wavelength of the flow oscillations of interest. As $L^*$ approaches unity, the sensor will be unable to resolve the flow oscillations since they will take place over a length of the same order as the sensor length. Since the effective stream-wise length of the probe is usually longer than the actual length of the sensor due to heat conduction in the substrate, the convection of heat downstream from the sensor and the diffusion of heat through the protective coating, and since the actual velocity inside the thermal boundary layer is significantly less that the free stream velocity used in the non-dimensionalization, $L^* << 1$ for effective spatial resolution of the desired flow oscillations.

The sensor aspect ratio is defined as $AR \equiv \frac{w_e}{l_e}$ and is important in terms of the sensor's steady state performance. Kalumuck's work [12] indicates that as the sensor aspect ratio increases, the sensor's steady-state sensitivity to shear increases and its zero-flow power decreases.

The dimensionless frequency $F_e$ is defined as $F_e = \frac{\omega t_e^2}{\alpha_e}$ and is a ratio of the thermal characteristic time of the sensor element to the period of the flow oscillations. Clearly, in order to have an adequate dynamic response, the sensor element must have a characteristic time which is less than the oscillation period ($F_e << 1$). As $F_e$ increases past unity, the sensor amplitude response will decrease and the phase lag will increase.

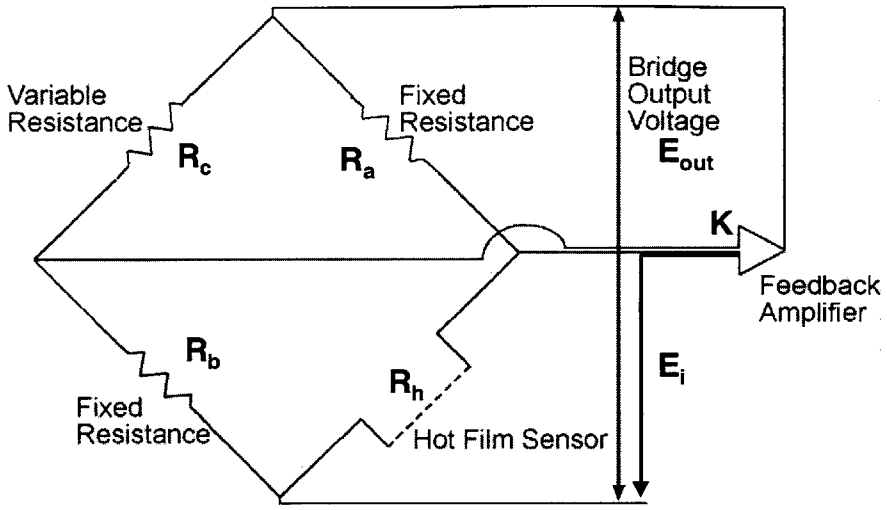


Figure 5-4. Constant Temperature Anemometer Bridge.

The Temperature Coefficient of Resistivity (TCR) affects the sensitivity of the sensor to changes in surface shear stress. Figure 5-4 shows the sensor as part of a simplified constant temperature anemometer (CTA) bridge. The effect of TCR is clear from an examination of an instantaneous change in the heat transfer rate at the sensor ($\delta\dot{Q}$) due to a change in the flow conditions over a time increment $\delta t$. The change in the resistance of the sensor ($\delta R_h$) is given by the relation:

$$\delta R_h = \frac{R\Theta(\delta\dot{Q})(\delta t)}{\rho_e C_P V_e} \qquad \text{(Equation 5.4)}$$

where $V_e$ is the volume of the sensor element, $\rho_e$ is the sensor element density (not the resistivity), and $C_P$ is the sensor element specific heat. The quantity $\rho_e C_P$ is the volumetric thermal capacitance of the sensor element. The corresponding instantaneous change in the output voltage is then:

$$\frac{\delta E_{out}}{E_{out}} = \frac{-\kappa(\delta R_h)}{(R_a + R_h)(R_a + R_h + \delta R_h)} \qquad \text{(Equation 5.5)}$$

where $E_{out}$ is the CTA output voltage and $\kappa$ is the constant gain for the feedback amplifier. From Equations 5.4 and 5.5 it is evident that the change in the output voltage can be maximized by maximizing the value of the sensor element TCR.

The resistance of the sensor element (R) is significant because the sensor is a resistive heater operated at extremely high power densities (typically in excess of 1 $MW/m^2$). For a fixed maximum bridge voltage, these high power densities require low sensor resistance values. Typical constant temperature anemometers work off a maximum bridge voltage of 8-16 Volts, and are limited to probes with a maximum resistance (at overheat temperature) of 30 Ω. Therefore, a lower sensor resistance allows a higher maximum overheat temperature, which is desirable since a high overheat temperature improves the sensor's sensitivity, its frequency response and reduces the effect of freestream temperature variations. However, too low a resistance value can present problems as well. Equation 5.4 and 5.5 indicate that a lower R value results in a lower change in the CTA output voltage due to a change in the flow. Also, since very low resistances are difficult to measure accurately, sensor elements with low resistances can introduce significant errors in balancing the anemometer bridge and setting the overheat value. Commercially available hot film sensors typically have cold resistance values in the range of 6-15 Ω.

The considerations above lend insight into the selection of the sensor element dimensions and material. Consider first the sensor element thickness. Optimum performance requires minimizing $F_e$, which translates to minimizing the sensor thickness. However, since R is inversely proportional to $t_e$ as shown by the relation:

$$R = \frac{\rho(AR)}{t_e}, \qquad \text{(Equation 5.6)}$$

the thickness can not be reduced beyond the point where R is no longer in the useable range. Previous experiments on evaporated Nickel coatings indicated that 2000 Angstroms is the thinnest coating which can be applied by evaporation and still guarantee complete surface coverage. At a thickness of 2000 Angstroms, sensors of useable resistance can be fabricated from a number of metals. Thus, the element thickness was set at 2000 Angstroms.

The sensor design width was set based on the competing requirements of a high aspect ratio (large $w_e$) and a small overall sensor size (small $w_e$). The design goal for the overall size of the sensor head was $^1/_{16}$ of an inch in diameter. Reducing the width of the sensor also reduces its directional sensitivity and the amount of spatial averaging of the

surface flow conditions. Thus, the sensor width was set at value of 1016 micrometers (0.040 inches), which is comparable to the widths of commonly used commercial sensors.

The sensor design stream-wise length was determined by considering Pe, L*, AR, R and the limits of the fabrication process. The optimum stream-wise length balances the need for a high Pe value and a low value of R (high $l_e$) with the need for adequate spatial resolution and a high AR (low $l_e$). The minimum feature size for the fabrication technique used to create the photolithography mask for the sensors was 25 micrometers. Three design values of the stream-wise length were selected in order to compare their relative performance and to ensure that the fabricated sensors were within the useable resistance range. The three values of $l_e$ were: 81.3 micrometers (0.0032"), 67.5 micrometers (0.0025") and 50.8 micrometers (0.0020"), corresponding to aspect ratios of 12.5, 16 and 20 respectively.

The sensor element material was selected based on the requirements for low values of R and $F_e$ and a high value of TCR. Since the optimum performance requires a high aspect ratio, a low thickness and a low overall resistance, Equation 5.6 indicates that the material selected must have a low volume resistivity. For the design, the acceptable range for resistance was set as 5-15 Ω. However, thin films tend to have higher volume resistivities than they would in bulk due to the sub-micron thickness as well as impurities and possibly discontinuities in the film. Bulk properties are used for the design because the material properties for metals applied in thin films at sub-micron thicknesses are not well documented and depend significantly on the quality of the deposited film (level of impurity, etc.). Fabrication results presented in the next chapter for Nickel indicate that the actual resistivity achieved was approximately 144% of the bulk resistivity value. Thus, increasing the bulk resistivities by a factor of 1.5 and considering the range of aspect ratios as 12-20 with an element thickness of 0.2 micrometers, the sensor material must have a bulk volume resistivity in the range of 5.8-10 μΩcm. Furthermore, the material must have a high TCR for sensitivity and a high thermal diffusivity to minimize $F_e$. Equation 5.4 indicates that a low volumetric thermal capacitance is also advantageous, but since the volume of the sensor is so low, the difference in thermal

capacitance between different metals is negligible. Table 5-2 lists typical metals used for thin film resistive sensors elements and their bulk properties.

| Candidate Sensor Element Material Properties | | | | | |
|---|---|---|---|---|---|
| Metal | T(°C) | ρ (μΩcm) | TCR (x$10^3$ 1/°C) | α(x$10^6$$m^2$/s) | ρCp (x$10^{-6}$ J/$m^3$K) |
| Nickel | 20 | 6.84 | 6.9 | 23.0 | 3.95 |
| Gold | 20 | 2.24 | 8.3 | 127 | 2.49 |
| Copper | 20 | 1.68 | 6.8 | 117 | 3.44 |
| Zirconium | 20 | 40.0 | 4.4 | 12.4 | 1.82 |
| Iron | 20 | 9.71 | 6.5 | 23.1 | 3.52 |
| Tin | 0 | 11.0 | 4.7 | 40.1 | 1.66 |
| Tantalum | 25 | 12.45 | 3.8 | 24.7 | 2.32 |
| Platinum | 20 | 10.6 | 3.9 | 25.1 | 2.85 |
| Palladium | 20 | 10.5 | 3.7 | 24.5 | 2.93 |
| Cadmium | 0 | 6.83 | 4.2 | 48.4 | 2.00 |
| Chromium | 0 | 12.9 | 3.0 | 29.1 | 3.21 |
| Zinc | 20 | 5.92 | 4.2 | 41.8 | 2.78 |
| Aluminum | 20 | 2.65 | 4.3 | 97.1 | 2.44 |

Table 5-2. Candidate Sensor Element Material Properties.
(from Guenette [10])

From Table 5-2, Nickel is the clear choice for the sensor element material due to its low resistivity within the acceptable range and its high TCR. Note that although thermal diffusivity is shown for all of the candidate materials, it is not as significant as the resistance and the TCR because the sensor thickness is so small. At a thickness of 2000 Angstroms with the maximum frequency of interest of 1000 Hz, the value of $F_e$ will be orders of magnitude less than unity regardless of the metal used.

### *5.4 Protective Coating*

The robust hot film sensor uses a protective coating to prevent damage to the sensor element from sand abrasion and due to installation and maintenance handling. Three dimensionless parameters involving the coating affect the performance of the sensor: $F_c$, Bi, and $K_c$.

For a given substrate and a coating which is at least an order of magnitude thicker than the sensor element with a comparable or lower thermal diffusivity than the sensor element, the dynamic response of the coating will govern the dynamic response characteristics for the sensor since $F_c >> F_e$. Just as for the substrate and the sensor

element, $F_c$ is simply a ratio of the flow oscillation period to the characteristic time for the coating. Clearly, optimizing the sensor dynamic performance for a given frequency range requires a coating which can achieve thermal equilibrium much faster than the period of the flow oscillations of interest ($F_c<1$). Using the one-dimensional model detailed in Section 5.1, the amplitude and phase lag of the power dissipated in the sensor due to a time varying convection heat transfer coefficient at the coating surface were determined for a range of coating thicknesses. Figures 5-8 and 5-9 show the amplitude and frequency response curves based on $F_c$ for the sensor. Note that for the results shown, the model used a 635 micrometer thick quartz substrate with a Nickel sensor element and an Aluminum Oxide coating. Coating thicknesses of 1, 2, 5, 10 and 20 micrometers were examined. For both the amplitude and the phase lag, as shown in Figures 5-8 and 5-9, all of the dimensional curves collapse into a single dimensionless curve based on $F_c$, which demonstrates how the characteristic time of the coating $t_c^2/\alpha_c$ dominates the dynamic response of the sensor. The one-dimensional model results indicate that for an amplitude response above the –3dB cutoff, the $F_c$ value for the coating must be less than 2.42. For a phase lag of less than 20 degrees, the $F_c$ parameter must be less than 0.715. Although these values are clearly rough approximations, they offer a means to estimate the maximum allowable coating thickness given the dynamic performance requirements.

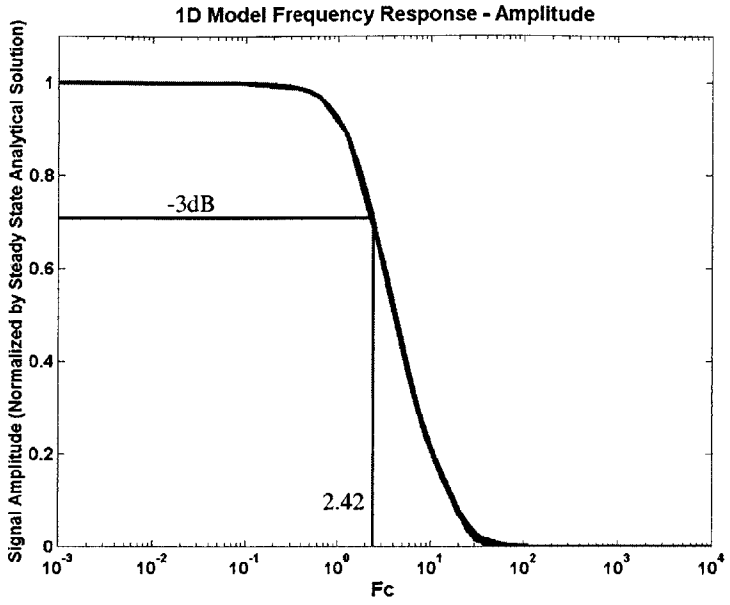


Figure 5-5. One-Dimensional Model Amplitude Response versus Coating Thickness (Non-Dimensional).

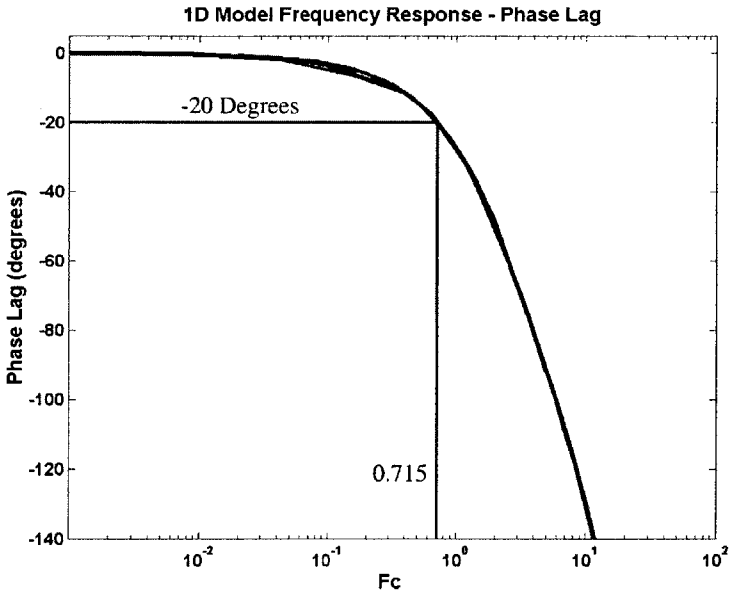


Figure 5-6. One-Dimensional Model Phase Response versus Coating Thickness (Non-Dimensional).

The Biot number is the ratio of the resistance to conduction in a material and the resistance to convection along the surface of that material. In steady-state, the Biot number is a ratio of the temperature drop across the coating to the temperature drop between the coating and the freestream. For the sensor coating, Bi<<1 is desired in order

to ensure that conduction within the coating responds more rapidly than changes in the thermal boundary layer. Optimizing the Biot number requires using the thinnest possible coating with a coating material of the highest possible thermal conductivity.

The ratio of the coating and substrate thermal conductivities ($K_c$) indicates the degree to which heat is transferred to the coating relative to the substrate in steady state. As discussed previously, the vast majority of the heat produced by the sensor is lost due to conduction in the substrate and does not contribute to the performance of the probe. As $K_c$ increases, the thermal resistance of the coating relative to the substrate decreases and the amount of heat conducted through the coating (the amount of flow sensitive power) increases relative to the amount of heat conducted through the substrate. Thus, to maximize the flow sensitive power, a material with a very high thermal conductivity relative to the substrate should be used.

The protective coating also has an effect on the steady state sensitivity and spatial resolution of the sensor which is not seen in the one-dimensional model. As the thermal conductivity of the coating decreases or the thickness of the coating increases, the heat transferred from the sensor to the surface will become more diffuse, giving the sensor a longer effective probe length at the convective surface. The effect of a longer effective probe length is to increase the sensor's aspect ratio and therefore reduce its steady state sensitivity as well as its spatial resolution.

To summarize, optimum sensor performance requires a coating which is as thin as possible to achieve the desired abrasion resistance with as high a thermal diffusivity and thermal conductivity as possible.

In order to determine the abrasion resistance for the sensor, the hardness of the candidate protective coatings must be considered. For contact angles greater than 45 degrees, where the contact angle is defined as the angle of the impact surface relative to the free stream, abrasive wear is dominated by microcracking in the surface material and therefore is best countered with a ductile material which can withstand the impact shock of the abrasive particles without cracking. On the other hand, the opposite is true for contact angles of less than 45 degrees where the dominant wear mechanism is microcutting due to abrasive particles which are harder than the surface material dragging along the surface. Thus, the best material for low contact angles is a material which is

harder than the abrasive elements. For the robust sensor design, hardness was selected over ductility since regardless of the sensor location within the inlet, the contact angle will likely be less than 45 degrees. To prevent wear damage to the sensor, the protective coating must have a Moh's hardness value greater than that of naturally occurring sand (7).

Table 5-3 is a list of the candidate materials considered for the coating and their bulk properties. Quartz is included in the table since it is commonly used on commercial sensors to prevent handling damage. The materials listed in Table 5-3 are electrical insulators commonly used as wear resistant coatings. Note that although electrochemical treatments (the application of metal coatings by electrolysis) are possible, they do not produce as high a surface hardness as some of the ceramic materials in Table 5-3 [23].

| Candidate Coating Material Properties | | | | | |
|---|---|---|---|---|---|
| Material | $\alpha$ x$10^6$ ($m^2/s$)* | k (W/mK)* | Hardness (Moh Scale) | Resistivity ($\Omega$m@RT) | Thermal Shock Resistance °C |
| SiC | 230 | 490 | 10 | $10^6$ | 350 |
| $Al_2O_3$ | 11.9 | 36 | 9 | $10^{12}$ | 200 |
| $Si_3N_4$ | 9.65 | 16 | 9 | $10^{11}$ | 750 |
| $SiO_2$ | 0.834 | 1.38 | 7 | $10^8$ | 1400 |

*Values from Incropera & Dewitt, Introduction to Heat Transfer

Table 5-3. Bulk Properties of Candidate Coating Materials.

Of the candidate materials considered, clearly Silicon Carbide is optimal, possessing an extremely high $k_c$, $\alpha_c$, and surface hardness. However, commercial application of Silicon Carbide is done only through chemical vapor deposition (CVD) which requires temperatures in excess of 1350°C and typically applies thickness on the order of 100 micrometers or more. The extreme temperatures involved in CVD are incompatible with the sensor design since they exceed the melting point of Gold (1062°C) and are near the melting point of Nickel (1455°C). Furthermore, the typical thicknesses applied are too large for the protective coating and the cost of establishing a system to apply the correct thickness is prohibitive.

Aluminum oxide is the next best material for the coating in terms of $k_c$, $\alpha_c$, and surface hardness. Also, Aluminum Oxide has a number of relatively inexpensive and commonly used commercial methods for deposition. One additional benefit of Aluminum Oxide, as indicated by Popescu [18], is that it is the optimum material for

maintaining the time stability of the TCR of the sensor element. Aluminum Oxide can be applied through physical vapor deposition (PVD) methods including evaporation and sputtering from sub-micron to hundreds of microns in thickness. Sputtering is the application method of choice since it results in a higher quality surface coating with a higher hardness and a better step coverage than evaporation.

Based on the considerations outlined above, a 2 micrometer thick Aluminum Oxide coating was selected to protect the sensor. Based on the one-dimensional model results, the maximum thickness of Aluminum Oxide which still allows the sensor to meet the stated requirements of having an amplitude reduction of less than 3dB at 1000 Hz and a phase lag of less than 20 degrees is 36.8 micrometers. The design value for the coating was selected as much less than this predicted value for several reasons. First, selecting a thinner coating will ensure adequate performance despite uncertainty in the actual thermal properties of the coating. The material properties used for the model are bulk values because the actual thermal properties for a thin film coating depend on the deposition method and the quality of the deposited film. Second, the one-dimensional model is an optimistic simplification of the problem and therefore should over-predict the allowable coating thickness. Finally, the cost for Aluminum Oxide coatings between 2 micrometers and 20 micrometers is excessive because the deposition must be done through sputtering which requires a slow deposition rate and thus an excessive amount of time to apply the coating.

### *5.5 Summary*

The physical dimensions of the sensor are summarized in Table 6-2. The design values for the key dimensionless parameters described above are listed in Table 5-4. Note that in Table 5-4, $L^*$ assumes a $U_o$ value corresponding to Mach 0.7 at 300K.

| Design Parameters (300 K) | | | |
|---|---|---|---|
| | 12.5 AR | 16 AR | 20 AR |
| Pe | $(2.94x10^{-4})(s)$ | $(2.02x10^{-4})(s)$ | $(1.15x10^{-4})(s)$ |
| K | 53.23 | | |
| $K_c$ | 25.71 | | |
| $F_e$ | $1.09x10^{-5}$ | | |
| $F_c$ | $2.10x10^{-3}$ | | |
| Bi | $(5.56x10^{-8})(h)$ | | |
| $L^*$ | $2.1x10^{-3}$ | $1.7x10^{-3}$ | $1.3x10^{-3}$ |
| $\alpha_s^*$ | 0.0371 | | |
| $\alpha_e^*$ | 1.022 | | |
| $\alpha_c^*$ | 0.529 | | |
| $t^*$ | 406.5 | 337.5 | 254.0 |
| R | 6.41 Ω | 8.21 Ω | 10.26 Ω |
| TCR | $6.9x10^{-3}$ 1/°C | | |

Table 5-4. Sensor Design Parameters.

# 6 Robust Sensor Fabrication

The robust sensors were fabricated using electron beam evaporation deposition and standard photolithography techniques as well as simple physical masking to create the Nickel sensor elements and the Gold sensor leads. The Aluminum Oxide protective coating was applied through sputter deposition. The resistance of the sensor element was stabilized using a long duration, high temperature bake.

The sensors were constructed on 1" x 1" x 0.025" quartz substrates. The physical properties of the substrates are listed below in Table 6-1.

| Substrate Physical Properties | |
|---|---|
| $SiO_2$ Purity | 100% |
| Density | 2.2 $g/cm^3$ |
| Specific Heat | 745 J/kgK |
| Thermal Conductivity | 1.4 W/mK |
| Coefficient of Thermal Expansion | $0.55x10^{-6}$ |
| Surface Polish | 60/40 Optical |
| Camber | 0.0003-0.0005 (inch/inch) |
| Hardness | 7 (Mohs Scale) |
| Compressive Strength | 161,000 psi |
| Flexural Strength | 25,000 psi |

Table 6-1. Substrate Physical Properties.
(from Accumet Engineering Corporation)

Figure 6-1 illustrates the general procedure used to fabricate the robust sensors. Steps 1-9 were completed at the MIT Technology Research Laboratory (TRL), a Class 100 clean facility. Step 10, the deposition of the Aluminum Oxide protective coating, was performed by San Diego Magnetics, Inc.

The first step in the fabrication process was to clean the substrates to ensure proper adhesion of the Nickel layer. The quartz substrates were cleaned with a succession of acetone, methanol and 2-isopropynol and then in a room temperature piranha bath (1:3 solution of hydrogen peroxide and sulfuric acid) to ensure their surfaces were completely devoid of organic and inorganic contaminants.

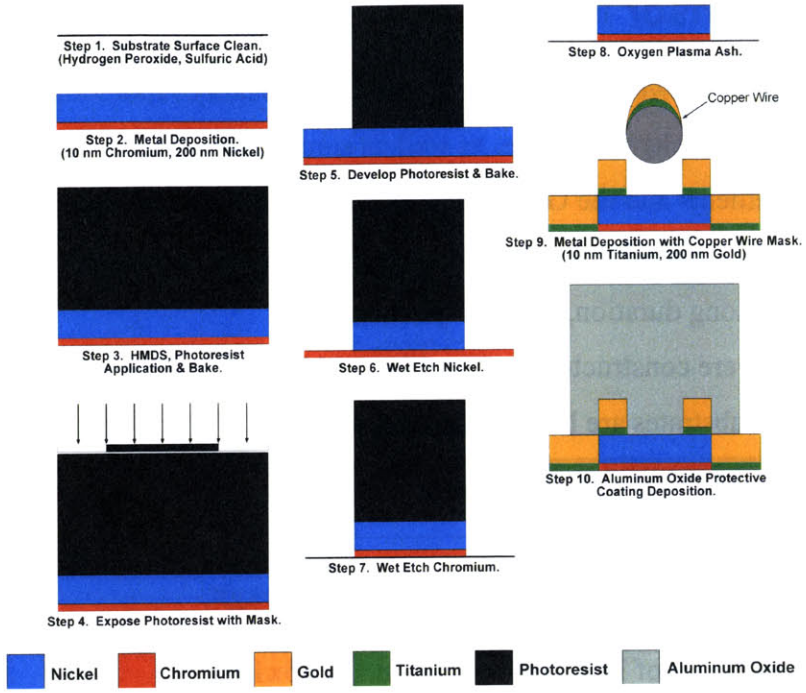


Figure 6-1. Sensor Fabrication Process.

Next, a nominally 2000 Angstrom thick Nickel layer for the sensor elements was deposited by electron beam evaporation. The thickness of the Nickel layer was set by initial deposition experiments which indicated that 2000 Angstroms was the thinnest coating which could guarantee continuous surface coverage. Also, initial deposition runs showed poor adhesion between the Nickel and the quartz and high surface tensile stress in the Nickel layer. An adhesive tape test of the Nickel layer resulted in a total liftoff of the tested area. Therefore, an adhesive layer was required between the Nickel and the quartz. A 100 Angstrom thick adhesive layer of a significantly oxygen-active metal (strongly negative free energy of formation) significantly improves surface adhesion by forming strong covalent bonds with the oxide substrate and metallic/ionic bonds with the Nickel layer. Both Chromium and Titanium are very oxygen-active and have been used successfully as adhesion layers for metal on glass substrates. However, although Titanium has a significantly more negative free energy of formation than Chromium, Chromium was selected as the adhesive in this case because it is significantly easier to etch than Titanium and therefore made the subsequent patterning process much easier. The evaporation deposition was conducted with a chamber pressure less than $6.0 \times 10^{-7}$ torr and deposition rates of 2 Angstroms per second for Chromium and 3 Angstroms per

second for Nickel. Note that both layers were deposited during a single cycle so that the vacuum was not broken between depositions of the layers. The Chromium layer significantly improved the surface adhesion of the Nickel as shown by the adhesive tape test, which did not remove any of the deposited film.

Once deposited, the Nickel layer was patterned to the appropriate sensor geometry using a photoresist mask and an isotropic wet etch. A one micrometer thick layer of standard positive photoresist (Olin 825) was spun onto the substrates using a spin-coater, with Hexamethyldisilazane (HMDS) used to improve the photoresist adhesion. The photoresist was soft-baked at 90°C and then exposed using a direct contact, glass mask with a positive chrome pattern. The mask pattern is shown below in Figure 6-2. Since the actual volume resistivity of the Nickel layer was difficult to predict due to errors in the coating thickness and possible impurities in the Nickel, 15 sensors of 3 different nominal aspect ratios (12.5, 16, 20) were patterned onto each substrate to ensure the process would produce a sufficient number of sensors of usable resistance. The glass/chrome mask was created using an emulsion transparency and a blank, chrome coated glass plate through a standard photolithography process developed by Rebecca Jackman and Sameer Ajmera of the MIT TRL. Creating the mask using an emulsion transparency was significantly less expensive than outside vendor fabrication, but the emulsion transparency process is limited to a minimum feature size of 25 micrometers. The photoresist was then developed (using Olin 934 3:2 developer) and hard-baked at 105°C to increase its resistance to the acid etch. The etch used for the Nickel was a solution of 20 : 16 : 5 : 70 nitric acid, acetic acid, sulfuric acid and deionized water. At room temperature the etch rate of this solution was 50 Angstroms per second. After completely etching away the Nickel layer, the remaining 100 Angstrom Chromium layer was etched away using a commercial Chromium etchant (CR-7) for 10 seconds.

After the etch was completed, the remaining photoresist could not be removed by typical solvents such as acetone, and was instead removed with a 30 minute cycle in an Oxygen plasma asher.

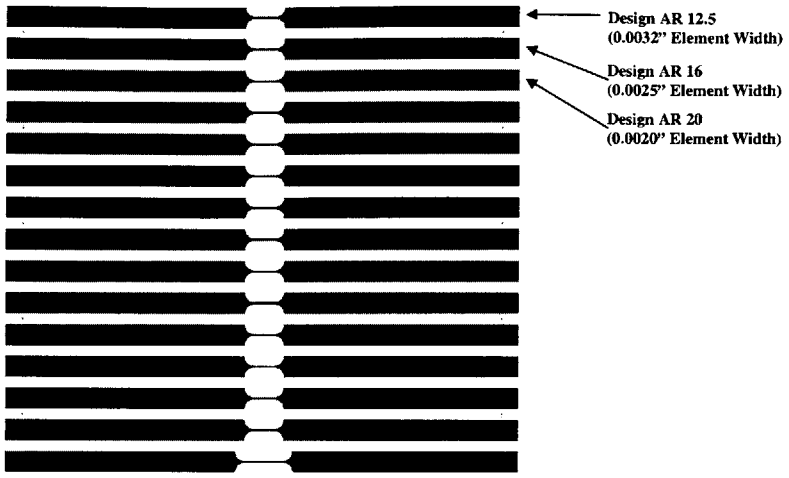


Figure 6-2. Nickel Mask Pattern.

The Gold layer for the sensor leads was then deposited using electron beam evaporation. To ensure adequate surface adhesion between the Gold and the Nickel, a 100 Angstrom adhesive layer of Titanium was used. The chamber pressure and deposition rates were the same as noted above for the Chromium/Nickel deposition process. With the Titanium layer, the adhesive tape test did not remove any of the gold film. The gold layer was patterned using a physical mask, in this case a 1.016mm (0.040") diameter copper wire, to shield the sensor elements during deposition.

Measurements of the sensor dimensions were performed using a diamond stylus TENCOR P-10 surface profilometer. Table 6-2 below shows the design and actual dimensions of the sensor elements. Note that the roughly 12% error in the lengths of the sensor elements is due to undercutting in the isotropic wet etches used to pattern both the chrome mask and the Nickel film. The error in the widths of the elements was due to the difference between the actual diameter of the copper wire used as the mask and the size of the shadow it projected onto the substrate.

| Sensor Characteristics | Design Aspect Ratio | | |
|---|---|---|---|
| | 12.5 | 16.0 | 20.0 |
| Actual Aspect Ratio | 13.8 | 16.7 | 22.5 |
| Design Width | 1016μm (.0400") | | |
| Measured Width | 995μm | | |
| Design Length | 81.3μm (.0032") | 63.5μm (.0025") | 50.8μm (.0020") |
| Measured Length | 72.2μm | 59.5μm | 44.2μm |
| Design Ni Thickness (w/Cr Layer) | 2100 Angstroms | | |
| Measured Ni Thickness (w/Cr Layer) | 2061 Angstroms | | |
| Design Au Thickness (w/Ti Layer) | 2100 Angstroms | | |
| Measured Au Thickness (w/Ti Layer) | 1980 Angstroms | | |
| Design Al2O3 Thickness | 20,000 Angstroms | | |
| Measured Al2O3 Thickness | 19,353 Angstroms | | |
| Ni Theoretical Resistivity | $6.84 \times 10^{-8}$ Ωm | | |
| Ni Measured Resistivity (Before Bake) | $1.17 \times 10^{-7}$ Ωm | | |
| Ni Measured Resistivity (After Bake) | $9.86 \times 10^{-8}$ Ωm | | |

Table 6-2. Sensor Characteristics.

The aluminum oxide protective coating was sputtered onto the sensor elements with the sensor leads physically masked by Kapton© film. Table 6-2 above shows the nominal and the measured thickness for the protective coating. Figure 6-3 below shows the completed sensor with the Aluminum Oxide protective coating.

After the protective coating was applied, the substrates were cut into individual sensors measuring 5.76mm x 1.59mm using a diamond saw with a 340 micrometer wide blade.

The individual sensors were then heated to 300°C for 12 hours to stabilize the sensor element resistance. Thin metal films deposited by evaporation typically exhibit high values of residual tensile stress. As the film ages the residual stress gradually relaxes and the resistance of the film decreases over time to a limiting value. Heat treating the sensors accelerates the aging process and reduces the film resistance.

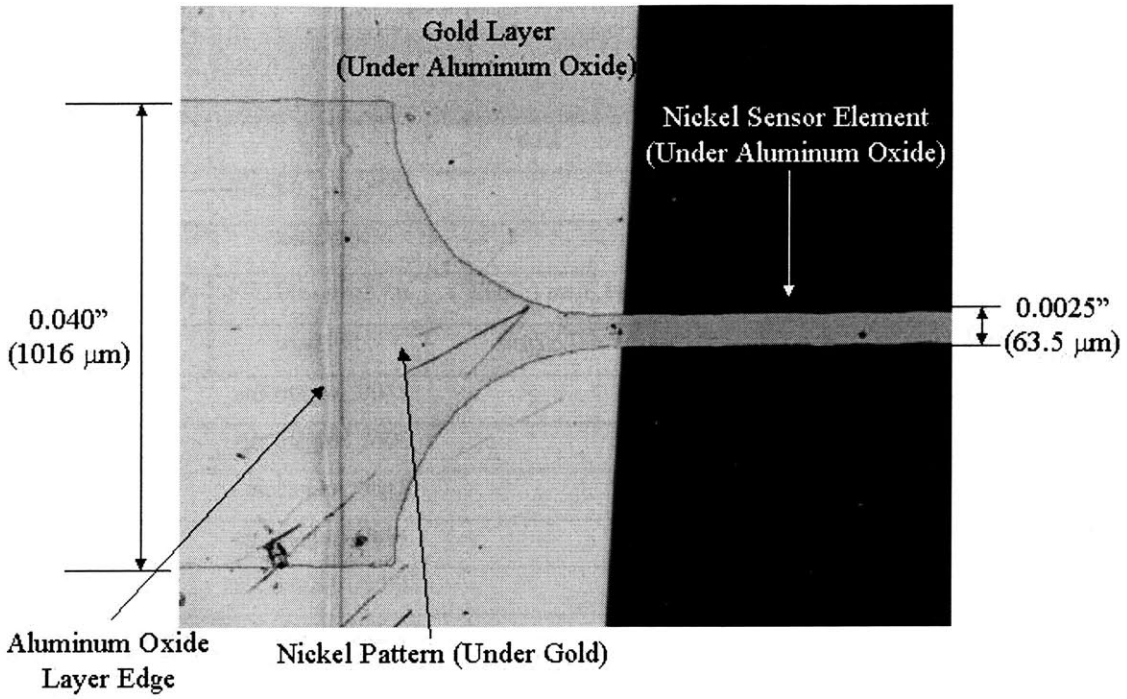


Figure 6-3. Hot Film Sensor Top View.
(5x Magnification)

Although some references recommend as much as 72 hours of heat treatment at 300°C for Nickel [18], experiments performed on 1500 Angstroms thick evaporated Nickel on quartz coatings indicated that the minimum resistance value is reached in less than 12 hours. Table 6-2 shows the measured resistivity of the Nickel film both before and after heat treatment. The resistivity values were computed by averaging the values from 14 sensors from the same substrate piece and neglecting the effect of the Chromium adhesive layer. Heat treatment caused an average reduction in the film resistivity to 84% of the pre-heat treatment value, although for individual sensors the effect varied widely (from 93.1% to 72.7%).

The fabrication procedure detailed above can produce relatively inexpensive sensors on flat surfaces in any configuration with a minimum feature size of 25 micrometers. Thus, the creation of tightly spaced sensor arrays and even arrays with sensors oriented at angles to each other for directional measurements is feasible.

In order to perform a series of characterization tests on the sensors, they were placed into Aluminum probe holders. The probe holder design and dimensions are shown below

in Figure 6-4. Aluminum was selected for the probe holder because of its strength, its temperature range, and most importantly, the fact that it can be anodized after machining in order to provide a wear resistant surface. Note that although probe head sizes as small as $^{1}/_{16}$ of an inch in diameter are feasible with the current sensor design, the size of the probe head was selected as $^{3}/_{8}$ of an inch in diameter for convenience in fabrication and ease of handling during subsequent tests. The quartz substrate with the sensor element fits as an insert into the slot on the head of the probe holder, using M-Bond 610© high temperature strain-gauge glue as the adhesive. 0.003" OD wires were soldered to the gold leads at either end substrate and passed through holes in the probe holder to larger Teflon coated 0.032" OD wires, which were secured using Ecobond 104© high temperature epoxy. The selection of wire types and adhesives guaranteed effective performance throughout the required temperature range for the sensor established in Section 4.2.1.

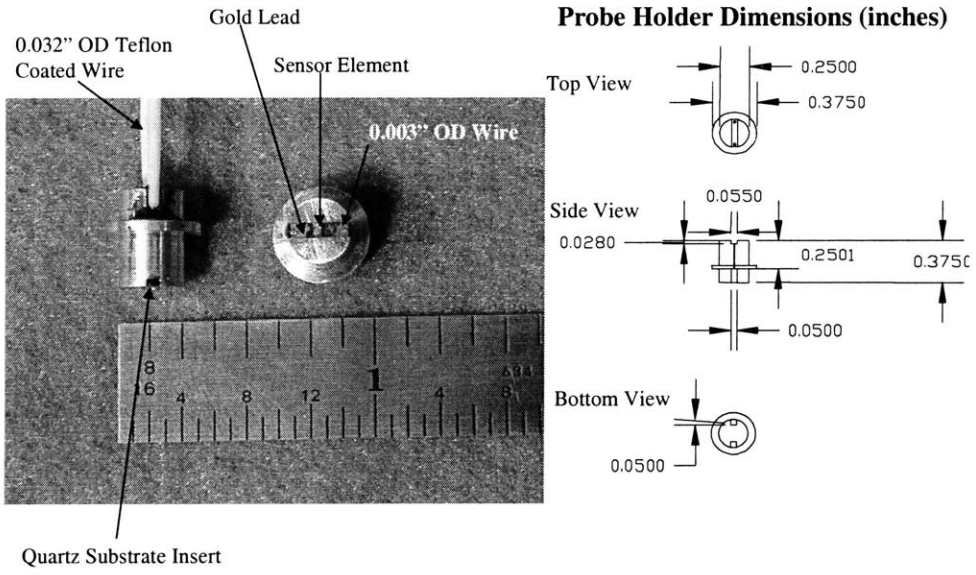


Figure 6-4. Completed Robust Hot Film Sensor with Aluminum Probe Holder.

# 7 Robust Sensor Characterization Tests

The robust sensors were subjected to four sets of tests to characterize and evaluate their performance against the requirements established in Chapter 4: TCR stability, steady-state sensitivity, dynamic response, and sand abrasion.

## *7.1 Temperature Coefficient of Resistivity Stability*

### *7.1.1 Intent*

The purpose of the TCR stability tests was to quantify the change in the performance of the robust sensors with time due to changes in TCR.

### *7.1.2 Methodology*

Two sensors were tested, one uncoated AR 16 robust sensor and one SENFLEX® 9902 single element sensor with the same characteristics as the sensors detailed in Table 2-1. The TCR for the sensors was determined by taking a linear fit of direct measurements of temperature and sensor resistance. Typically, TCR for hot film sensors is based on the sensor resistance at 20°C ($R_{20}$) and is defined as:

$$TCR \equiv \frac{1}{R_{20}}\left(\frac{\Delta R}{\Delta T}\right). \qquad \text{(Equation 7.1)}$$

But, because data was not taken at 20°C, the value of $R_{20}$ was determined for each sensor using the slope of the linear fit and the lowest temperature data point. Note that the $R_{20}$ value was only computed in order to compare the sensor TCR with the theoretical value for Nickel. For relative comparisons between the robust sensor and the SENFLEX® sensor, $TCR_{50}$ was computed using the sensor resistance at 50°C ($R_{50}$) which was directly measured.

In order to simulate the time aging of the sensors as discussed in Section 4.3, the sensors were electrically heated using DANTEC 56C17 CTAs to the maximum required sensor temperature (200°C) for 126 cycles of 10 minute duration in a no flow condition. In order to set the CTA bridge to give a sensor temperature of 200°C, the resistance value $R_h+R_l$ (where $R_h$ is the resistance of the sensor at 200°C and $R_l$ is the lead and cable

resistance for the sensor) must be known. $R_h$ was determined from the initial TCR experiment, and $R_l$ was computed from direct measurements of both R and $R+R_l$. The CTA bridge was reset after each TCR measurement, using the new TCR to ensure the sensor temperature was as close to 200°C as possible.

### *7.1.3 Experimental Facility*

The temperature measurements for the sensors were taken using a Hart Scientific 6330 Temperature Calibration Bath with an internal platinum resistance thermometer and Dow Corning 200.20 silicone oil as the working fluid. In order to suspend the robust sensor in the oil bath, it was mounted without an Aluminum probe holder to a glass rod as shown in Figure 7-1 below, such that the sensor substrate and the glass rod were not in physical contact to prevent any temperature loss due to conduction through the glass rod. The SENFLEX sensor was mounted to a $^1/_{16}$ inch Aluminum plate using M-Bond 610© high temperature adhesive for testing in the oil.

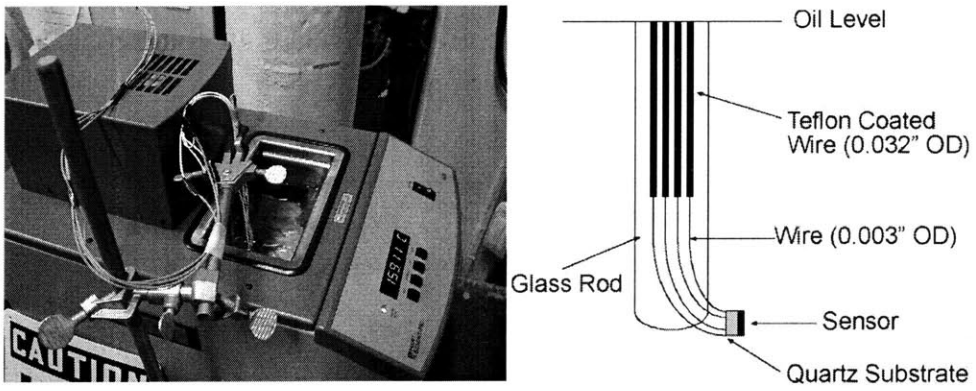


Figure 7-1. TCR Test Experimental Setup.

The resistance measurements were taken using a four-wire connection to a Hewlett-Packard 34401A Multimeter (100μΩ resolution). The four-wire connection provides a very accurate resistance measurement by using separate pairs of wires to

transmit the test current and to measure the associated voltage drop. The test current during all of the experiments was one milli-Ampere.

Data acquisition was performed by a National Instruments LabVIEW data acquisition system (DAQ). For each temperature set point, the temperature of the bath was stabilized to within ±0.05°C of the set point for two minutes. After the bath temperature was stabilized, ten simultaneous temperature and resistance measurements were taken at 0.5 Hz. These temperature and resistance measurements for each temperature set point were averaged to provide a single temperature and resistance data point.

### *7.1.4 Results & Discussion*

Figure 7-2 below shows the results from the initial test of both the robust sensor and the reference sensor (no thermal cycling). The robust sensor had a TCR of 0.63%/°C, approaching the theoretical TCR value for bulk Nickel of 0.69%/°C, while the reference sensor had a TCR of 0.39%/°C. Typical TCR values for commercial Nickel film sensors are approximately 0.35%/°C.

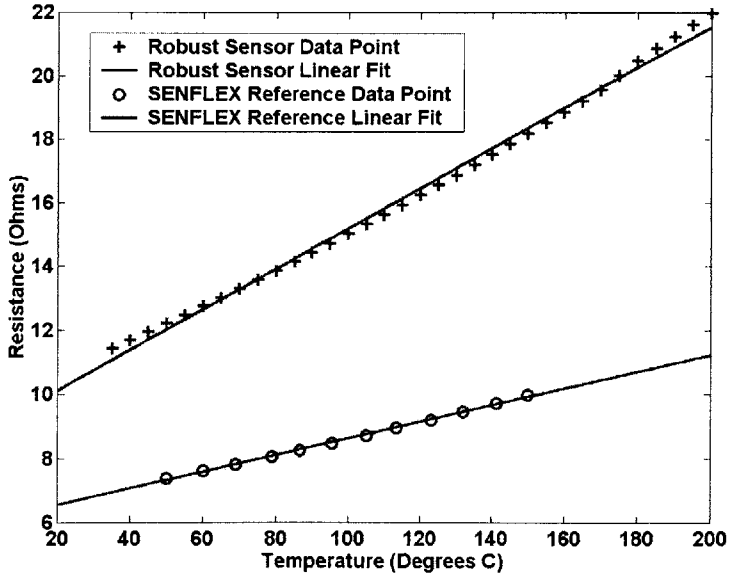


Figure 7-2. TCR Results.

Figure 7-3 below shows the value of $TCR_{50}$ normalized by the zero cycle $TCR_{50}$ value as a function of the number of thermal cycles for both the robust sensor and the SENFLEX reference sensor. For the evaluation of the change in $TCR_{50}$ over time, the $TCR_{50}$ for the robust sensor was computed using 12 data points evenly spaced from 40°C to 150°C while the $TCR_{50}$ for the SENFLEX reference sensor was computed using 6 data points even spaced from 50°C to 150°C .

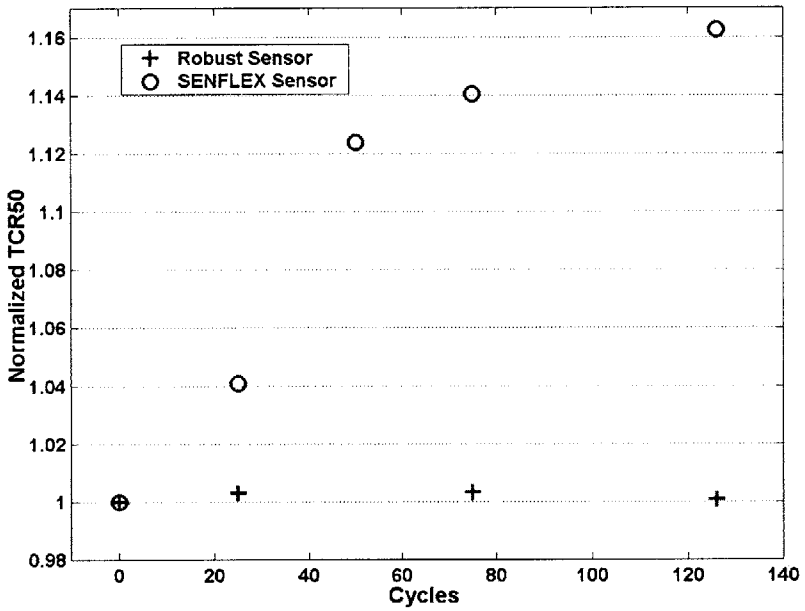


Figure 7-3. Effect of Thermal Cycling on Sensor TCR.

The large change in the $TCR_{50}$ of the SENFLEX sensor over time was due to the reduction of the sensor resistance due to aging (see Section 4.3.3). The robust sensor, which was heat treated to reduce the effect of aging, showed a very low maximum variation in $TCR_{50}$ of 0.32%. Thus, the results indicate that even operating at the maximum sensor temperature, the robust hot film sensors can maintain a consistent TCR value throughout the entire required design life.

The uncertainty involved in the computation of the $TCR_{50}$ was negligible given that the maximum error in the temperature measurement from the calibration bath was ±0.035°C and the maximum error in the resistance measurements from the multimeter was ±0.0062 Ω. For both the resistance and the temperature measurements, the maximum errors were below 0.1% of the measurement.

## *7.2 Steady-State Sensitivity*

### *7.2.1 Intent*

The primary intent of the steady-state sensitivity tests was to establish that the robust sensors are sensitive enough to small changes in surface shear stress to provide useful data about flow conditions in the inlet. Because the shear profile of the flow in the regions of interest in the inlet is not known, defining a minimum required sensitivity is not practical. Therefore, the sensitivity tests evaluated the sensitivity of the robust sensors against the sensitivity of the commercial hot film sensors used successfully in the small-scale inlet experiments described in Chapters 2 and 3. Also, the sensitivity tests were used to verify the predicted effects of changes in the sensor aspect ratio, overheat temperature, and the addition of the protective coating on the sensor sensitivity.

### *7.2.2 Methodology*

The sensitivity of a hot film sensor is an expression of the change in power dissipated in the sensor due to a change in the surface shear stress. In order to measure the sensitivity accurately, the surface shear stress must be known. Therefore, the sensitivity tests were conducted using a laminar flat-plate flow for which the shear stress could be accurately computed using the Blasius solution.

For laminar flow, the heat transferred from the sensor to the flow by forced convection is proportional to the surface shear stress to the $^1/_3$ power. Therefore, the relationship between the CTA output voltage (which is proportional to the power dissipated in the sensor) and the shear stress is approximated by:

$$E_{out} = E_o + B(\tau_w^{1/3}) \qquad \text{(Equation 7.2)}$$

where $E_o$ is the output voltage with no flow. In dimensionless terms, the relationship is:

$$Nu = Nu_o + B(Pe^{1/3}) \qquad \text{(Equation 7.3)}$$

where $Nu_o$ is the sensor Nusselt number with no flow. In either case, B is defined as the sensor sensitivity. It is important to note that this linear approximation is only valid where forced convection is the dominant mode of heat transfer. Therefore, it is not valid at extremely low Peclet number values, and the actual $Nu_o$ is much larger than the $Nu_o$ predicted by Equation 7.3. Although the sensitivity values computed are only valid for

laminar flow, the laminar flow method provides a means for an accurate relative comparison.

The Nusselt number is defined as: $Nu \equiv \frac{P}{w_e k_f \Delta T}$. The value of the overheat temperature ($\Delta T$) was determined from the known sensor temperature and an ambient flow temperature measurement taken abeam the sensor location. The sensor temperature was set by placing the sensors to be tested into a temperature calibration oil bath (described previously in Section 7.1.3) with all of the same cabling used in the wind tunnel tests. The bath was heated to the desired sensor temperature and stabilized to within 0.01°C, as measured by the bath's internal platinum resistance thermometer. The corresponding resistance measured for the sensor and cables ($R_h$+$R_l$) is the resistance value set into the CTA bridge to ensure that the sensor is maintained by the CTA at the correct temperature.

The power dissipated (P) was computed from the output voltage of the CTA. For the DANTEC 56C17 CTAs used, the relationship between power dissipated in the sensor and the output voltage ($E_{out}$) is as follows:

$$P = \left( \frac{1.05 E_{out}}{R_h + R_l + 20\Omega} \right)^2 R_h \qquad \text{(Equation 7.4)}$$

Where $E_{out}$ was directly measured, $R_h$+$R_l$ was known (as described above), and $R_h$ was computed by direct measurements of R and R+$R_l$.

The Peclet number is defined as: $Pe \equiv \frac{s l_e^2}{\alpha_f}$ where the surface shear (s) was computed from direct measurements of the ambient pressure, flow temperature, and flow velocity at the sensor location using a dimensional form of the Blasius solution:

$$s = 0.332 (U_o^{3/2}) \sqrt{\frac{\rho}{\mu x}} \qquad \text{(Equation 7.5)}$$

where $U_o$ is the freestream velocity, $\rho$ is the air density, $\mu$ is the air viscosity, and x is the stream-wise coordinate along the flat plate.

Once the Nu and Pe were computed for each flow velocity, the sensitivity value (B) was then be determined by a linear regression of the data points, excluding the zero-flow point which did not follow the linear relationship.

### *7.2.3 Experimental Facility*

The sensitivity tests were conducted by mounting a commercial reference sensor and a robust test sensor flush with the surface of a flat plate suspended in a low speed wind tunnel test section at zero angle of attack. The leading edge of the flat plate was machined with an 80° angle knife-edge to ensure a Blasius flow over the sensors. A photograph and diagram of the wind tunnel test section is shown below in Figure 7-4.

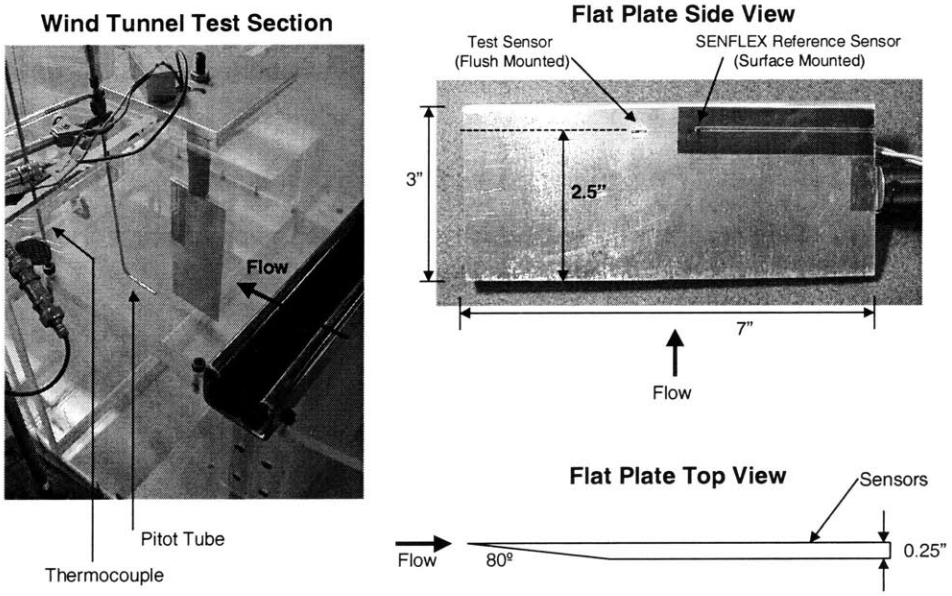


Figure 7-4. Sensitivity Test Experimental Setup.

The reference sensor was a SENFLEX® SF9902 single element hot film sensor glued to the surface with exactly the same characteristics as the sensors detailed in Table 2-1. The purpose of the reference sensor was to provide a comparison for the sensitivity of the test sensor, and to ensure that the flow conditions did not vary significantly from one test run to the next. The test sensor with an Aluminum probe holder (as shown in Figure 6-4) was inserted into the flat plate so that the sensor was mounted flush with the surface.

Both the reference and the test sensor were controlled by DANTEC 56C17 CTAs with the CTA output voltages simultaneously recorded by an ADTEK AD-380 12-bit high speed analog to digital data acquisition system. A single steady state output voltage was determined for each flow velocity by averaging 1000 measurements per sensor taken at 10 kHz.

The wind tunnel velocity was measured using a pitot tube connected to a SETRA differential pressure transducer (0-0.25" water). Ambient pressure was measured using a SETRA absolute pressure transducer (0-100 psi). Flow temperature was measured using a thermocouple suspended in the flow.

The tests were conducted at flow velocities of up to 11 m/s, with the Reynolds Number based on the momentum thickness ($Re_\theta$) always less than 200, which is the minimum required for the flow to transition from laminar to turbulent due to surface roughness, bumps or other flow disturbances [8]. Therefore, the flow for all of the tests was fully laminar.

### *7.2.4 Results & Discussion*

Tests were conducted on sensors of different aspect ratio both with and without the Aluminum Oxide protective coating. Table 7-1 below lists the results for each sensor tested and the corresponding reference sensor values for each test run.

| Sensitivity Test Results | | | | | |
|---|---|---|---|---|---|
| **Sensor Description** | **R (Ω)** | **Sensor Temp (°C)** | **Dimensionless Sensitivity** | **Actual $Nu_0$** | **Dimensional Sensitivity ($V/Pa^{1/3}$)** |
| Uncoated AR 12.5 | 6.2 | 100.0 | 3.00 | 51.3 | 0.128 |
| Reference Sensor | 6.5 | 150.0 | 4.59 | 35.4 | 0.651 |
| Uncoated AR 12.5 | 6.2 | 147.6 | 3.27 | 55.5 | 0.247 |
| Reference Sensor | 6.5 | 150.0 | 4.53 | 35.6 | 0.682 |
| Uncoated AR 12.5 | 6.2 | 179.5 | 3.23 | 57.8 | 0.252 |
| Reference Sensor | 6.5 | 150.0 | 4.59 | 35.7 | 0.672 |
| Coated AR 12.5 | 5.1 | 147.6 | 3.09 | 59.1 | 0.191 |
| Reference Sensor | 6.5 | 150.0 | 4.48 | 35.9 | 0.628 |
| Coated AR 16 | 7.9 | 147.6 | 3.73 | 56.9 | 0.229 |
| Reference Sensor | 6.5 | 150.0 | 4.58 | 35.7 | 0.679 |

Table 7-1. Sensitivity Test Results.

The reference sensor results indicate a relatively high degree of repeatability in the flow conditions. The reference sensor dimensionless sensitivity varied less than 1.7% from the mean for all the flow conditions while the $Nu_o$ value varied less than 1% from the mean for all tests. As expected, the reference sensor has a much lower $Nu_o$ value than the test sensors due the difference in the conductivity ratio (K) between the polyimide substrate in the reference and the quartz substrate in the test sensors. The results also indicate that the reference sensor had a higher sensitivity than all of the robust test sensors, which was unexpected since the test sensors had a significantly higher TCR and comparable or greater aspect ratio, and will be discussed later in more detail.

As shown in Table 7-1 and Figure 7-5 below, the results verify Kalumuck's assertion that increasing the sensor aspect ratio increases the sensitivity while decreasing the zero-flow Nusselt number ($Nu_o$). Figure 7-5 shows both the individual data points as well as the linear curve-fit for each sensor.

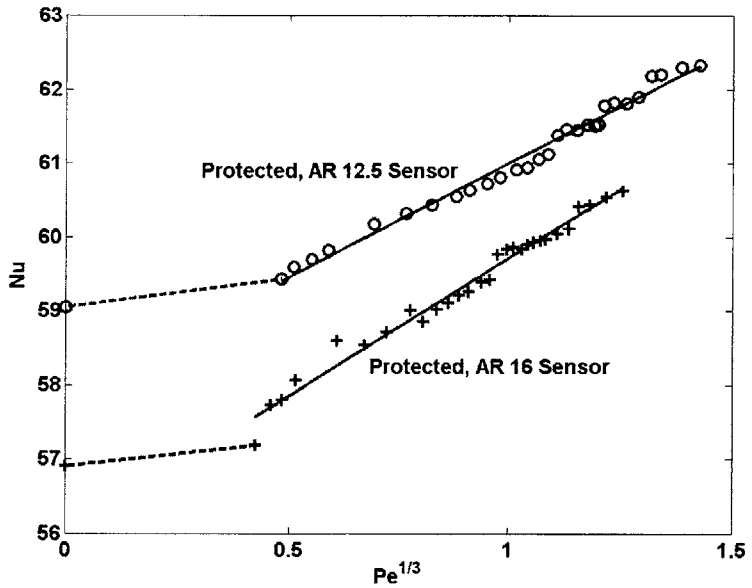


Figure 7-5. Effect of Aspect Ratio
on Steady-State Sensor Performance.

The sensor results also demonstrate the effect of the overheat temperature on the sensor performance. Figure 7-6 shows the dimensional and the dimensionless results for the same sensor at three different sensor temperatures. The mean flow temperature for the test runs was approximately 20°C. The data suggests that increasing the overheat temperature improved the sensor sensitivity. However, the tests found no significant

advantage to increasing the sensor temperature above 150°C (corresponding to an overheat value of 130°C). Increasing the sensor temperature also increased the non-flow-sensitive portion of the power applied to the sensor (increasing $Nu_o$), making accurate measurements of the flow sensitive power changes more difficult to resolve.

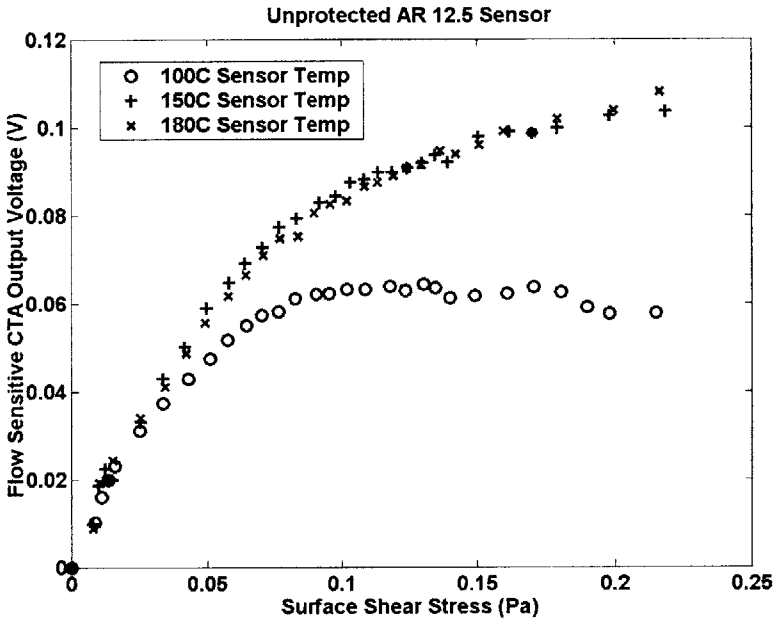


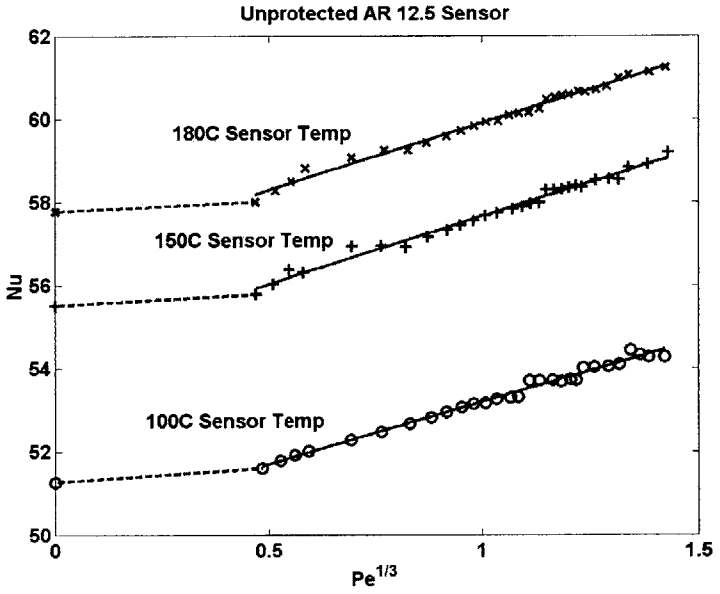


Figure 7-6. Effect of Overheat Temperature on Steady-State Sensor Performance.

Most importantly, the sensitivity results show the effect of the two micrometer thick Aluminum Oxide coating on the sensitivity of the robust sensors. For the comparison of the coated and uncoated sensors, the dimensionless sensitivity is not accurate because the sensor length used in the definition of the Peclet number is not correct due to the diffusion of heat through the coating, which increases the effective length of the coated sensor at the convective surface. Therefore the dimensionless sensitivity for the coated sensor is slightly overstated. Another method to compare these two sensors since they have the same physical dimensions and test conditions is to consider the dimensional sensitivity. From a comparison of the results of the coated 12.5 AR sensor with the uncoated 12.5 AR sensor it is clear that the coating caused an increase in the $Nu_o$ value and a decrease in the sensitivity. Thus, the effect of the coating was to diffuse the heat from the sensor and decrease the effective aspect ratio of the sensor at the convective surface. This result further underscores the importance of using a high aspect ratio for the robust sensor in order to compensate for the effect of the coating. But, the decrease in dimensional sensitivity due to the coating was on the order of only 28%, and could have been offset by an increase in the signal gain of the coated sensor by a factor of 1.28. Therefore, the effect of the coating on the sensitivity was minor and could be easily compensated for by a modest increase in the output voltage gain.

The sensitivity tests demonstrate that the robust sensors can achieve a sensitivity value of the same order as the commercial sensors used in the small-scale experiments. Table 7-1 shows that robust sensors of the aspect ratios tested can achieve dimensionless sensitivity values of up to 82% of the mean value of the unprotected commercial sensor. The lower sensitivity for the test sensor is most likely due to the presence of the Aluminum probe holder. Kalumuck's work [12] indicates that placing a sensor in a material with a higher conductivity ratio than the actual substrate will lower the sensitivity of the sensor provided the thermal boundary layer of the sensor is large enough to interact with the surface beyond the actual substrate. Since the conductivity ratio of the Aluminum probe holder is two orders of magnitude larger than the substrate conductivity ratio, and the tests were conducted at sufficiently low Peclet number values for the thermal boundary layer to extend past the substrate, the presence of the probe

holder certainly affected the sensitivity result. This reduction in sensitivity could be corrected by using a material for the probe holder with a thermal conductivity of the same order as the sensor substrate. However, this sensitivity reduction is minor and will diminish as the Peclet number for the flow increases. For the AR 16 protected sensor, an increase in the output voltage gain of a factor of 3 gives the same dimensional sensitivity as the commercial reference sensor. Thus, although some gains in sensitivity can be made by making the probe holder out of a material with a lower thermal conductivity ratio, the reduction in sensitivity is not significant and can be easily compensated for by a modest increase in the signal gain.

### *7.3 Dynamic Response*

#### *7.3.1 Intent*

Dynamic response tests of the sensor were conducted to determine the dynamic amplitude and phase response of the robust sensor. The minimum dynamic response requirements for the robust sensor were developed previously in Section 4.3.1.

#### *7.3.2 Methodology*

The dynamic response of the robust sensor was determined by placing the sensor in the output flow of a high speed rotary valve capable of producing a flow oscillation frequency greater than 1 kHz. However, since the exact output flow characteristics of the rotary valve were not known, the frequency response of the robust sensor was determined through a comparison with a reference sensor with a frequency response greater than 1 kHz.

The comparison of the performance of the robust sensor and the reference sensor was performed by considering the complex transfer function between them with the reference sensor output voltage as the input and the robust sensor output voltage as the output. The complex transfer function was computed using only those data points in both signals with greater than 0.95 coherence.

In order to determine the amplitude response of the test sensor, the amplitude of the transfer function was normalized by the amplitude for the lowest flow oscillation frequency. The resulting normalized transfer function magnitude shows the relative amplitude response of the robust sensor and the reference sensor. A decrease in the amplitude performance of the robust sensor relative to the reference sensor as the oscillation frequency increased would appear as a decrease in the normalized transfer function magnitude.

To analyze the phase response, the phase of the complex transfer function was examined. No attempt was made to determination the exact phase lag of the sensor due to the uncertainty in the phase response caused by small stream-wise variations in the locations of the hot films and the reference hot wire as well as the phase difference between the surface shear stress measured by the hot films and the flow velocity outside

of the boundary layer measured by the hot wire. The work of Cook, Giddings and Murphy [6] shows that for laminar flow the oscillations in the surface shear stress actually lead the oscillations in the edge velocity. The amount of lead is zero in steady-state and increases with increasing frequency of oscillation, with an asymptote at 45 degrees. Thus, the examination of the phase response was intended only to provide insight into the general behavior of the sensor. In order to examine the phase response, the phase of the transfer function at each point was adjusted so that the point of maximum phase was set to zero. With this adjustment, the phase of the transfer function provides a best-case estimate of the phase response of the sensor. Note that any increase in the phase lag of the robust sensor relative to the reference sensor resulted in a decrease in the phase of the transfer function.

### *7.3.3 Experimental Setup*

The experimental setup for the dynamic tests is shown below in Figure 7-7. The oscillating airflow was produced using a high speed rotary valve designed by Brian McElwain of MIT. The design and operating characteristics of the rotary valve are covered in detail in McElwain's thesis, which has not yet been published. The rotary valve accepted pressurized air through a supply line and passed it through a channel with a high speed valve to two output slots. The high speed valve was simply a spinning disc with 10 holes evenly spaced along its circumference which therefore imparted an oscillation to the flow with a frequency of 10 times the motor shaft speed. Motor shaft speed was monitored using an encoder. Since the motor shaft had 16 gear teeth, the ratio of the frequency measured by the encoder to the actual velocity output frequency was 1.6. The rotary valve was operated at a supply pressure of 15 psi gauge.

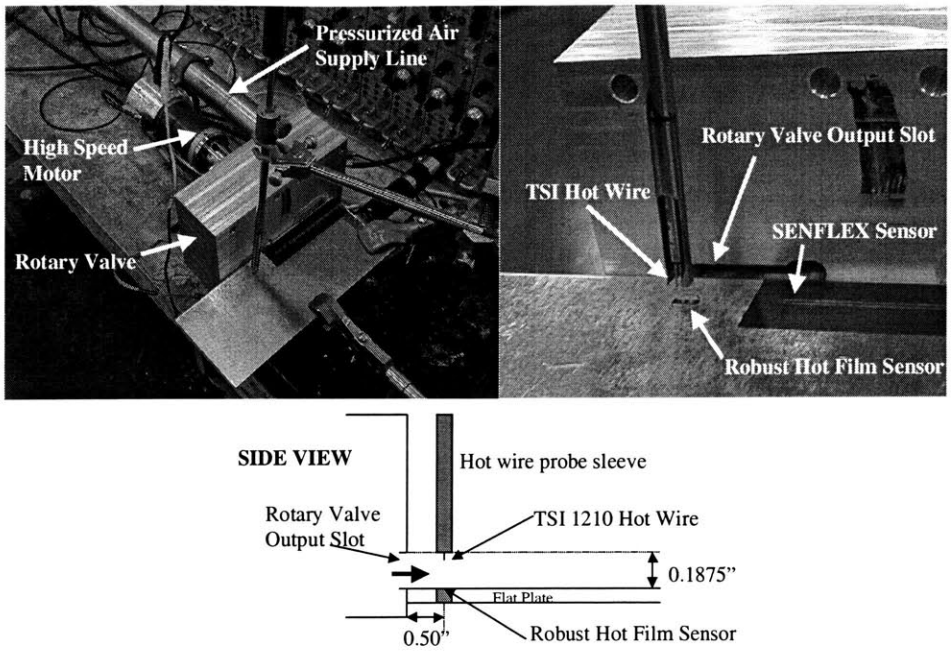


Figure 7-7. Dynamic Response Test Experimental Setup.

The flat plate shown in Figure 7-4 was placed against the rotary valve with the upper surface of the plate flush with the lower edge of the rotary valve output slot as shown in Figure 7-7. The robust hot film sensor was mounted in the flat plate so that the sensor element was flush with the plate surface. The robust sensor used was the same coated, AR 16 sensor used in the steady-state sensitivity tests in Section 7.2 above. The robust hot film sensor and the SENFLEX sensor were operated using DANTEC 56C17 CTAs with 5 meter cable lengths and an overheat ratio of 1.5. The output voltages from the 56C17 CTA were passed through a DANTEC 56N20 Signal Conditioner to AC couple and amplify the signals. The signal conditioners were both set with the highpass filter at 1 Hz, the lowpass filter at 3 kHz, and the gain at 50. The internal settings for the CTAs were the same as those listed in Table 2-3.

The reference sensor was a TSI 1210 Hot Wire placed just below the upper edge of the rotary valve output slot (as shown in Figure 7-7) to ensure it was inside the output flow but outside of the flat plate boundary layer. Tests were conducted with the hot wire positioned directly above both the robust hot film sensor and the SENFLEX® hot film sensor. The hot wire was operated using a DANTEC 56C17 CTA with a 5 meter cable length and the same settings shown in Figure 2-3, except the internal amplifier frequency

response shape was set for a hot wire (1.2 dB/octave). The hot wire was operated at the overheat resistance recommended by the manufacturer of 12.15 Ω. The CTA output was AC coupled and amplified using a DANTEC 56N20 Signal Conditioner with the same settings noted above for the robust sensor except the gain was set to 10.

Data acquisition was performed using a TMS320-based Texas Instruments Digital Signal Processor (DSP) board with 8 channels controlled by a C based software interface. Data for each measurement was taken at 10 kHz per channel for 5 seconds.

### *7.3.4 Results and Discussion*

Figure 7-8 below shows the normalized transfer function magnitude and the adjusted transfer function phase for the signals from the robust sensor and the hot wire reference sensor. The normalized transfer function magnitude shows that the robust hot film sensor's amplitude response did not decay significantly (less than 3 dB) relative to the hot wire up to 1 kHz, the maximum frequency tested.

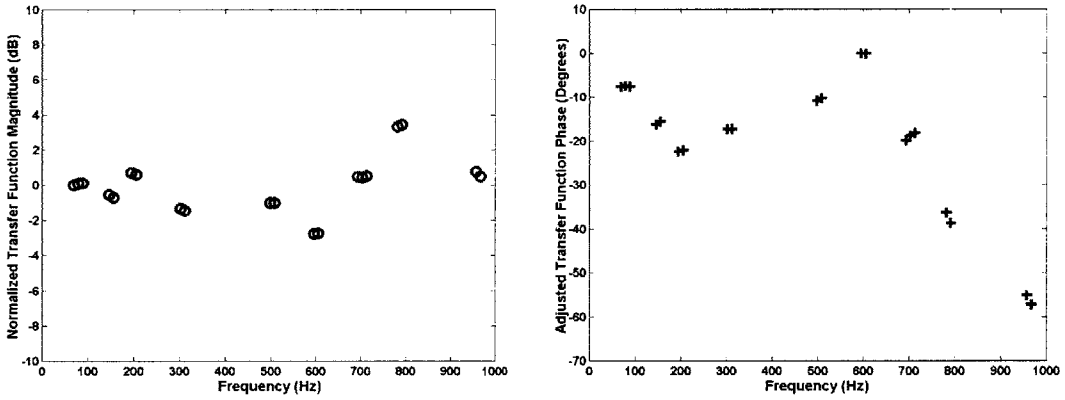


Figure 7-8. Robust Hot Film Sensor Transfer Function.

The adjusted phase of the transfer function shows that the phase lag of the robust sensor initially increased as the frequency was initially increased and then decreased with

increasing frequency until at approximately 600 Hz where the phase lag increased again with frequency to 1 kHz. The shape of the transfer function phase plot can be explained by the combined effects of the substrate and the protective coating. Up to approximately 600 Hz, the phase lag was governed by the response of sensor substrate. As noted by Cole and Beck [3], the phase lag of an uncoated hot film sensor is caused by the fact that the steady state heat distribution along the hot film sensor element is different at different flow conditions even though the average temperature of the element is the same. As the flow changes rapidly, the substrate is unable to instantaneously assume the new temperature distribution and thus the probe signal lags the flow. At low frequencies the phase lag increases with increasing frequency because the characteristic time is large enough that the entire substrate (or at least a significant portion) is affected by the transient changes in the flow. As the frequency continues to increase, less and less of the substrate is involved in the transient heat transfer problem and the phase lag decreases. If there were no protective coating, one would expect the phase lag to continue to decrease with increasing frequency, which is exactly the behavior exhibited by the SENFLEX® uncoated hot film sensor. Thus, the sharp increase in the phase lag at 600 Hz indicates that near 600 Hz the lag caused by the protective coating dominated the phase response of the sensor. Note that the substantial increase in the phase lag of the sensor due to the protective coating occurred at a far lower frequency than predicted by the one-dimensional model results in Section 5.4.

Thus, from the results shown in Figure 7-8, the robust sensor met the requirements for amplitude response with a -3bB cutoff frequency clearly in excess of 1 kHz. The adjusted transfer function phase results show that the protective coating of the robust sensor did not affect the phase response of the sensor until approximately 600 Hz. Below 600 Hz, the phase lag was caused by the effect of the sensor substrate (and the Aluminum probe holder). Since the adjusted transfer function plot in Figure 7-8 represents a best case probe performance due to the assumption of zero phase lag at 600 Hz, it is clear that the robust sensor phase lag most likely exceeded the 20 degrees limit set in Section 4.3.1 for a significant portion of the frequency range. However, significant improvements in the phase response below 600 Hz could be realized by limiting the amount of the substrate that is involved in the transient heat transfer. Limiting the

amount of substrate can be done by isolating the quartz insert from the Aluminum probe holder using a thick insulating layer with a very low thermal diffusivity or by making the probe holder itself out of a material with a significantly lower thermal diffusivity than the quartz substrate.

## *7.4 Sand Abrasion*

### *7.4.1 Intent*

The intent of the sand abrasion experiments was to demonstrate the feasibility of using the robust sensors in actual production aircraft exposed to a blowing sand environment. The abrasion tests were conducted at zero angle of incidence (parallel) to the flow in order to provide results independent of the actual full-scale inlet geometry.

### *7.4.2 Experimental Setup*

The abrasion tests were conducted by injecting sand particles into a nozzle which produced a high velocity air jet incident upon a target sensor. Figure 7-9 shows an overview of the experimental facility. The discussion below covers the five major components of the facility in detail: the air source, the nozzle, the injector, the target plate, and the exhaust duct.

The air source was a 100-psi gauge air reservoir maintained at constant pressure by a compressor. In order to minimize the moisture in the reservoir, the air supplied to the compressor was passed through a Kemp Oriad Adsorptive Dryer. MIL-STD-810F [7] indicates that the relative humidity of air used in the tests should be below 30%. The air from the reservoir was passed through a filter and a pressure regulator into a large plenum. Since the air velocity inside the plenum during the tests was negligible (less than one meter per second), the total pressure and temperature of the flow just upstream of the nozzle were measured using a static pressure tap and a thermocouple on the plenum.

The nozzle used was constructed of stainless steel with sharp-edges, a constant diameter, and an orifice length to diameter ratio of 3.43. A diagram of the nozzle is shown in Figure 7-10. Based on the work of Ward-Smith [21], the nozzle choked when the ratio of the exit pressure to the upstream pressure was 0.55 or less. Sand entered the nozzle through a $^1/_8$ inch ID stainless steel tube from the sand injector, which entered the side of the nozzle upstream of the orifice and then turned ninety degrees to align directly with the center of the orifice.

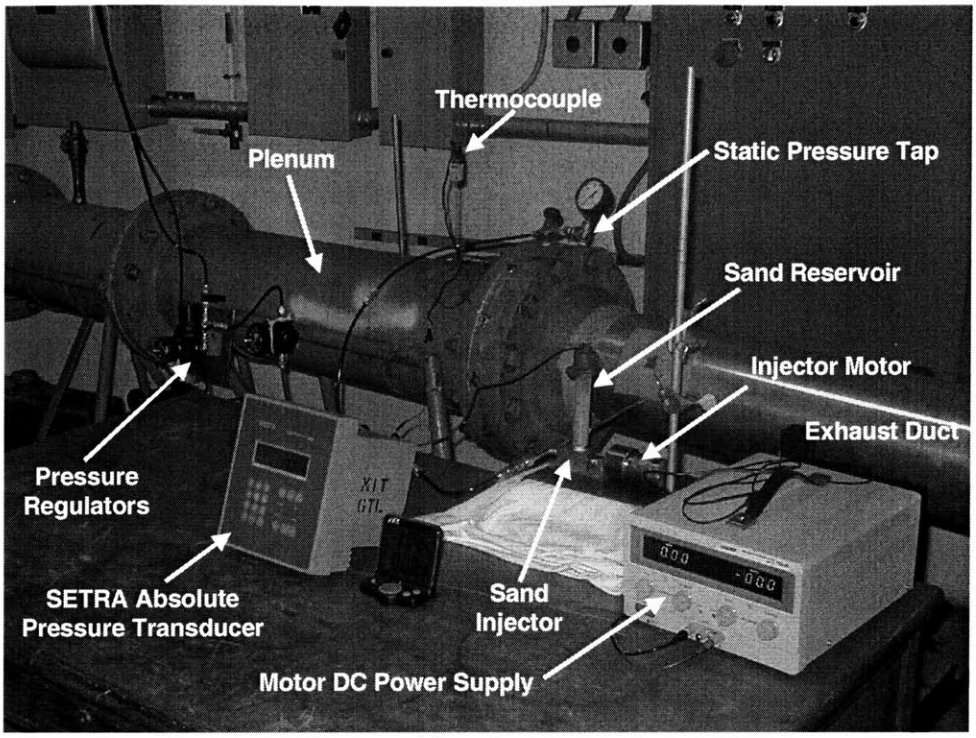


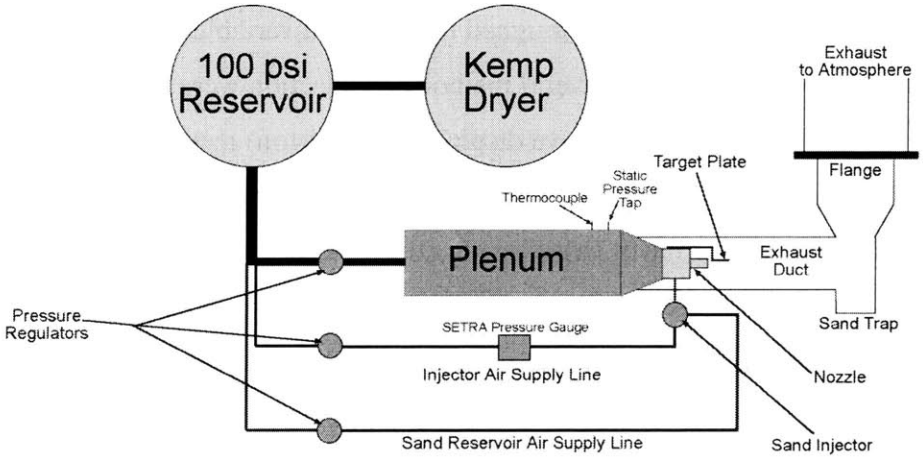


Figure 7-9. Sand Abrasion Experimental Rig Overview.

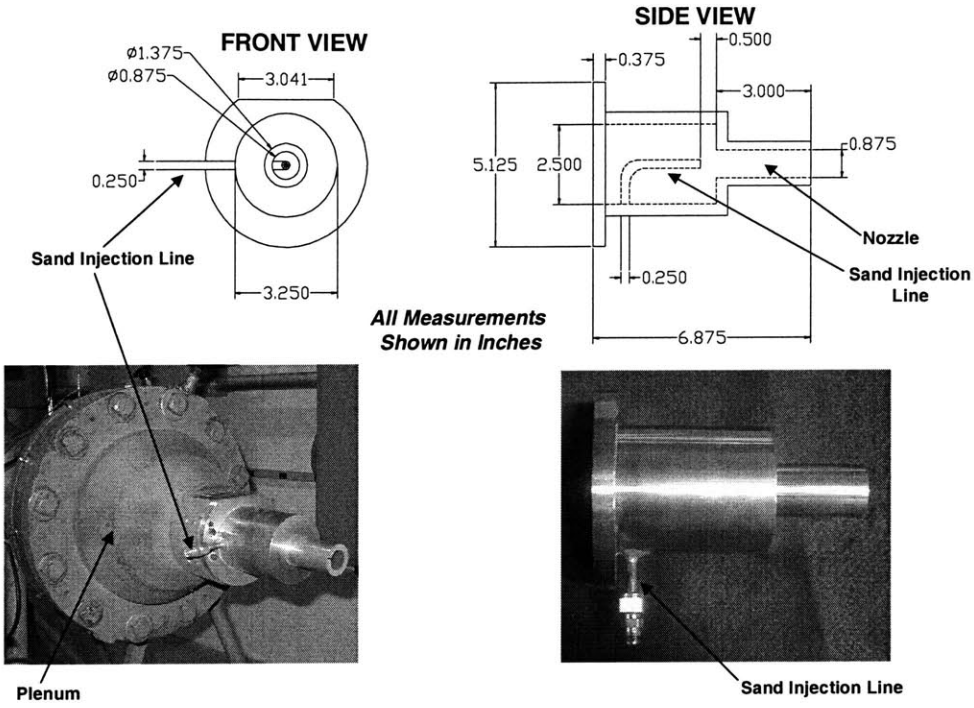


Figure 7-10. Nozzle Design.

The sand particle injector was designed to provide a variable and controlled rate of sand flow into the injector line. Several methods of injection were investigated to include gravity feed methods and positive displacement (piston) methods. However, due to the large grain sizes of the sand used, both gravity feed and positive displacement methods were useful only for much larger sand addition rates than desired since the particles tended to jam in small openings. In order to get sand to flow at the low rate desired, the injector design used a positive pressure difference across the injector to force the sand into the injection line with an agitator to prevent the sand from jamming.

The final injector design consisted of a pressurized particle reservoir positioned over a $^{5}/_{32}$ inch diameter, silicon carbide coated, double-fluted drill bit in a shaft connected to the high pressure sand injection line. The $^{5}/_{32}$ inch drill bit was used since it had flutes large enough to accommodate the largest of the sand particles. Figure 7-11 shows a diagram of the injector. The drill bit was spun by a DC motor at a constant speed, agitating the sand to ensure constant particle flow. As the drill bit turned, sand particles were forced to travel down the flutes of the bit and into the injection line by the pressure difference between the sand reservoir and the injection line. The reservoir pressure, and therefore the sand addition rate, was controlled using a pressure regulator

on the sand reservoir air supply line. In order to minimize sand particle interference with the movement of the drill bit, the clearance between the shaft and the injector walls was 0.002 inches, less than the diameter of the smallest sand grain used.

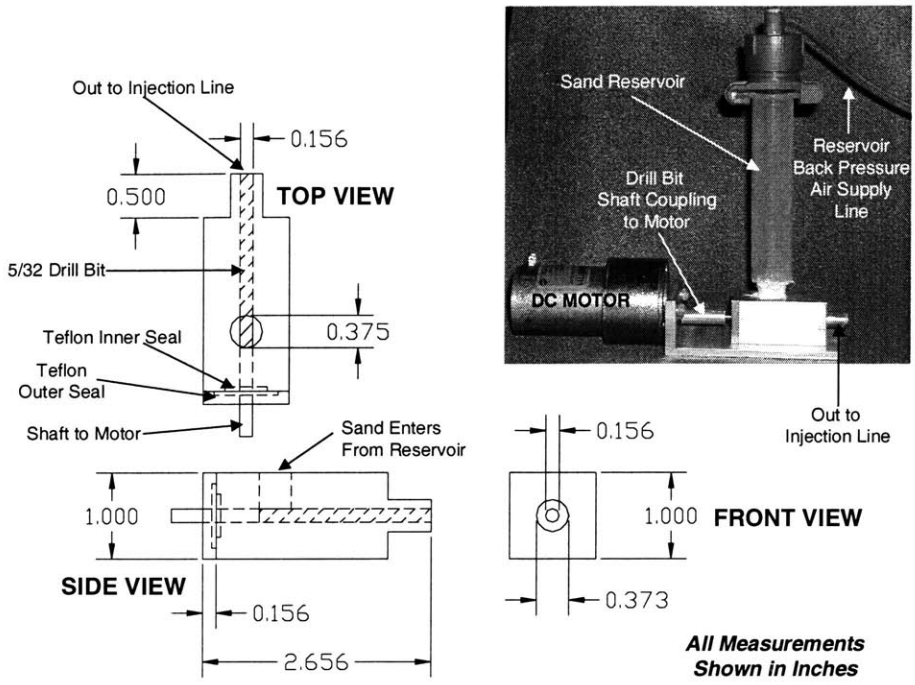


Figure 7-11. Sand Injector Design.

The abrasive element used for the sand abrasion tests was Type 4000 industrial grade quartz sand. Type 4000 sand closely matches the requirements established by MIL-HBK-310 [9] and MIL-STD-810F [7] which are listed in Section 4.2.3. The type of silica sand commonly used as a commercial sandblasting media could not be used due to the large particle sizes (up to 1000 micrometers in diameter) and the high hardness required (7 on the Moh's scale). The Type 4000 sand as used had a density of 1.57 g/cm$^3$ (1.61 g/cm$^3$ for the sand only – no air volume) with a Moh's hardness of 7. The sand grains had sharp angular edges, and in accordance with MIL-STD-810F were not reused since the force of the impacts during the tests blunts the sharp grain edges. Tables 7-2 and 7-3 below list the particle size breakdown and the typical component analysis for the sand (values provided by Browns Hill Sand & Glass Block).

| Type 4000 Sand Particle Sizes | | |
|---|---|---|
| Mesh Size | Avg Particle Size (μm) | % by Weight |
| 20 | 940 | 1 |
| 30 | 559 | 6 |
| 40 | 420 | 28 |
| 50 | 350 | 18 |
| 70 | 203 | 21 |
| 100 | 122 | 16 |
| 140 | 106 | 6 |
| 200 | 75 | 2 |

Table 7-2. Type 4000 Sand Particle Sizes.

| Type 4000 Sand Makeup | |
|---|---|
| Component | % by Weight |
| $SiO_2$ | 99+ |
| $NA_2O$ | 0.48 |
| $C_2O$ | 0.20 |
| $Fe_2O_3$ | 0.17 |
| Other | Less than 0.10 |

Table 7-3. Type 4000 Sand Composition.

The target plate was a $^1/_8$ inch thick Aluminum plate suspended in front of the nozzle as shown in Figure 7-12 in order to place the target sensor directly in line with the center of the nozzle orifice at a zero degree angle of incidence (parallel) to the air jet at a stream-wise distance of 3 inches. Figure 7-12 shows the layout of the target sensor on the target plate. In order to ensure that the only the surface of the target sensor was abraded by the sand, and not the exposed side facing the flow, a 0.025 inch thick Aluminum Oxide plate was placed in front of the target sensor. The Aluminum Oxide plate was polished to a 0.1 microinch finish and secured to the target plate with duct tape along the edges. To ensure that the surface of the target sensor was not shielded by the Aluminum Oxide plate, the target sensor was mounted to the target plate using MACtac® IF-2012 adhesive discussed previously in Section 2.2.2. The thickness of the adhesive ensured the target sensor would be raised above the Aluminum Oxide plate by less than 0.002 inches. The step between the Aluminum Oxide plate and the target sensor was filled in by epoxy to protect the exposed sensor edge and inspected under a microscope to ensure the epoxy did not rise above the level of the surface of the target sensor. Lead

wires (0.018 inch OD) were attached to the sensor leads and run to an RG-58A/U coaxial cable and then to a Fluke 8060 multimeter to measure the sensor electrical resistance. The leads of the sensors and the wires were then covered by duct tape in order to protect them from abrasion during the test runs.

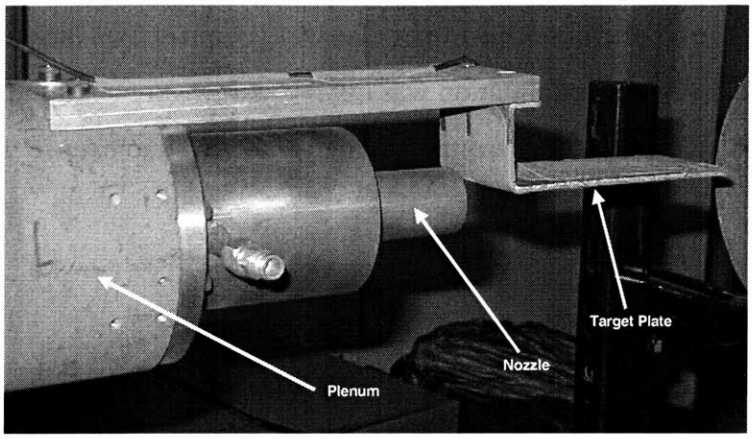


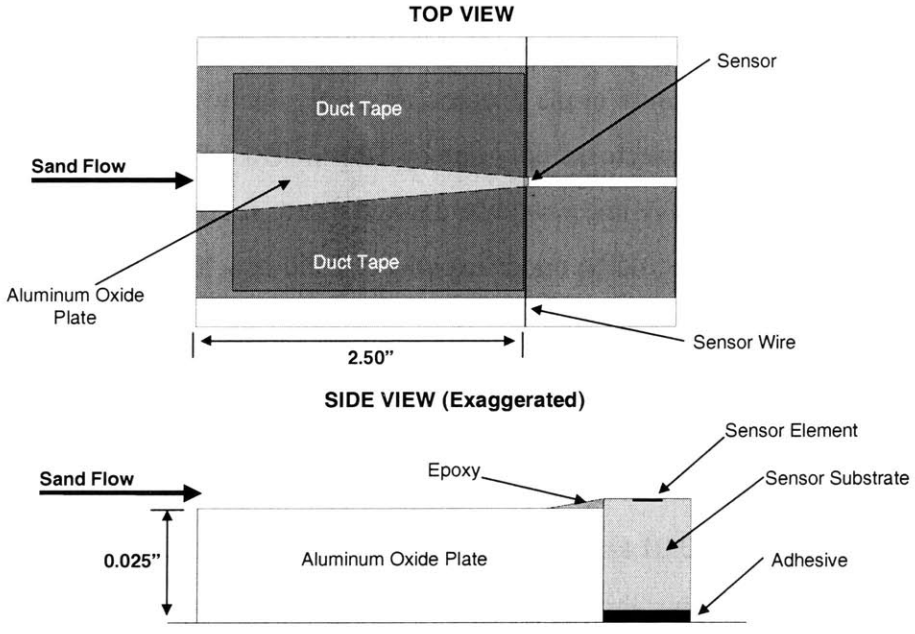


Figure 7-12. Target Plate Layout.

The exhaust ducting was made from 26 gauge galvanized steel typically used in HVAC applications. The duct was initially 8 inches in diameter and completely enclosed the nozzle as shown in Figure 7-9. The duct traveled horizontally and then made a ninety

degree turn to travel vertically while expanding to a 10 inch diameter. The duct then attached with a flange to a 12 inch diameter PVC pipe which vented to atmosphere outside the building. The increasing diameter of the pipe slowed the flow such that the velocities at the turn and at the flange were insufficient to support the sand particles against gravity. The majority of the sand particles were deposited in a removable sand trap at the bottom of the turn. Finer particles were deposited on the surface of the flange, but no significant sand accumulation was observed downstream of the flange. Note that the duct could be disconnected from the flange and moved to expose the nozzle and the target plate.

### *7.4.3 Methodology*

The first step in the conduct of the abrasion tests was to choke the nozzle by setting the pressure ratio (the ratio of the ambient pressure to the pressure in the plenum) to 0.55 or less using the pressure regulator between the air source and the plenum. Once the nozzle was choked, the SETRA absolute pressure gauge (100 psi range) was used to measure the pressure in the injector air supply line as shown in Figure 7-9 above. The regulator controlling the pressure in the injector air supply line was then adjusted to increase the pressure in the injector supply line by 10 psi. This increase in pressure ensured that the injector supply line would be choked due to friction and that the exit flow from the injector line would be under-expanded to aid in achieving a uniform particle distribution in the nozzle.

The sensor failure time ($t_f$) was defined as the sand exposure time required to produce a sudden increase in the sensor's electrical resistance by more than 0.05 Ω. It should be noted that the resistance of the sensor initially increased smoothly in increments on the order of 0.01 Ω at the beginning of each test as the flow temperature gradually increased and then stabilized. But, the sudden resistance changes due to particle impacts were easily discernable from the gradual initial increases due to the increasing flow temperature.

The maximum sand particle velocities at the target were estimated by assuming the particles to be individual quartz spheres. The flow velocity was determined at discrete points along the particle path and the resultant drag force and therefore the

acceleration on each particle at each point was determined using the known drag coefficient versus Reynolds number relationship for a sphere. To simplify the analysis, the average ambient and plenum temperature and pressure values for all of the tests were used along with the following assumptions:

1. The sand particles were brought to rest at the ninety degree turn in the sand injection line.
2. The flow in the sand injection line was adiabatic (valid for short ducts at high speed).
3. The sand injection line was choked due to friction (verified by calculation).
4. Flow from the plenum was isentropically accelerated to Mach 1 at the entrance of the nozzle orifice.
5. The flow maintained an average of Mach 1 through the choked nozzle orifice.
6. The velocity along the centerline of the nozzle exhaust remained constant from the nozzle exit to the target (a distance of 3.4 nozzle diameters). This is a reasonable rough approximation given the slightly under-expanded nature of the jet at the nozzle exit. For an incompressible axisymmetric jet, the centerline velocity remains constant for 7 nozzle diameters [25].
7. The particle paths were free of collisions with other particles or the nozzle sidewalls.

For the choked sand injection line, the flow Mach number was determined at each point by iterating the following equation from White [24]:

$$\frac{\bar{f}L'}{D} = \frac{1-M^2}{\gamma M^2} + \frac{\gamma+1}{2\gamma}\ln\left[\frac{(\gamma+1)M^2}{2+(\gamma-1)M^2}\right] \qquad \text{(Equation 7.6)}$$

where $\bar{f}$ is the tube friction factor, $L'$ is the distance to the exit of the tube (the sonic length), D is the tube diameter, $\gamma$ is the ratio of specific heats for air and M is the local Mach number.

Figure 7-13 below shows the estimated maximum particle velocities for the abrasion tests against the maximum particle velocities for the full-scale inlet developed in Section 4.2.3.

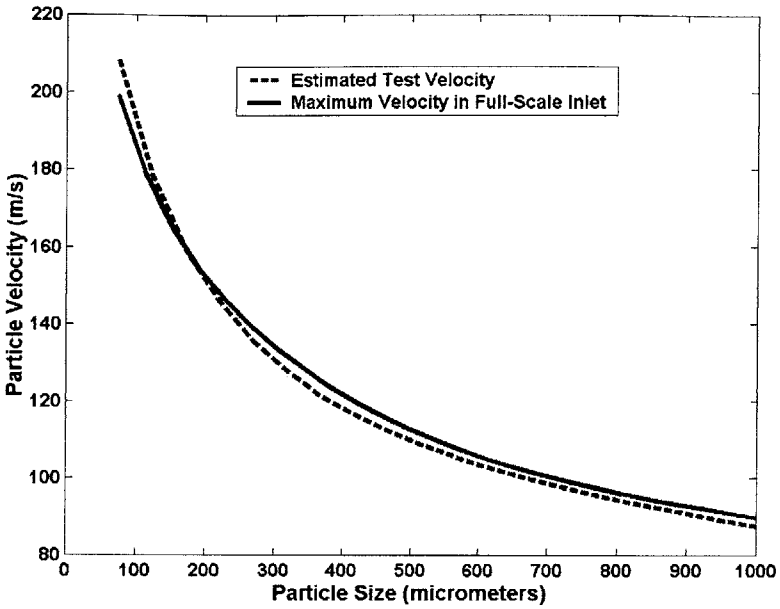


Figure 7-13. Sand Particle Velocity Comparison.

The maximum concentration of sand particles (expressed as the massflow of sand per unit area) near the separation point in the full-scale inlet under actual operating conditions was determined using Equation 7.7 below.

$$\dot{m}''_{s_{ref}} = \frac{\dot{m}_{a_{inlet}} \xi}{\rho_{a_{ref}} A_{inlet}} \qquad \text{(Equation 7.7)}$$

where $\dot{m}_{a_{inlet}}$ is the massflow of the full-scale inlet at cruise power (111.5 lb/s), $\xi$ is the maximum ambient concentration of sand in the air ($3.77 \times 10^{-4}$ kg sand per cubic meter of ambient air – see Section 4.2.3), $\rho_{a_{ref}}$ is the density of the ambient air for the full-scale inlet (1.225 kg/m$^3$), and $A_{inlet}$ is the cross-sectional area of the full-scale inlet at the separation point (0.2266 m$^2$) where the sensors would most likely be located. The actual average concentration of sand (massflow per unit area) achieved during each test was computed using the following relation:

$$\dot{m}''_{s_{test}} = \frac{V_s \rho_s \eta}{t_f A_s} \qquad \text{(Equation 7.8)}$$

where $V_s$ is the volume of sand injected during the test (m$^3$), $t_f$ is the sensor failure time (in seconds), $\rho_s$ is the density of the injected sand (1570 kg/m$^3$), $A_s$ is the cross-sectional

area of the core of the jet flow ($m^2$), and $\eta$ is the fraction of the total mass of the injected sand inside the core of the jet flow.

The values $A_s$ and $\eta$ were used to correct the sand concentration for the cross-sectional non-uniformity in the sand exiting the nozzle. The pattern of the sand exiting the nozzle was determined by placing a borosilicate glass plate perpendicular to the nozzle exhaust at the same stream-wise distance as the test sensor (3 inches). The impact of the sand impinging on the glass plate eroded the surface, and the pattern of erosion was used as an estimate of the cross-sectional distribution of the sand at the target point. Figure 7-14 below shows two cross-sections of the erosion pattern on the glass plate taken perpendicular to each other. The erosion pattern was measured using a depth indicator attached to a precision milling machine.

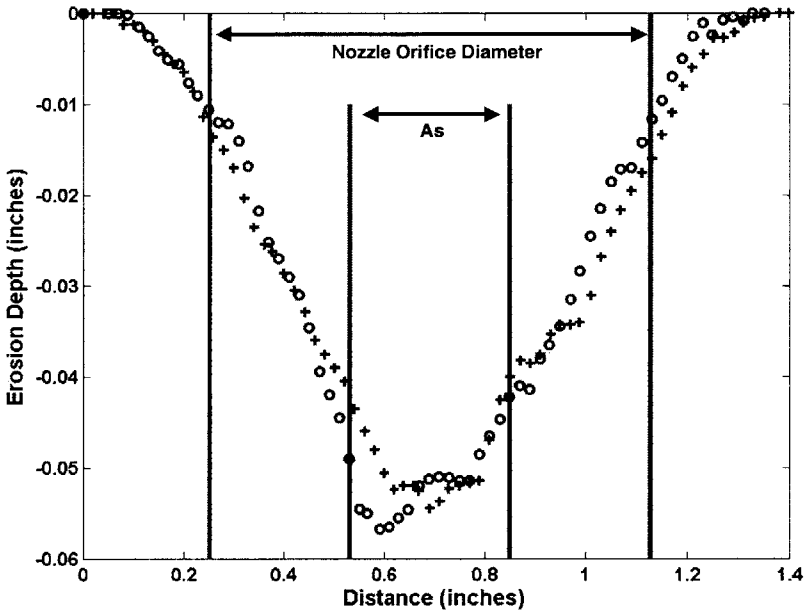


Figure 7-14. Sand Erosion Pattern.

From Figure 7-14 it is clear that the sand was not evenly distributed across the width of the nozzle. Since the target was placed in the approximate center of the erosion pattern, where the erosion damage was the most significant and therefore the concentration of sand was the highest, a calculation of the sand concentration using the entire width of the nozzle or the entire impact area would be an underestimate of the concentration seen by the target sensor. Thus, the area used ($A_s$) was the cross-sectional area of the center region, as indicated on Figure 7-14, where the sand distribution was approximately

uniform. The percentage of the total mass of sand inside the center region ($A_s$) was determined by assuming that it was approximately equal to the percentage of the total volume eroded inside the center region.

The sand concentrations during the tests where much larger than the reference concentration for actual operating conditions due to the difficulty of injecting sand at such low rates. Thus, the sensor failure times were corrected for the higher concentrations using the relation:

$$t_f' = t_f \left( \frac{\dot{m}''_{s_{test}}}{\dot{m}''_{s_{ref}}} \right) \qquad \text{(Equation 7.9)}$$

where $t_f'$ is the sensor failure time adjusted to the reference condition, $t_f$ is the sensor failure time during the test, and $\dot{m}''_{s_{test}}$ and $\dot{m}''_{s_{ref}}$ are the test and reference sand concentrations respectively.

### *7.4.4 Results and Discussion*

Five individual robust sensors were tested, with the test results shown below in Table 7-4. The uncertainty reflected in Table 7-4 was a result of the fact that the amount of sand injected could only be accurately measured to within ±0.5 milliliters. The mean failure time for the sensors tested was 21.7 minutes, corresponding to 574 flight hours using the assumptions from Section 4.2.3. The mean failure time met the requirement established in Section 4.2.3 of 19 minutes (500 flight hours). However, when examined individually, two of the five sensors failed this requirement.

| Sand Abrasion Results | | | | |
|---|---|---|---|---|
| Sensor Number | $\dot{m}''_{s_{test}}$ (kg/sm$^2$) | $t_f$ (s) | $t'_f$ (s) (± 73) | Equivalent Flight Hours (± 32) |
| 1 | 0.2151±0.0086 | 577 | 1734 | 765 |
| 2 | 0.1155±0.0096 | 516 | 867 | 382 |
| 3 | 0.2982±0.0129 | 383 | 1662 | 733 |
| 4 | 0.1490±0.0248 | 200 | 434 | 191 |
| 5 | 0.2278±0.0091 | 545 | 1807 | 797 |
| Parameters | | | | |
| $\dot{m}''_{s_{ref}}$ | 0.0687 kg/sm$^2$ | | | |
| $A_s$ | 5.189x10$^{-5}$ m$^2$ | | | |
| $\eta$ | 0.3282 | | | |

Table 7-4. Sand Abrasion Test Results.

But, although the robust sensors did not consistently meet the established abrasion resistance requirement, they did exhibit a significant improvement in abrasion resistance over unprotected sensors. The improvement in abrasion resistance was clear under microscopic inspection of protected and unprotected targets shown in Figure 7-15. The first image in Figure 7-15 is robust sensor number 3 after 25 milliliters of sand injection at ten times magnification. The second image is a quartz substrate with a 0.15 micrometer thick Nickel coating without a protective Aluminum Oxide layer after 25 milliliters of sand injection under the same conditions as sensor 3. Note that both photographs are shown to the same scale and that in both images, areas where the surface has been damaged appear darker than the surface.

It is important to note that these abrasion resistance tests were performed independent of the actual full-scale inlet geometry and the specific sensor locations. For an accurate indication of the actual failure time of the sensors as part of a full-scale inlet, the abrasion tests would need to be repeated with the sensors properly placed on the correct inlet geometry. Testing with the actual inlet geometry should significantly increase the useful life of the sensors since the separated flow region will be an area which diverges from the core flow through the inlet. Although some sand particles will be swept into the reverse flow of the separated region and abrade the sensors, those particles will be smaller and have less velocity than the particles used in the abrasion tests conducted here.

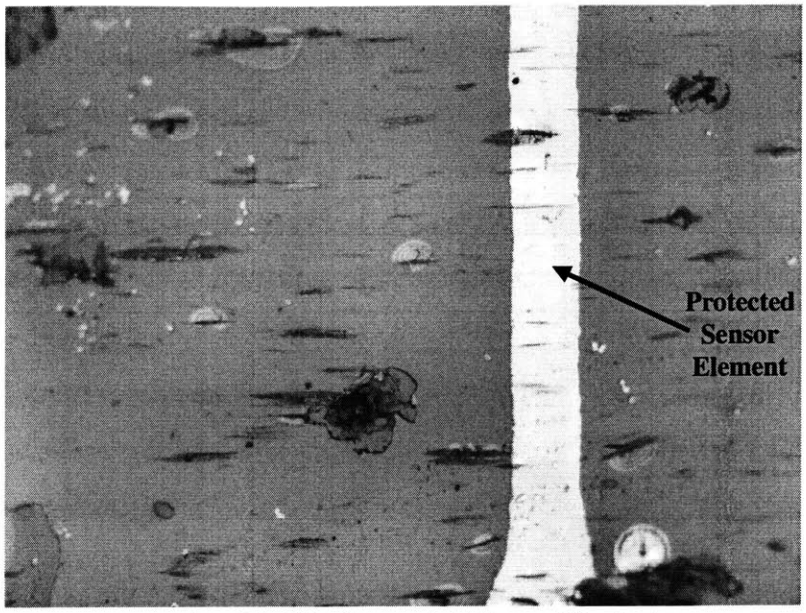


Robust Hot Film Sensor 3 (x10 magnification)

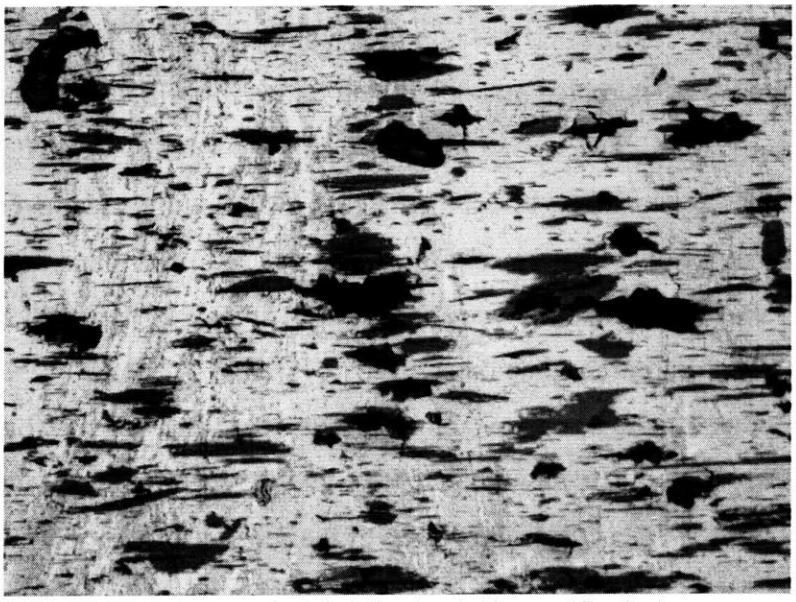

Unprotected Nickel Coating (x10 magnification)

Figure 7-15. Sand Abrasion Damage Comparison.

# 8 Conclusions & Recommendations

This research demonstrated the feasibility of using hot film sensors as inputs for active control systems in production aircraft seeking to reduce separation induced distortion at the compressor face. First, experiments conducted on a one-sixth scale model of a Northrup-Grumman UCAV inlet demonstrated that hot film sensors in the separated flow region were highly correlated to the unsteady regions of the AIP within a characteristic frequency band. Second, protected hot film sensors capable of withstanding the environmental hazards of the tactical flight environment without significant losses in performance were developed.

The small-scale UCAV inlet experiments demonstrated that the inlet exhibited a peak in unsteadiness near its scaled cruise massflow of 3.12 lb/s. This unsteadiness was accompanied by the presence of a characteristic frequency seen both in the separated flow region and at the AIP for massflows ranging from 2.9 lb/s to 3.4 lb/s, with the peak intensity at approximately 3.1 lb/s. Analysis of the time delay between the hot film sensors in the separated region and the total pressure sensors at the AIP indicated that the characteristic frequency was the result of a periodic convective disturbance traveling downstream from the hot film sensors to the AIP, such as vortex shedding from the separated flow region. Due to this disturbance, the hot film sensors, particularly those arrayed near the stagnation line at the leading edge of the separated region, were highly correlated (a maximum cross-correlation value of 0.68 with a maximum coherence value of 0.95) to the unsteady regions of the AIP within the characteristic frequency band. Because the correlations between the hot film sensors and the AIP were due to the presence of a periodic disturbance such as vortex shedding, further experiments on the full-scale next generation inlet for the UCAV must be conducted to determine if the unsteadiness observed in the small-scale inlet is unique to the small-scale inlet's particular geometry or if it is a generic characteristic of the family of short, separating inlets.

The hot film sensors also provided unambiguous information about the steady state strength of the separation at the AIP of the small-scale inlet. In the massflow range from 2.9 lb/s to 3.6 lb/s, the RMS of the AC coupled sensor output voltages for two sensors

located just behind and to either side of the center of the stagnation line at the leading edge of the separation decreased monotonically as the massflow increased.

For both steady and unsteady information about the conditions at the AIP, sensors located just behind the stagnation line along the leading edge of the separated region were the most highly correlated and the least subject to variation between experimental tests.

The robust hot film sensors developed and constructed were high aspect ratio (12.5-20), 0.2 micrometer thick, evaporated Nickel sensor elements on 635 micrometer thick quartz substrates protected by 2 micrometer thick sputtered Aluminum Oxide coatings with gold leads. The robust sensors were tested against environmental requirements for TCR time stability and sand abrasion resistance, and against performance requirements for steady-state sensitivity and dynamic response. The results of these tests showed that the robust sensors could withstand the environmental hazards of the tactical flight environment while meeting the performance requirements for use in an active control system with a sensor design life of 500 hours of operation. The sensors withstood the required temperature range of -77°C to 199°C and on average survived sand abrasion at the maximum particle velocities and sand concentration possible in an actual UCAV inlet for over 21 minutes (the equivalent of 574±73 flight hours) without a significant increase in resistance. The robust sensors demonstrated a stable performance over time, with a maximum TCR change of only 0.32% during thermal cycling at 200°C to simulate 500 hours of operation (compared to over 16% for the unprotected sensors used in the small-scale experiments). In terms of performance, the robust sensors demonstrated a steady-state laminar flow sensitivity of 82% of the unprotected sensors used in the small-scale experiments and a -3dB cutoff frequency for dynamic amplitude response of greater than 1 kHz. For dynamic phase response, the protective coating began to degrade the sensor response at 600 Hz.

Future work should include tests on the next generation full-scale UCAV inlet to verify the presence of the characteristic frequency and to determine its upper limit in order to establish more accurate sensor frequency response requirements. Additional sand abrasion tests that take into account the geometry of the inlet and the actual sensor locations should also be conducted. Because the sensors will most likely be placed in the separated flow region where the inlet walls diverge from the core flow, sand abrasion

tests incorporating the inlet geometry should result in much longer sensor life spans since the particles caught in the reverse flow of the separation will have a lower velocity and will be predominantly smaller than those used in the sand abrasion tests conducted as part of this research.

Further improvements to the robust hot film sensor design should include increasing the sensor aspect ratio, reducing the thermal conductivity of the probe holder, and protecting the sensor leads from abrasion. Increasing the sensor aspect ratio will help to offset the effective reduction in aspect ratio and steady-state sensitivity due to the diffusion of heat through the protective coating. Reducing the thermal conductivity of the probe holder to a value of the same order or less than that of the sensor substrate, either by isolating the sensor substrate from the probe holder with a layer of insulation or by simply making the probe holder itself out of a material with a lower thermal conductivity, will improve both the steady-state sensitivity of the sensor and also the phase response of the sensor below 600 Hz. Protecting the sensor leads from abrasion can be done using numerous methods which already exist in the commercial sensor industry.

To summarize, robust hot film sensors capable of withstanding the environmental hazards common to tactical aircraft while meeting the performance requirements for use in an active control system were developed and characterized. The usefulness of these sensors was demonstrated by employing hot film sensors in the separated flow region of a small-scale Northrup-Grumman UCAV inlet to show that they can provide real time information about the steady and unsteady separation induced distortion at the AIP.

# References


1. J.D. Anderson. Modern Compressible Flow. McGraw-Hill Publishing Company, second edition, 1990.

2. D.R. Askeland. The Science and Engineering of Materials. PWS-Kent Publishing Company, second edition, 1989.

3. J.V. Beck and K.D. Cole. *Conjugated Heat Transfer From a Hot-Film Probe for Transient Air Flow.* Transactions of the ASME, Volume 110, 290-296, 1988.

4. M. Brear. *A Summary of the Computed Flow Structure Within the UCAV Engine Inlet.* MIT Micro-Adaptive Flow Control Project internal memorandum, 2000.

5. S.A. Campbell. The Science and Engineering of Microelectronic Fabrication. Oxford University Press, 1996.

6. W.J. Cook, T.A. Giddings, and J.D. Murphy. *Response of Hot Element Wall Shear Stress Gages in Laminar Oscillating Flows.* AIAA Journal, Volume 26, 706-713, 1988.

7. Department of Defense Test Method Standard for Environmental Engineering Considerations and Laboratory Tests. MIL-STD-810F, 2000.

8. M. Drela. Lectures, Course 16.13, *Aerodynamics of Viscous Fluids.* Department of Aeronautics and Astronautics, Massachusetts Institute of Technology, Fall 2001.

9. Global Climatic Data for Developing Military Products. Department of Defense Handbook 310, 35-6, 1997.

10. G.R. Guenette. *A Fully Scaled Short Duration Turbine Experiment.* Ph.D. Thesis, Massachusetts Institute of Technology, 1985.

11. F.P. Incropera and D.P. DeWitt. Introduction to Heat Transfer. John Wiley and Sons, second edition, 1990.

12. K.M. Kalumuck. *A Theory for the Performance of Hot-Film Shear Stress Probes.* Ph.D. Thesis, Department of Mechanical Engineering, Massachusetts Institute of Technology, 1983.

13. S. Kuppa and S.M. Mangalam. *In Flight Detection of Flow Separation, Stagnation and Transition.* ICAS-92-3.7.2.

14. S.M Mangalam, T.M. Moes and G.R. Sarma. *Flight Demonstration of a Shock Location Sensor Using Constant Voltage Hot-Film Anemometry.* NASA Technical Memorandum 4806, 1997.

15. *Measurement Uncertainty*. ANSI/ASME PTC 19.1-1985.

16. A.N. Menendez and B.R. Ramaprian. *The Use of Flush-Mounted Hot-Film Gauges to Measure Skin Friction in Unsteady Boundary Layers*. Journal of Fluid Mechanics, Volume 161, 139-159, 1985.

17. A.F. Mills. Heat and Mass Transfer. Irwin, 1995.

18. C.I. Popescu and M. Popescu. *Thermo-Resistive Sensors*. Thin Film Resistive Sensors, Ed. P. Ciureanu, 215-252, Institute of Physics Publishing, 1992.

19. R.L. Simpson. *Turbulent Boundary-Layer Separation*. Annual Review of Fluid Mechanics, Volume 21, 222, 1989.

20. S.D. Stearns. Digital Signal Analysis. Prentice-Hall, Inc., 1990.

21. A.J. Ward-Smith. *Critical Flowmetering: The Characteristics of Cylindrical Nozzles with Sharp Upstream Edges*. Int. Journal of Heat and Fluid Flow, Volume 1, No. 3, 123-132, 1979.

22. Z. Warfield. *Active Control of Separation Induced Distortion in a Scaled Tactical Aircraft Inlet*. S.M. Thesis, Department of Aeronautics and Astronautics, Massachusetts Institute of Technology, 2001.

23. Wear Resistant Surfaces in Engineering. Department of Trade and Industry, Her Majesty's Stationary Office, 1986.

24. F.M. White. Fluid Mechanics. McGraw-Hill Publishing Company, second edition, 1986.

25. F.M. White. Viscous Fluid Flow. McGraw-Hill Publishing Company, second edition, 1991.

# Appendix A – Hot Film Sensor Array Wiring Scheme

The wires from the hot film sensor leads were connected to the pins of "D" connectors mounted to brackets on either side of the inlet piece. The numbering scheme for these "D" connectors is shown below in Figure A-1. Table A-1 lists the "D" connector and the specific pins to which each sensor is attached. Table A-2 details how each CTA is connected to the data acquisition system (DAQ).

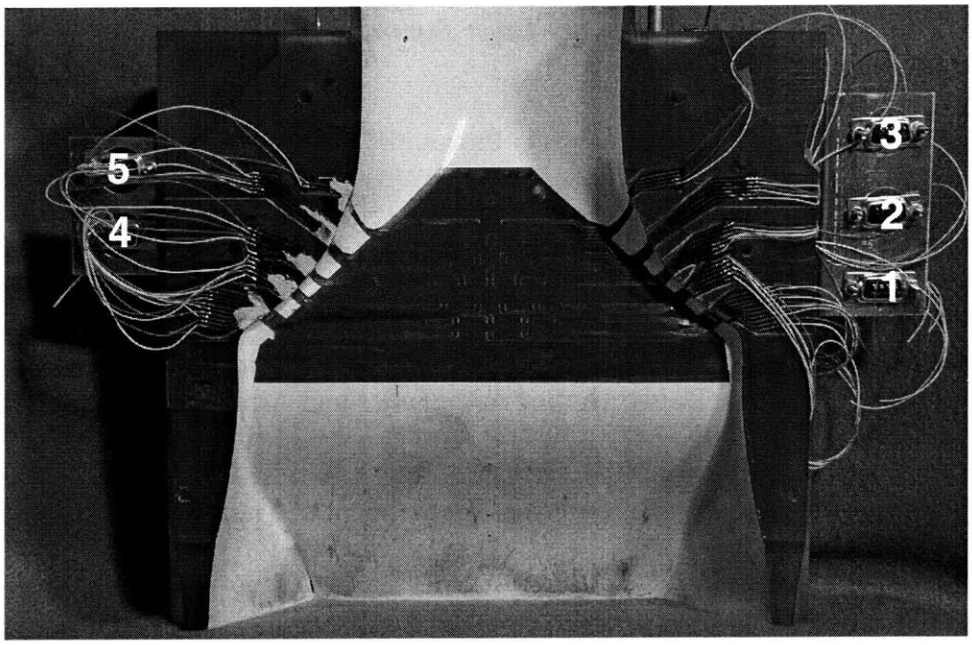


Figure A-1. D Connector Numbering.

| Sensor Number | "D" Connector | Pins |
|---|---|---|
| 1 | 5 | 5,10 |
| 2 | 3 | 11,12 |
| 3 | 5 | 13,14 |
| 4 | 3 | 8,9 |
| 5 | 3 | 6,7 |
| 6 | 5 | 8,9 |
| 7 | 5 | 11,12 |
| 8 | 3 | 3,4 |
| 9 | 3 | 1,2 |
| 10 | 5 | 3,4 |
| 11 | 5 | 6,7 |
| 12 | 2 | 5,10 |
| 13 | 2 | 13,14 |
| 14 | 2 | 11,12 |
| 15 | 5 | 1,2 |
| 16 | 4 | 5,10 |
| 17 | 4 | 13,14 |
| 18 | 2 | 3,4 |
| 19 | 2 | 6,7 |
| 20 | 2 | 8,9 |
| 21 | 4 | 6,7 |
| 22 | 4 | 8,9 |
| 23 | 4 | 11,12 |
| 24 | 2 | 1,2 |
| 25 | 1 | 7,8 |
| 26 | 4 | 3,4 |
| 27 | 4 | 1,2 |
| 28 | 1 | 1,2 |
| 29 | 1 | 3,4 |
| 30 | 1 | 5,6 |

Table A-1. Hot Film Sensor to D Connector Wiring Scheme.

| DANTEC 56C17 CTA | Signal Conditioner | Output Wire (to DAQ) | DAQ Board | DAQ Channel |
|---|---|---|---|---|
| 1 | DANTEC 56N20 | 17 | 1 | 1 |
| 2 | Model 2300 | 31 | 1 | 2 |
| 3 | Model 2300 | 32 | 1 | 3 |
| 4 | Model 2300 | 1 | 1 | 4 |
| 5 | Model 2300 | 2 | 1 | 5 |
| 6 | Model 2300 | 3 | 1 | 6 |
| 7 | Model 2300 | 4 | 1 | 7 |
| 8 | Model 2300 | 5 | 1 | 8 |
| 9 | Model 2300 | 6 | 2 | 1 |
| 10 | Model 2300 | 7 | 2 | 2 |
| 11 | DANTEC 56N20 | 8 | 2 | 3 |
| 12 | DANTEC 56N20 | 9 | 2 | 4 |
| 13 | DANTEC 56N20 | 23 | 2 | 5 |
| 14 | DANTEC 56N20 | 24 | 2 | 6 |
| 15 | DANTEC 56N20 | 25 | 2 | 7 |
| 16 | DANTEC 56N20 | 27 | 2 | 8 |
| 17 | DANTEC 56N20 | 29 | 3 | 1 |
| 18 | DANTEC 56N20 | 30 | 3 | 2 |

Table A-2. CTA to DAQ Wiring Scheme

# Appendix B – Small-Scale Inlet Test Matrix

Table B-1 below is the test matrix for all of the experimental runs performed on the small-scale inlet with the hot film sensor array and shows which sensor was connected to each CTA for each test as well as the sensor lead and cable resistance ($R_l$) and the sensor overheat resistance ($R_h$). The path from each CTA to the DAQ is detailed in Table A-2. Table B-2 shows the detailed test information for the AIP total pressure sensors.

| CTA | Test 1 | | | Test 2 | | | Test 3 | | |
|---|---|---|---|---|---|---|---|---|---|
| | Sensor | $R_l$ | $R_h$ | Sensor | $R_l$ | $R_h$ | Sensor | $R_l$ | $R_h$ |
| 1 | 20 | 0.85 | 12.40 | 30 | 1.12 | 12.52 | 26 | 1.32 | 12.42 |
| 2 | 19 | 1.27 | 12.22 | 29 | 1.46 | 12.26 | 29 | 1.46 | 12.26 |
| 3 | 28 | 1.03 | 11.98 | 28 | 1.52 | 12.32 | 17 | 1.15 | 11.95 |
| 4 | 17 | 1.38 | 12.18 | 24 | 1.41 | 12.51 | 24 | 1.41 | 12.51 |
| 5 | 14 | 1.84 | 13.69 | 23 | 1.27 | 12.07 | 23 | 1.27 | 12.07 |
| 6 | 13 | 0.94 | 11.74 | 22 | 1.32 | 12.12 | 22 | 1.32 | 12.12 |
| 7 | 12 | 1.19 | 11.84 | 21 | 1.20 | 12.90 | 21 | 1.20 | 12.90 |
| 8 | 11 | 1.28 | 12.08 | 20 | 1.15 | 12.70 | 20 | 1.15 | 12.70 |
| 9 | 10 | 1.10 | 12.20 | 19 | 1.17 | 12.12 | 11 | 0.97 | 11.77 |
| 10 | 9 | 1.07 | 11.92 | 18 | 1.31 | 12.26 | 18 | 1.31 | 12.26 |
| 11 | 8 | 0.84 | 11.64 | 25 | 1.45 | 13.00 | 10 | 0.64 | 11.74 |
| 12 | 7 | 0.90 | 11.70 | 13 | 0.60 | 11.40 | 7 | 0.76 | 11.56 |
| 13 | 6 | 0.85 | 11.70 | 27 | 1.43 | 12.23 | 27 | 1.43 | 12.23 |
| 14 | 5 | 1.33 | 12.58 | 9 | 0.87 | 11.82 | 6 | 0.77 | 11.72 |
| 15 | 4 | 0.51 | 11.36 | 8 | 0.67 | 11.47 | 3 | 0.72 | 11.67 |
| 16 | 3 | 0.95 | 11.80 | 5 | 1.06 | 12.31 | 1 | 0.75 | 11.40 |
| 17 | 2 | 0.91 | 11.71 | 4 | 0.53 | 11.48 | 4 | 0.53 | 11.48 |
| 18 | 1 | 1.00 | 11.65 | 2 | 0.84 | 11.64 | 2 | 0.84 | 11.64 |

Table B-1. Hot Film Array Test Matrix.

| Model 2300 Amplifier | Total Pressure Sensor | Test 1 | Test 2 | Test 3 | Output Wire | DAQ Board | DAQ Channel |
|---|---|---|---|---|---|---|---|
| | | Location (*Fig 2-6*) | | | | | |
| 1 | 1 | 37 | 37 | 37 | 10 | 3 | 3 |
| 2 | 2 | midpt 37-2 | midpt 37-1 | 1 | 11 | 3 | 4 |
| 3 | 3 | 2 | 1 | 7 | 12 | 3 | 5 |

Table B-2. AIP Total Pressure Sensor Test Matrix.